UNIVERSITÁ DI PISA
DOTTORATO DI RICERCA IN INGEGNERIA DELL'INFORMAZIONE

A NOVEL METHODOLOGY FOR LITHIUM-ION BATTERY SYSTEM DESIGN IN MEDIUM AND HIGH POWER APPLICATIONS

DOCTORAL THESIS

Author
Roberto Di Rienzo

Tutor
Prof. Roberto Saletti

Reviewers
Prof. Alessandro De Gloria
Prof. Henk Jan Bergveld

The Coordinator of the PhD Program
Prof. Marco Luise

Pisa, 11 2017

XXX

Summary

LITHIUM-ION batteries are unquestionably the best choice to power small devices, such as smartphones, tablets, and laptops. In the last years, they have been introduced into many other market sectors, ranging from high-power applications, such as electric vehicles, renewable energies, and uninterruptible power supplies, to medium-power applications. The latter include small electric vehicles and tools for gardening, housework, building, and cleaning the streets. The vast spreading of this technology is due to its superiority, compared to all the other rechargeable battery technologies, in terms of energy and power density, long cycle and calendar life, lower self-discharge, and fast charging rate. These aspects introduce some unequivocal performance advantages in the target application, but at the same time the higher cost of the technology slows down its adoption. Moreover, the lithium-ion battery must be equipped with a Battery Management System (BMS), an electronic board that controls the battery behavior to maintain the battery cells in their safety operation area (SOA) with respect to voltage, temperature and current. In fact, these lithium-ion cells can suffer from accelerated aging or even irreversible damages if they work outside the SOA. The BMS cost increases the already high cost of the battery, making its cost issue more critical.

To solve this problem, some innovative design methodologies are presented in the thesis to develop smart battery systems, which allow a reduction of the battery cost and enable a clear performance breakthrough in some specific applications. For example, in the field of electric traction, there are a lot of applications that are characterized by some work phases interspersed with rest times, such as the public transportation and the handling of materials in the warehouses. This characteristic can be combined with the lithium-ion fast charging rate to reduce the needed battery size, and therefore its cost. In fact, the application rest times can be used to recharge the battery of the energy used in the work phases, with a fast charge policy. Obviously, the application of a fast charge policy requires a greater initial investment to buy a most powerful charger but its cost can be divided among many vehicles. To analyze this approach, we have designed and realized a lithium-ion battery to power an electric minibus for the public transportation. It was originally equipped with a $72\,\mathrm{V}$ lead acid battery

that was degraded making the minibus unusable. This problem is very common, in fact in the last years many electric vehicles have been sold with a lead acid battery to reduce their initial cost. Unfortunately, the lead acid technology presents a reduced lifetime, and nowadays there are many unused electric vehicles in the world because their battery is degraded. For this reason, the developed battery has been based on a $12\,\mathrm{V}$ standard module, compatible with the classic lead acid battery, which can be used in these situations to replace the old batteries. In this way, the module cost can be reduced thanks to the increasing of its production volume, making the module attractive for these and other applications. The developed minibus has demonstrated that a battery of only $240\,\mathrm{A\,h}$ can guarantee a continuous work to the minibus if it is recharged for one minute each ran kilometer and the maximum distance between two fully recharges is less than about $40\,\mathrm{km}$. These values are very promising, because they are compatible with the real use of the minibus and the small size battery presents a very attractive cost.

The modular approach can also introduce many advantages in other applications, such as tools for gardening, housework, and building. In these fields, many applications require the same battery voltage, so the manufacturer develops the battery that can power a family of tools. The number of the family tools is limited by their different requirements in term of power and especially of energy to guarantee a good run-time. In fact, the battery size needed to obtain a good run-time of the most powerful application would be unsaleable with the least powerful ones. The modular approach can solve the problem. In the presented work, we have developed a standard battery that can be parallel-connected to increase its capacity, and therefore the availability of the battery system. The battery parallelization must be controlled to avoid unsafe situations due to the high current that could flow from one battery into the other ones if its voltage is higher than the other. This problem can be easily solved connecting the batteries in parallel with the diodes which stop this current. However, this solution is not adoptable in this system because it dissipates a lot of energy. The diodes can be replaced with the power switches to reduce the dissipated power. This solution increases the complexity of the system, because it must control the switches with a smart algorithm to avoid the unsafe situation. For this reason, the developed standard battery has been provided with a power switch, which is used by the internal BMS to protect the cells and can be closed by the application control unit to parallel-connect the batteries.

To find the best parallelization algorithm, a dedicated simulation platform has been developed. It emulates the behavior of two standard batteries, on which a power profile of a lawnmower can be applied to evaluate the algorithm performances in a realistic condition. In particular, the parallelization, in addition to the increase of the available energy, reduces the battery current and consequently the cell temperature. The reduction of these stresses increases the lifetime of the battery as widely demonstrated in literature. The presented concepts have been tested developing a dual battery gardening system, which is composed of a smart lawnmower and an innovative charger that implements the Internet of Thing (IoT) paradigm. The lawnmower has been provided with a custom main unit, based on a microcontroller, in which the parallelization algorithm is executed. The main unit embeds also a bluetooth module to implement the IoT paradigm and with which the user can monitor the state of the system and configure the behavior of the motor controlled by the main unit as well. The IoT concept has been

also introduced into the developed charger, which is equipped with a Wi-Fi module. Therefore, it can collect the battery data and send them to a company cloud. This is an interesting opportunity for both the manufacturer and the user, because the first one can process the data of all his sold systems and extract some valuable market indications. At the same time, the manufacturer can process some advanced information items for the user which allow them to optimize the use of their system. With respect to this, the charger can apply a custom current profile to the battery to increase the informative contents of the data uploaded on the cloud. The charger can concurrently manage all the system batteries to always maintain them in a SOA and ready to be used. This feature is fundamental in a multi-batteries system because it helps the user to manage all their batteries in an effective way.

Sommario

Le batterie agli ioni di litio sono probabilmente la scelta migliore per l'alimentazione di piccoli dispositivi, come per esempio smartphone, tablet e laptop. Negli scorsi anni, tale tecnologia è stata introdotta in tantissimi altri settori del mercato che vanno dalle applicazioni di alta potenza, come per esempio veicoli elettrici, sistemi di accumulo per siti di produzione di energie rinnovabili e sistemi per il backup energetico (UPS), ad applicazioni di media potenza. In questo ultimo campo, sono molteplici i dispositivi che sono stati dotati di batteria agli ioni di litio e sul mercato è facile trovare elettroutensili per il giardinaggio, l'edilizia, i lavori domestici e per la pulizia.

La larga diffusione delle batterie al litio è data dalla loro superiorità rispetto alle altre tecnologie di batterie ricaricabili grazie a un'elevata densità di potenza ed energia, maggior numero di cicli di ricarica, minor auto-scarica e la possibilità di essere ricaricate con alte potenze, riducendo i tempi di ricarica. Questi aspetti introducono notevoli vantaggi nelle applicazioni in cui sono usate, ma allo stesso tempo, l'alto costo della tecnologia ne rallenta la diffusione.

Le batterie agli ioni di litio devono poi essere dotate di un sistema elettronico di controllo, chiamato solitamente Battery Management System (BMS), che gestisce la batteria e la mantiene nella zona sicura di funzionamento (Safety Operation Area, SOA). Infatti, le batterie al litio lavorando fuori da tale zona in cui sono fissati limiti di tensione, corrente e temperatura, possono presentare un invecchiamento accelerato, in particolari casi danni permanenti che ne inficiano l'uso, e addirittura essere non sicure. Il BMS, ovviamente, aumenta il costo già alto di questa tecnologia, rendendo spesso il costo la metrica più importante nella progettazione delle batterie. Per favorire la diffusione di questa promettente tecnologia tenendo conto delle problematiche evidenziate, nel percorso di dottorato sono state sviluppate una serie di metodologie, descritte nel dettaglio nella presente tesi, da applicare in fase di progettazione.

Per esempio, nel campo dei veicoli a trazione elettrica ci sono molteplici applicazioni le cui caratteristiche si sposano bene con la tecnologia agli ioni di litio, come il trasporto pubblico o la movimentazione di materiali nei magazzini. Infatti, esse sono caratterizzate da cicli operativi interallacciati da momenti di pausa, nei quali si può

sfruttare la possibilità offerta da tale tecnologia di essere ricaricata con elevate potenze (fast charge) per recuperare parte o tutta l'energia utilizzata nei cicli operativi precedenti. Tale approccio consente di ridurre l'energia che deve essere immagazzinata nella batteria per garantire una buona autonomia, e quindi ne riduce il costo, l'ingombro e il peso con notevoli benefici per l'applicazione. Ovviamente, l'applicazione di profili di ricarica rapida richiede un incremento del costo dell'infrastruttura che però può essere ammortizzato su un gran numero di veicoli. Nel lavoro di dottorato si è potuto validare tale concetto all'interno di un progetto in collaborazione con ENEA, nel quale è stata progettata e realizzata una batteria agli ioni di litio per un minibus elettrico adibito al trasporto pubblico secondo profili d'uso compatibili con l'approccio fast charge. Il minibus in esame era originariamente equipaggiato con una pesante batteria al piombo acido da $72\,\mathrm{V}$ e $585\,\mathrm{A\,h}$, ormai degradata e con autonomia insufficiente al ciclo operativo giornaliero del minibus. Il risultato della sperimentazione ha dimostrato che con una batteria di soli $240\,\mathrm{A\,h}$ il minibus presenta un'operatività teoricamente infinita purché sia ricaricato per 1 minuto ogni kilometro percorso e vengano percorsi al massimo $40\,\mathrm{km}$ tra una ricarica completa e la successiva.

La batteria è stata progettata seguendo un approccio modulare, dove il modulo base ha una tensione di $12\,\mathrm{V}$ ed è compatibile con le classiche battere al piombo acido. In questo modo esso può essere utilizzato per il ricondizionamento di veicoli preesistenti con un mercato notevolmente più ampio e di conseguenza con un maggiore volume di produzione, il che porta a una riduzione dei costi.

L'approccio modulare può introdurre notevoli vantaggi anche in altre applicazioni, come per esempio elettroutensili per il giardinaggio o l'edilizia. In questi ambiti i produttori tendono a progettare utensili con la stessa tensione operativa in modo da renderli compatibili con un unico tipo di batteria che può alimentare l'intera famiglia di prodotti. Le limitazioni di tale approccio sono date dell'impossibilità di soddisfate il fabbisogno energetico di tutte le applicazioni con una batteria di taglia unica, in quanto, la batteria progettata per soddisfare l'utensile più energivoro risulta poco proponibile in termini di peso, volume e costo con le applicazioni che richiedono basse energie. Per tale motivo molti produttori propongono diverse taglie di batterie compatibili meccanicamente ed elettricamente, ma con diverse capacità, rinunciando parzialmente ai vantaggi di un modulo standard. Per risolvere questa contraddizione, in questa tesi è stata presentata una batteria standard che può soddisfare i requisiti di numerose applicazioni grazie alla possibilità di essere connessa in parallelo ad altre simili.

La connessione di batterie in parallelo richiede particolari accorgimenti hardware/-software per evitare condizioni potenzialmente distruttive per l'applicazione o per le batterie. Infatti, se due batterie simili con una notevole differenza di tensione, dovuta al diverso stato di carica, vengono connesse in parallelo, si ha una notevole corrente di circolazione, limitata solo dalle bassissime resistenze serie delle batterie, che scorre dalla batteria più carica all'altra, per bilanciare il sistema. L'uso di dispositivi passivi quali i diodi per risolvere tale problema comporta un'inaccettabile perdita di efficienza.

La soluzione proposta utilizza degli interruttori a stato solido al posto dei diodi, gestiti con algoritmi "smart" che prevengono condizioni poco sicure per il sistema. Di conseguenza, la batteria standard è dotata di un interruttore di potenza utilizzato dal BMS interno per garantire la sua sicurezza, ma che può essere attivato tramite comando esterno. Tale interruttore viene controllato dall'apposito algoritmo di parallelizzazione

eseguito dall'unita di calcolo dell'utensile che utilizza le batterie. Per trovare il miglior algoritmo di parallelizzazione è stata realizzata una piattaforma simulativa che ha consentito di sviluppare, analizzare e confrontare diversi algoritmi in totale sicurezza, ma nelle condizioni più vicine possibili a quelle reali. Da tale studio è stato individuato il miglior algoritmo che massimizza il tempo in cui le batterie sono parallelizzate, portando a una riduzione della corrente media erogata dalle singole batterie. Tale aspetto incrementa l'energia estraibile dal sistema batteria a parità delle condizioni di partenza e riduce la temperatura di lavoro delle stesse. Quest'ultimo effetto, insieme alla riduzione degli stress di corrente, porta a un incremento della vita utile delle batterie, come ampiamente documentato in letteratura.

Per verificare tali concetti è stato sviluppato un dimostratore a doppia batteria che è composto da un rasaerba e un charger innovativi, che implementano anche il paradigma IoT (Internet of Thing). Il rasaerba è provvisto di un'unita di controllo custom basata su un microcontrollore il quale esegue l'algoritmo di parallelizzazione, controlla il motore e gestisce la comunicazione tramite un modulo Bluetooth. La possibilità di una comunicazione permette all'utente di monitorare il sistema e configurarlo, adattandolo alla particolare situazione nella quale esso verrà utilizzato. Il concetto di IoT viene anche sfruttato sul charger, il quale è dotato di un modulo Wi-Fi, che può connettersi a un cloud aziendale per caricare le informazioni dalle batterie e ricevere configurazioni o aggiornamenti di sistema. Tale possibilità è utile al produttore, il quale, se autorizzato, può utilizzare questi dati per analisi di mercato, e anche per l'utente che può ricevere dal produttore analisi avanzate sul sistema e avvisi in caso di uso impropri o semplicemente consigli su come poter ottimizzare il sistema in funzione del suo utilizzo.

List of publications

International Conferences/Workshops with Peer Review

1. Baronti, F., Di Rienzo, R., Papazafiropulos, N., Roncella, R., Saletti, R. (2014,December). Investigation of series-parallel connections of multi-module batteries for electrified vehicles *International Electric Vehicle Conference (IEVC)*. (pp. 660-666). IEEE.

2. Baronti, F., Di Rienzo, R., Moras, R., Roncella, R., Saletti, R., Pede, G., Vellucci, F. (2015,July). Implementation of the fast charging concept for electric local public transport: the case-study of a minibus. *13th International Conference on Industrial Informatics (INDIN)*. (pp.1284-1289). IEEE.

3. Morello, R., Zamboni, W., Baronti, F., Di Rienzo, R., Roncella, R., Spagnuolo, G., Saletti, R. (2015,November). Comparison of State and Parameter Estimators for Electric Vehicle Batteries. *IECON 2015*. IEEE.

4. Vellucci, F., Pede, G., Baronti, F., Di Rienzo, R., Cignini, F. (2016,June). Effects of fast charge on a lithium-ion battery system. *2016 Electric Vehicle Symposium & Exhibition 29 (EVS29)*. (pp. 19-22).

5. Di Rienzo, R., Baronti, F., Vellucci, F., Cignini, F., Ortenzi, F., Pede, G., Roncella, R., Saletti, R. (2016,November). Experimental Analysis of an Electric Minibus with Small Battery and Fast Charge Policy. *Esars Itec 2016*.

6. Morello, R., Di Rienzo, R., Baronti, F., Roncella, R., Saletti, R. (2016,October). System on Chip Battery State Estimator: E-Bike Case Study. *IECON 2016*. IEEE.

7. Morello, R., Baronti, F., Tian, X., Chau, T., Di Rienzo, R., Roncella, R., B. Jeppesen, Lin, W. H., Ikushima, T., Saletti, R. (2016,June). Hardware-in-the-Loop Simulation of FPGA-based State Estimators for Electric Vehicle Batteries. *25th International Symposium on Industrial Electronics (ISIE 2016)*.

8. Nannipieri, P., ... Di Rienzo, R., ... Filippeschi, S (2017,April). The U-PHOS experience within the ESA student REXUS/BEXUS programme: A real space

hands-on opportunity. *2017 Global Engineering Education Conference (EDUCON)*. IEEE.

9. Morello, R., Di Rienzo, R., Roncella, R., Saletti, R., Baronti, F. (June,2017). Tuning of Moving Window Least Squares-based algorithm for online battery parameter estimation. *2017 14th International Conference on Synthesis, Modeling, Analysis and Simulation Methods and Applications to Circuit Design (SMACD)*.

10. Di Rienzo, R., Baronti, F., Roncella, R., Morello, R., Saletti, R. (June,2017). Simulation platform for analyzing battery parallelization. *2017 14th International Conference on Synthesis, Modeling, Analysis and Simulation Methods and Applications to Circuit Design (SMACD)*.

11. Di Rienzo, R., Roncella, R., Morello, R., Baronti, F. and Saletti, R. (2018,January). Low-cost Modular Battery Emulator for Battery Management System Testing. *2018 1st International Conference on Industrial Electronics for Sustainable Energy Systems (IESES)*.

12. Litta, G., Di Rienzo, R., Morello, R., Roncella, R., Saletti, R. and F. Baronti (2018,January). Flexible platform with wireless interface for DC-motor remote control. *2018 1st International Conference on Industrial Electronics for Sustainable Energy Systems (IESES)*.

Contents

CHAPTER 1

Introduction

Electrochemical storage has come a long way from the invention of the first voltaic cell, better known as the battery, by Alessandro Volta in 1800. Gaston Planté invented the lead-acid cell in 1859, the first rechargeable battery that is still widely in use today. In 1991, the Sony Corporation, in collaboration with the Asahi Kasei Corporation, commercialized the first lithium-ion battery, which has monopolized the market of a low-power devices in very few years. Suffice it to say that, you have at least one lithium-ion battery in your pockets, on your desk or in your hands, while you are reading this thesis. In fact, all the tablets, laptops and smartphones are powered by lithium-ion batteries, because they are superior to all other rechargeable battery technologies with their high energy and power density, long cycle and calendar life, lower self-discharge, fast charging rate.

On the other hand, this technology must work in the safety operation area with respect to voltage, temperature and current, otherwise accelerated aging or even irreversible damages may show up. For this reason, the lithium-ion battery must be equipped with an electronic board, which monitors the battery and manages it to prevent unsafe situations. In literature, this board is usually called Battery Management System (BMS).

In present low-power applications, the battery is composed of one to four series-connected cells, with a nominal voltage in the range from $2.5\,\mathrm{V}$ to $4\,\mathrm{V}$ and a capacity from several hundreds of milliAmpere hour to a dozen of Ampere hour. Instead, in high-power applications such as electric or hybrid vehicles, renewable energies, and Uninterruptible Power Supply (UPS), the battery is composed of hundreds of cells with a capacity of even dozens of Ampere hour. Sometimes, the capacity requested to the battery is not obtainable with a single string of series-connected cells. For this reason, the battery can be composed of series and parallel-connected cells in some different

architectures. For example, the cells can be divided in groups of parallel-connected cells, which are then series-connected to build the battery. Another possible solution can be to parallel-connect some strings, composed of series-connected cells. The chosen architecture influences the performance, the cost, and the flexibility of the battery and introduces some problems which are dealt with in detail in the following chapters. In these applications, another key factor of the battery design is the architecture of the BMS which will have to handle some hundreds of cells. A hierarchical modular architecture has been proposed, realized, and tested in this work using an electric minibus as case study. The automotive industry is one of the most interesting fields for the lithium ion battery systems. Usually, the main investment is aimed to develop a battery system for electric or hybrid cars, but there are a lot of small vehicles where this technology can introduce undeniable advantages. For example, the characteristic of the public transportation, which is characterized by some predefined routes interspersed by a dwell time due to the boarding and alighting of the passengers, fits in perfectly with the lithium ion characteristics. In fact, the high charging power allowed by this technology can be used to recover all or a considerable part of the used energy in the route during the dwell times. This fast charge policy allows to reduce the size of the bus battery that must guarantee the runtime to run the longest distance among bus stops, and then its cost. To analyze the real benefits of this policy, a specific battery system has been developed to power an electric minibus, presenting in this work the most important design choices and experimental results.

Between the low and the high-power applications, there are a very large number of applications in which the lithium-ion batteries have been introduced many advantages in the last years. For example, small electric vehicles, such as bike, scooter, and Segway, but also tools for various applications of gardening, housework, building, cleaning the streets, and so on. These kind of applications are usually characterized by a low cost and production volume, if they are compared with the low and high-power applications. Moreover, these systems are small and must not be heavy because their weight must often be supported by the user for long time. For this reason, the manufactures prefer to power them with a small removable battery that is swapped when empty with a fully charged one, increasing the application runtime. So the user should acquire a tool and several batteries which have a cost comparable, or even higher, than the tool. The manufacturer trend is to propose a family of tools that can be powered by the same battery, so that the user can reuse the same set of batteries for many tools.

One of the results achieved during this Ph.D. study is the generalization of this concept, as we have proposed a standard “universal” and smart battery that can supply a large number of tools with different energy and power requirements. The battery can be parallel-connected to another one like it, to supply applications with requests of power and energy not compatible with a single battery. Putting in parallel to power sources introduces some issues. In fact, a very high current could flow from the most charged battery to the other, if the parallel is established when the battery internal states are not identical. A simulation platform has been proposed to study these problems, to individuate the unsafe conditions and to draw the best hardware and software solutions for a safe parallel-connection of the batteries. The solutions, checked by simulations, have then been validated by experimental realizations that have shown their validity from both the scientific and industrial point of view.

As already briefly mentioned above, the thesis aim is the study of design methodologies and architectures for the realization of lithium-ion battery systems for medium and high-power applications, presenting some design approaches to develop an innovative BMS and its smart integration into these applications. Therefore, the thesis first presents a background analysis chapter, in which the lithium-ion technology, the BMS design issues and their most common solutions have been presented. To analyze these solutions and develop new ones, some simulation platforms and hardware-in-the-loop setups have been designed and presented in the third chapter. They are very useful to compare the proposed solutions and analyze their performance before the implementation in a real system, with a significant reduction of cost and time. The fourth chapter analyzes an innovative hierarchical modular approach to compose a battery connecting standard modules in series and parallel. The design and implementation of the traction battery of an electric minibus that allows a fast charging policy is shown in the fifth chapter. The sixth chapter reports the validation of the design of the smart parallelizable standard battery and the implementation of a demonstrator to analyze its performance. The final considerations and some interesting food for thought are summarized in the conclusion chapter.

CHAPTER 2

Background

The aim of this chapter is to summarize the fundamental pieces of information about the electrochemical storage, and more in details about the lithium-ion technology, in order to draw the background from which the new methods of battery design have been developed. In particular, the characteristics of the lithium-ion technology characteristics have been analyzed and compared to the other electrochemical storage technologies, highlighting the main issues of their usage. In order to study the latter, it is paramount to know the response of the battery with respect to different stimuli, therefore a simulative approach is usually adopted in the battery development. For this reason, an analysis of the lithium ion battery models has been presented in this chapter, focusing on the electrical model that is the most commonly used.

The lithium-ion battery must be equipped with an electronic control system, as will be clear at the end of the first section, called Battery Management System (BMS) [59]. Its essential characteristics have been presented in the second section of this chapter, in which we have also highlighted the most important aspects that must be considered during its design.

2.1 Lithium-ion batteries

In the last years, many electric energy storage technologies have been proposed in the literature to satisfy the increasing needs of efficient and affordable means for the local storage of energy, in order to enable applications that start from the portable electronics and mobility scenarios to the stationary applications, even pushed down to the residential scale [35, 76]. The most used electrochemical storage devices are the batteries, particularly based on the lead acid, the nickel–metal hydride (NiMH) and the lithium-ion technology, which are briefly compared in Table 2.1 [43].

Table 2.1: *Performance comparison among various energy storage devices [43]*

	Temperature [°C]	Energy [W h kg^{-1}]	Power [W kg^{-1}]	Voltage [V]	Self-discharge [%/Month]	Cycle life 80-20%DOD	Cost estimation $/kWh	$/kW
Lead Acid	-30-60	20-40	300	2.1	4-8	200	150	10
NiMH	-20-50	40-60	1300-500	1.2	20	>2500	500	20
Li-ion	-20-55	100-200	3000-800	∼3.6	1-5	<2500	800	60
Electric Double Layer Capacitor	-30-65	5-20	1500	∼2.5	30	Not app	2000	50

The lithium-ion technology offers the most promising characteristics, such as the best power and energy density values with respect to both weight and volume. Moreover, it presents a very low self-discharge rate and a long cycle life. At the same time, as this technology is rather delicate with respect to the others, using Li-ion batteries requires an accurate control of the operating conditions, in terms of voltage, current and temperature, to avoid physical damages, accelerated aging and thermal runaways [73, 89]. Therefore, the lithium-ion batteries are always equipped with an electronic system called Battery Management System (BMS), which monitors and controls the cell operating conditions avoiding unsafe situations. Thus, a Li-ion battery system always consists of a BMS and a given number of battery cells, properly connected in series and/or parallel. The lithium-ion cell is composed of two electrodes each one consisting of a current collector connected to the anode and cathode materials, respectively. Between the electrodes, there is a polyolefin-based separator that is soaked with an electrolyte and allows the electronic separation and the ionic conduction between cathode and anode.

Figure 2.1 shows the schematic illustration of a lithium-ion battery with the charge and discharge mechanisms [67]. Li-ions travel back and forth inside the battery, while the electrons are conducted through the outer circuit, during the charge and discharge processes. The most common materials used for the lithium-ion cell realization are reported in Table 2.2 [92], for several variants of the lithium-ion battery chemistry, which mainly differ in the cathode material.

Table 2.2: *Major components of lithium-ion batteries and their properties [92]*

Abbrev	**LCO**	**NCA**	**NMC**	**LFP**	**LTO**
Name	Lithium Cobalt Oxide	Lithium Nickel Cobalt Aluminum oxide	Lithium Nickel, Manganese Cobalt Oxide	Lithium Iron Phosphate	Lithium Titanate
Positive electrode	$LiCoO_2$	$Li(Ni_0, 85Co_0, 1Al_0, 05)O_2$	$Li(Ni_0, 33Mn_0, 33Co_033)_2$	$LiFePO_4$	LMO, NCA
Negative electrode	Graphite	Graphite	Graphite	Graphite	$Li4Ti_5O_{12}$
Cell voltage (V)	3.7-3.9	3.65	3.8-4.0	3.3	2.3-2.5
Energy density (Wh/kg)	150	130	170	130	85
Power	High	High	Normal	High	Very High
Safety	Low	Normal	Normal	Very High	Very High
Lifetime	Low	High	Normal	High	Highest
Cost	Low	Normal	Normal	High	Normal

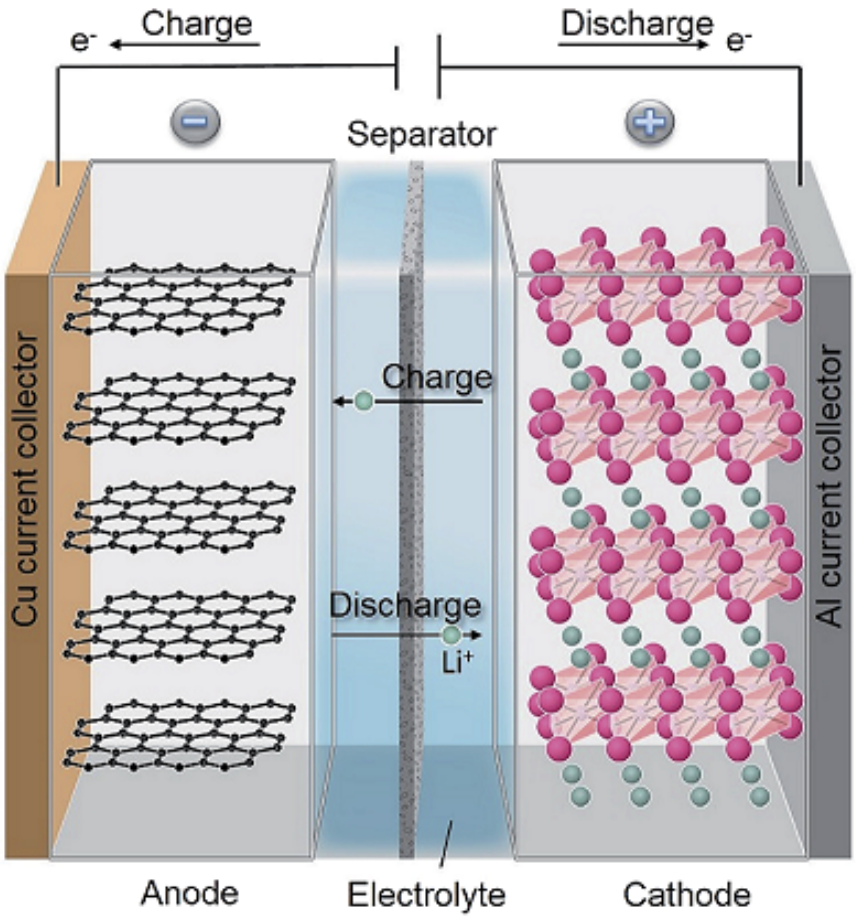

Figure 2.1: *Schematic illustration of a lithium ion battery showing charge/discharge processes [67].*

We can note that the Lithium Nickel Manganese Cobalt oxide (NMC) has the best energy density, so it is used in low/medium-power portable devices, in which the battery weight and volume are prominent figures of merit. Instead, the Lithium Iron Phosphate (LFP) technology is safer than the NMC [24] and presents the best trade-off between energy density and lifetime. These characteristics make them affordable in the large format batteries, as those typically used in high energy applications [6]. Considering the rather low cell voltage value and the other characteristics of the lithium-ion technology, a battery is usually composed by assembling a battery pack consisting of a variable number of elementary cells connected in series and/or in parallel to obtain the battery voltage and capacity that match the application requirements. As mentioned before, a BMS usually realized as an electronic control board controls the pack. Unfortunately, connecting in series and in parallel the elementary cells to develop a battery introduces some issues, such as the unbalance of the energy stored in the series-connected cells and the distribution of the current in the parallel-connected ones.

The first issue is very important especially in batteries composed of many series-connected cells, because it reduces the total energy that can be stored in the battery and may heavily affect the performance of the application in which the battery is used. This happens because the charge stored in the series-connected cells can change du-

ring the battery life, although the same current flows into them and they are initially charged with the same energy. This is caused by mismatches in cell capacity, internal resistance, chemical degradation, and inter-cell and ambient temperatures during the battery operation [21]. Figure 2.2 shows that the charge unbalance reduces the total capacity of the battery. As the Li-ion cells do not withstand over or under voltages, the charging and discharging phases must be stopped when the most charged and the less charged cells reach their voltage thresholds, even if the others have not reached the maximum or the minimum charge level yet. Therefore, the battery remains partly recharged and partly discharged, respectively, never reaching the full exploitation of the entire nominal capacity.

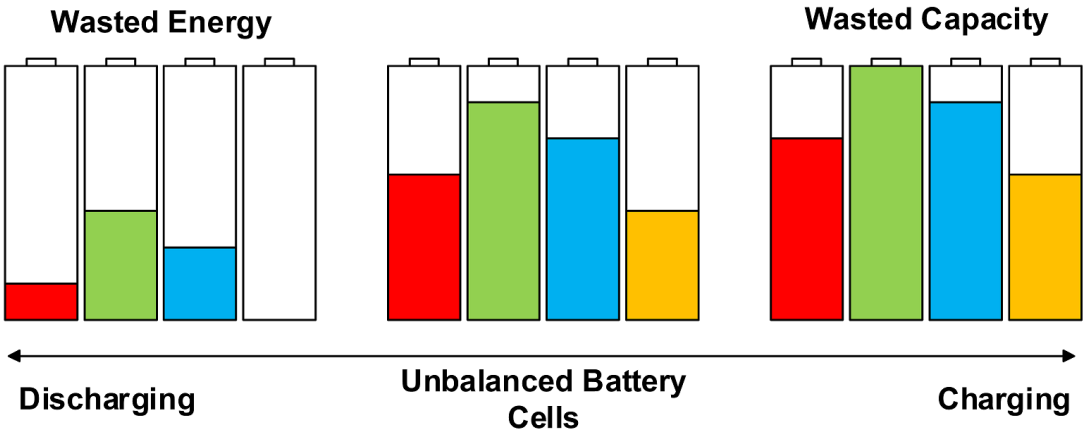

Figure 2.2: *Energy and capacity loss under cell unbalance situation [77].*

For this reason, the BMS must take care of this phenomenon also, by executing a function that makes the battery cells balanced again in the stored charge. In a parallel-connected cell group, mismatches between the characteristics of nominally identical cells lead to an uneven distribution of the current among the cells and this can impact on their aging [40]. For this reason, battery pack manufactures are used to screen the cells and find those best matched, before they are parallel-connected. Typically, the cells are connected together when the battery is manufactured and no changes are applied for all the battery life. However, the cells could dynamically be connected to increase the flexibility of the battery, allowing the battery voltage and capacity re-configurability. In this case, the parallel-connection of two cells, or two groups of series-connected cells, or even of modules of cells is not always possible. In fact, a large current can flow in the connection if the parallel is established when the voltage difference between the two groups is not minimal [38]. This is due to the very low ohmic resistance of the lithium-ion battery. For this reason, paralleling cells, groups or modules poses new challenges to the BMS that needs specific hardware and software solutions for the realization of reconfigurable batteries in which the parallel is executed in a safe and controlled way.

The most common quantities utilized for the characterization of the batteries are reported in the following:

- Nominal voltage (V_{n}): the voltage measured between the cell terminals when the charge has an average value and the current is zero.

- Nominal capacity (Q_{n}): the charge drained from a fully charged cell to completely discharge it [100].
- Maximum charging/discharging current: the maximum current values that can flow into the cell without damages, usually indicated in C-rate. 1 C-rate is the current value equal to the nominal capacity of the battery, *i.e.*, the current that discharges a fully charged battery in one hour [28].

Other important quantities for a battery are the State-Of-Charge (SOC) and the State-Of-Health (SOH). The first is defined as the charge stored in the cell normalized to the nominal capacity [72, 82, 103]. Instead, the definition of the SOH is more complex and is not univocal in the literature. Usually, it is related to the measured cell capacity normalized to Q_{n}, which accounts for the capacity degradation, and to the cell series resistance normalized to the resistance of a fresh cell [8, 93].

2.1.1 Cell Modeling

The knowledge of the response of a battery cell, and the corresponding battery pack when the cell is assembled with others, would be very useful for the evaluation of the performance of the battery itself and for the optimal design of the BMS. A common methodology adopted in many engineering fields is to describe the behavior of the device of interest by means of a model that reproduces the device behavior. Many models to describe the behavior of the lithium-ion cells have been presented in the literature [27, 46]. The most popular models can be divided into three different typologies:

- Electrochemical models: they use the equations that describe the cell chemical reactions to obtain a very accurate prediction of the cell behavior as function of voltage, current, temperature and microscopic quantities, such as the ion concentrations [69, 83, 98]. For this reason, the model requires many physical data in order to determine the coefficients of the electrochemical equations at the microscopic level. Moreover, it is very complex and thus requires a high computational power [37].
- Mathematical models: the cell behavior is estimated with empirical equations, which sometimes are not directly related to the chemical-physical reactions. Therefore, they enable the description of the cell under particular conditions but they are not able to predict all the possibilities [26, 75].
- Electrical models: they describe the relation between the macroscopic quantities of the cell (voltage, current and temperature) by using an electrical equivalent circuit. These models are very intuitive and the complexity is linked to the required accuracy. For this reason, they are the most used models in the development of the BMS hardware, control strategies and state estimation algorithms [54, 65, 70].

The most common Electric Circuit Model (ECM) is shown in Figure 2.3 [65]. It is composed of two parts: the left hand side consists of a linear capacitor, whose value is equal to the nominal cell capacity Q_{n} (expressed in Coulomb) divided by $1\,\mathrm{V}$, and a dependent current generator controlled by the cell current. This part of the circuit models the energy stored in the cell, in which the value of the capacitor voltage is the cell SOC multiplied by $1\,\mathrm{V}$. Sometimes, a resistance is parallel-connected to the

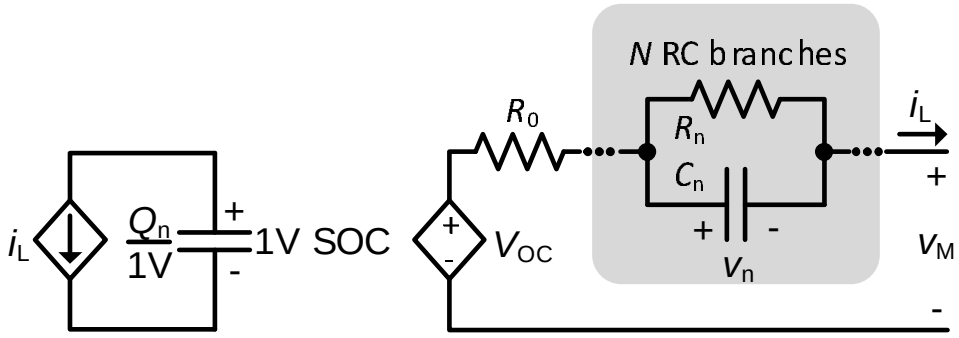

Figure 2.3: *Electrical equivalent model.*

capacitor to model the self-discharge of the cell. It is important only in the studies in which a very long simulation time is used, because the lithium-ion technology presents a self-discharge rate of about $3\,\%$ per month. For this reason it is usually neglected in most cases of study. In the right hand side of the circuit, the outer cell voltage is the sum of two terms: the open-circuit voltage (OCV) and a term which accounts for dynamic phenomena. The first contribution can be estimated using the relationship between the OCV and the cell SOC, which is usually considered independent of the other operating conditions (*e.g.* current and temperature) [71]. The dynamic term incorporates the voltage drops on the internal ohmic resistance R_0 and on one or more RC groups. A good compromise between complexity and accuracy is obtained with two RC groups that model the double layer and diffusion effects occurring in a Li-ion battery during charging and discharging [51]. In applications where the aim is to predict the cell voltage response to fast transients with a good accuracy and long term phenomena may be neglected, the model is applied with a single RC group only [39]. This simplified model is suitable to be executed in embedded systems with a rather low computational power. In this case, the cell time-domain state space model is the following:

$$\begin{cases} \dfrac{dSOC}{dt} = -\dfrac{i_{\mathrm{L}}}{Q_{\mathrm{n}}} \\ \dfrac{dv_1}{dt} = -\dfrac{v_1}{\tau_1} + \dfrac{i_{\mathrm{L}}}{C_1} \\ v_{\mathrm{M}} = OCV - R_0 i_{\mathrm{L}} - v_1 \end{cases} \tag{2.1}$$

where $\tau_1 = R_1 C_1$. The parameter of the dynamic term of the model strongly depends on the cell temperature [45]. Thus, the electric cell model is often applied in combination with a simple thermal model, which is able to predict the cell temperature by taking into account the electric power dissipated in the cell and the thermal resistances to the ambient.

The thermal dependency makes it necessary to have a complete characterization of the cell for different temperatures to obtain a large bunch of experimental data from which the parameters for a good cell behavior emulation can be extracted. A procedure to extract the parameter dependency from the temperature is studied in [10, 11], in

which the authors have developed a custom thermostatic chamber by which the surface temperature of the cell can be set. They perform characterization tests called Pulsed Current Test (PCT) at different cell temperatures in which profiles consisting of current pulses of given duration are applied to the cell [45]. The PCT was repeated for several temperature and current values obtaining for each parameter a 3 dimensional lookup table (LUT), which describes the dependency with respect to the temperature, SOC and current.

2.2 Battery management system

Given the characteristics of the Li-ion cells and the issues that arise in connecting the elementary cells to each other described above, the features and the functions of a BMS, particularly the most advanced of them, can be described. As already pointed out before, the main scope of a BMS is to monitor the battery behavior and thus to maintain the battery cells in the safe operating area (SOA) in terms of voltage, current and temperature [1]. To this end, it must be able to measure these quantities and to control the system according to the measurements and the protection policy applied. The BMS is usually composed of one or more electronic boards and it is able to communicate with the main control unit of the application for an optimized battery use. More in general, the most important BMS functionalities are summarized in Figure 2.4 and will be explained in detail in the following paragraph.

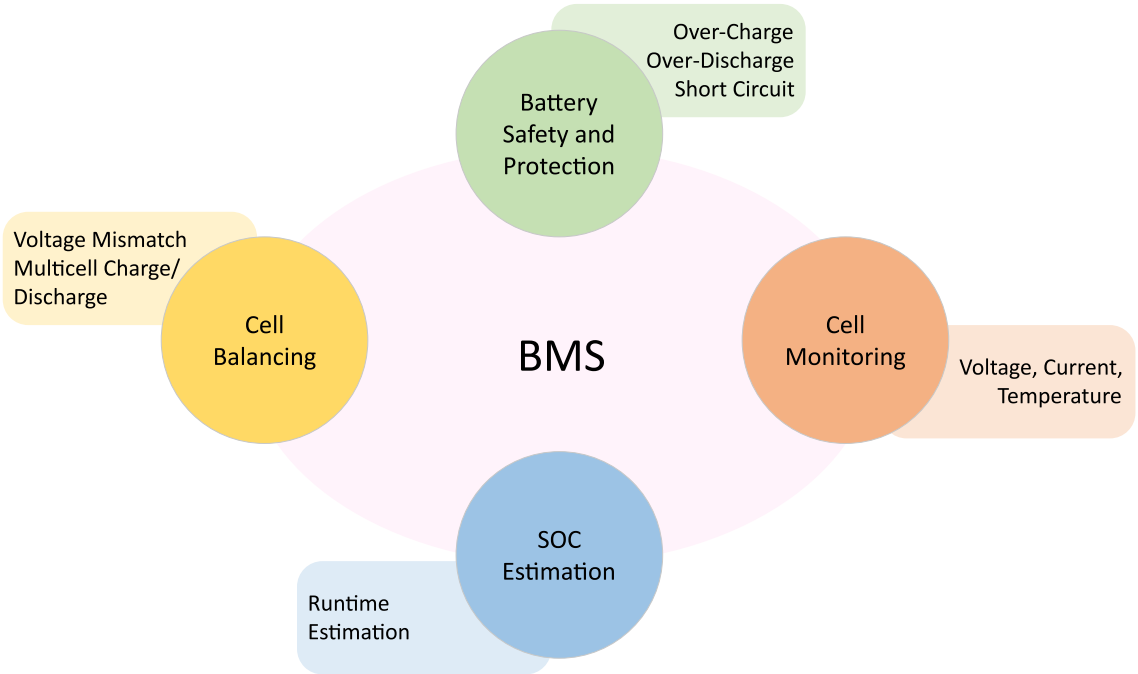

Figure 2.4: *The most important Battery Management System features.*

As far as the architecture of the BMS is concerned, the best solution to obtain an optimal BMS changes with the battery size and the application in which the battery is used [73]. In small size batteries, the functionalities of the BMS can be centralized on a single board to reduce the system complexity and cost. Instead, a distributed

approach in which the BMS functionalities are distributed over separate layers is more appropriate for applications that require a large-format battery. In the last case, the BMS can be divided into a group of boards, in which each board manages a group of cells, implementing all the BMS functions. The single board is connected to the others to compose the BMS. A hierarchical distributed approach is the most promising solution to make a very robust and flexible BMS [12,50,86]. The hierarchical approach is based on the BMS function distribution between a variable number of hierarchical levels, with the possibility to duplicate some functionalities on more levels in order to increase the system robustness [96]. Each level can be composed of one or more boards.

For example, the authors have presented in [18] a hierarchical BMS for a HEV divided in three hierarchical levels: the Cell Management Unit (CMU), the Module Management Unit(MMU), and the Pack Management Unit (PMU). Its block diagram is shown in Figure 2.5. The CMU manages the single cell by monitoring its voltage and temperature [17]. A group of 11 series-connected cells with the relevant CMU is controlled by an MMU, which collects the data measured by the CMUs and sends them to the uppermost level of the hierarchy. In fact, all the MMUs are connected to a PMU that controls the battery behavior and optimizes its usage in according to the main unit of the application.

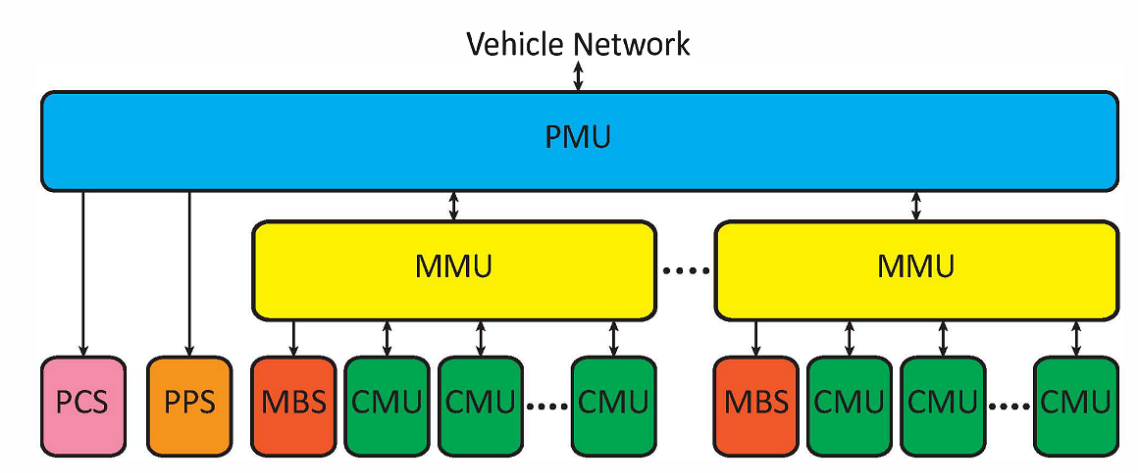

Figure 2.5: *Block diagram of the hierarchical BMS. Acronyms used are: Pack Management Unit (PMU). Pack Protection Switch (PPS). Pack Current Sensor (PCS). Module Management Unit (MMU), Module Bypass Switch (MBS), Cell Monitoring Unit (CMU) [18].*

2.2.1 Cell monitoring

The fundamental safety function the BMS is asked to carry out is avoiding the unsafe situations of cells working out of their SOA. For this reason, the knowledge of the cell voltage, temperature and current is required. The measurement of these quantities is usually performed utilizing three different circuit structures: a custom analog front-end, a commercial battery monitor integrated circuit or a mix of the two solutions [56,87]. A custom solution improves the flexibility of the system but also increases its complexity. Therefore, it is usually adopted at the lower level of a hierarchically

distributed architecture, where the board monitors a low number of cell (up to 4). This solution is often based on resistor based voltage dividers that adapt the cell voltage in the input range of the voltage sensor. On the other hand, dedicated integrated circuits for battery monitoring have been proposed on the market to monitor series-connected cells [96]. They can measure up to 16 cell voltages, the temperature in some points and often the cell current as well. For example, the LTC6803, manufactured by Linear Technology, measures the voltage of up to 12 series-connected cells and the temperature in two points. This chip can be controlled through a SPI interface with which the monitoring system is configured, the measurements are started and the acquired quantities are read. Moreover, it can also be used in a battery composed of a number of cells exceeding the capacity of the single chip, as more chips can be stacked, making it useful in both the centralized and distributed BMS architectures. A mix of the custom and commercial solutions can be applied to expand the functionalities of the dedicated chip or to add some missing functions [101]. For example, the LTC6803 must be equipped with a custom analog multiplexing front-end to allow it to acquire all the cell temperatures, and a dedicated circuit must be added to measure the cell current.

2.2.2 State-of-Charge estimation

One of the most valuable items of information that is needed when a battery is employed in an application is the knowledge of the battery State-of-Charge, *i.e.*, the residual charge that can be extracted from the battery. This is one of the most important indicators of the state of a lithium-ion cell because it is strictly related to many important features of the battery system of an application, such as the battery State-Of-Energy (SOE) that determines the application runtime. A definition of the cell SOC has been provided in the previous Section as the ratio between the charge contained in the cell and its nominal capacity [72]. However, a definition of the SOC of a battery composed of more cells is hardly definable . In fact, the capacity of a battery depends on the distribution of the charge among the cells, on the organization of the parallel/series cell connections and so it is difficult to define the maximum extractable charge. For this reason, the BMS executes mathematical algorithms to approximate the value of the battery SOC starting from the SOC of each cell. Moreover, the SOC value of a single cell is not directly measurable and its computation is demanded to an algorithm executed by the BMS that uses the quantities acquired directly from the cells, such as current and voltage, to compute the SOC. Many different algorithms have been proposed in the literature for the computation of the SOC [61, 103]. The most common used solutions are analyzed in detail in the following subsections.

Open Circuit Voltage method

The easiest method is based on the open circuit voltage measurement [73]. The OCV depends on the SOC, but it can be considered almost constant with respect to temperature and aging [71]. However, the cell voltage response to current variations is strongly affected by dynamic phenomena and so the voltage relaxes to the OCV only after the cell current has been equal to zero for a long time, *i.e.*, the relaxation transient phenomena are elapsed. Thus, this technique cannot be used in highly dynamic systems, characterized by a variable battery load profile.

Coulomb-Counting method

The Coulomb-Counting (CC) method is one of the most diffused techniques for measuring the SOC of a cell. It directly uses the definition of SOC, by measuring the extracted/inserted charge from the time integration of the cell current (i_{L}), and by normalizing the obtained value to the nominal capacity of the cell (Q_{n}):

$$\mathrm{SOC}(t) = \mathrm{SOC}_0 - \frac{1}{Q_{\mathrm{n}}} \int_0^t i_{\mathrm{L}}(\tau) d\tau \tag{2.2}$$

where SOC_0 is the value of the SOC for $t = 0$ [7].

This technique is very easy to implement and poses a very low computational burden, so it can be employed in low cost systems. The obtained estimation can be very accurate, but it is strictly dependent on the accuracy of the current measurement because of the integration process. In fact, the integration of the current can diverge if the current measurement is affected by errors, like an offset in the current sensor [58]. Furthermore, the values of the initial SOC and of the maximum storable charge are difficult to estimate, because they depend on the State-of-Health and the aging of the cell, respectively. A solution to these problems can be a periodical calibration of the algorithm when the battery stands in a known state, but it is only possible in some kinds of application.

An interesting method to calibrate the SOC estimation is combining the CC method with the Open Circuit Voltage one. In fact the latter can be used to obtain the SOC_0 and so to reset the integration of current when the battery is not in use [47].

Model based estimation

Many algorithms for SOC estimation have been presented in the literature to overcome the problems of the CC technique. For example, accurate methods are based on a mathematical battery model (artificial neural networks and fuzzy logic approaches) [26], but they are computationally intensive and require long training procedures.

In applications where high accuracy and reliability are required (*e.g.*, automotive field) and where the algorithm must be executed in real-time in an embedded system (like the BMS), a good solution is the use of model-based algorithms. Examples of model based algorithms are the Extended Kalman Filter (EKF) [74, 88], Particle Filters [79, 103], the Mix Algorithm [29] and the Adaptive Mix Algorithm (AMA) [64]. These techniques use a model of the cell in a closed-loop to correct the CC estimation of the SOC, by comparing the model predicted voltage to the measured one. Various kinds of model can be used, but the ECM is the most promising to use in a real-time embedded system, because it can provide good accuracy with affordable complexity [27]. However, the variation of the ECM parameters with the operating conditions must be taken into account for an accurate SOC estimation [13]. A possible solution is the adoption of Look-Up Tables (LUTs) in which the parameter values are stored and used depending on the actual operating point. This implementation requires low computational resources but also a very extensive offline characterization, since the model parameters are extracted after the realization of time consuming tests [11]. Furthermore, parameter variations due to manufacturing process tolerances and aging of the battery can hardly be modeled this way, as the LUT contains data relevant to a typical cell

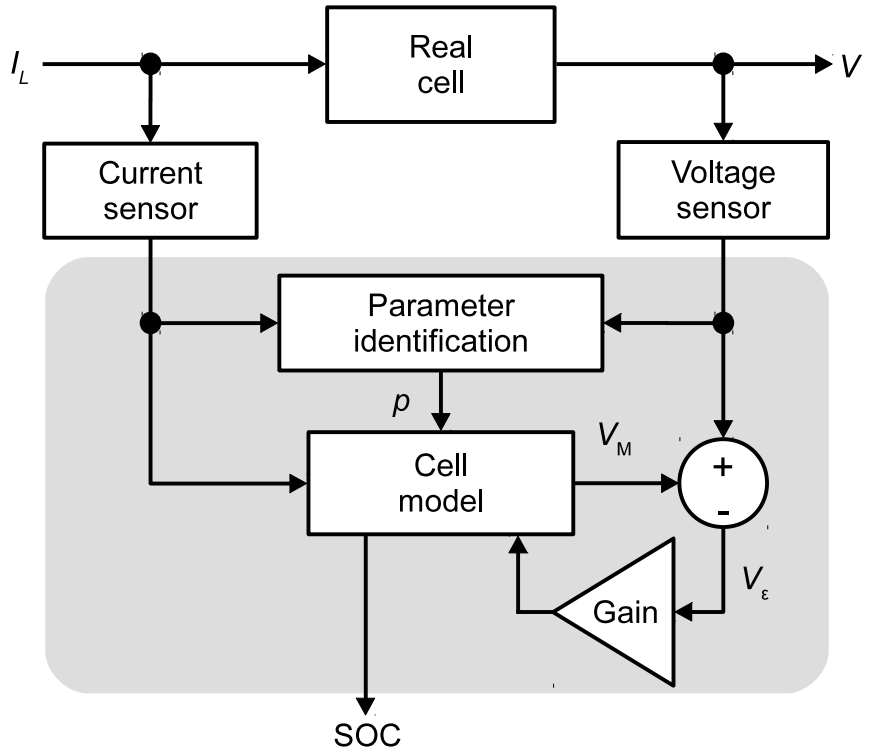

Figure 2.6: *Block diagram of the model-based algorithms.*

behavior. A good approach to face the above issues is to track the parameter variation online, which is the solution adopted in the Dual-EKF [65] and in the Adaptive Mix Algorithm techniques. Figure 2.6 shows the block diagram of the model-based approaches where the model parameters are continuously updated to follow their variations induced by changes in the battery operating conditions and aging.

Adaptive Mix Algorithm

The AMA is based on the combination of the Mix Algorithm and the Moving Window Least Square (MWLS) methods used with the AutoRegressive eXogenous (ARX) structure of the ECM. It is presented in [63], where the authors implement a BMS based on a Field Programmable Gate Array (FPGA) equipped with an AMA hardware estimator for the SOC estimation. Its working principle is shown in the block diagram seen in Figure 2.7.

The authors use the same electrical circuit model shown in Section 2.1.1 with a single RC group in order to keep the needed computational power low. The OCV-SOC relationship has been implemented with a LUT. The model is used to predict the cell voltage v_{M} that is then subtracted to the measured cell voltage v_{T} to obtain an error signal. The latter is firstly amplified by the observer gain L and then used to correct the measured cell current i_{L}. The SOC is obtained by integrating the corrected current signal over time. The observer gain L is chosen to reduce the effects due to a bad SOC initialization and current measurement errors [19].

The estimation accuracy depends on the capability of the ECM to reproduce the cell

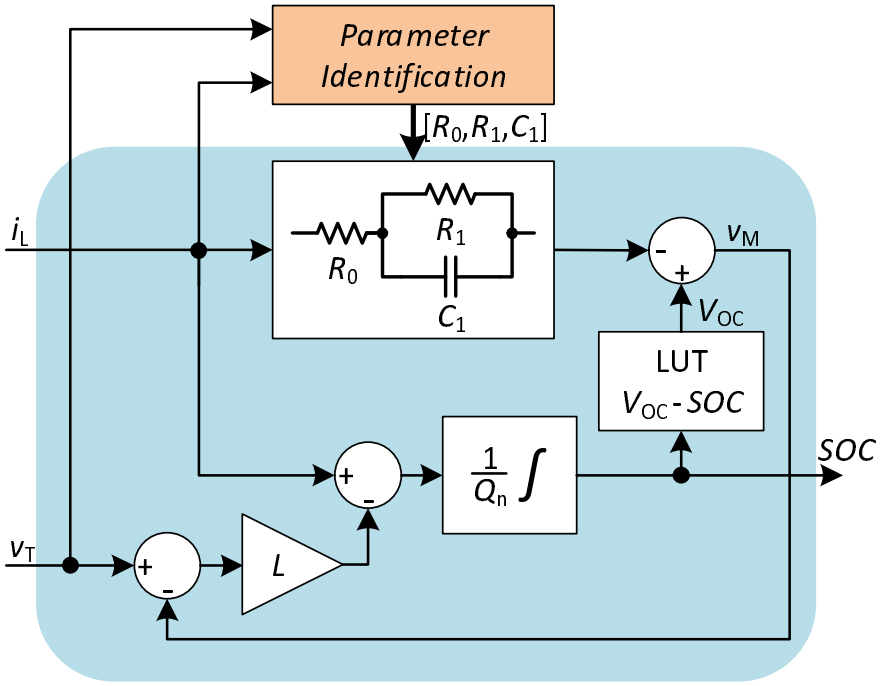

Figure 2.7: *Functional diagram of the AMA algorithm [63].*

behavior. It can be improved by updating online the ECM parameters using the MWLS algorithm, implemented in the Parameter Identification block. In this way, the algorithm takes into account the parameter variations due to the battery aging, the operation conditions (as cell SOC and temperature) and the manufacturing process tolerances. The ARX structure can be obtained starting from the cell time-domain state space model reported in Eq.(2.1). The cell operating point slowly changes over time, so that the model can be linearized around it, considering the parameters constant in the identification window. The OCV-SOC relationship is thus approximated by a piecewise linear curve OCV = α_0 + α_1 SOC, where α_0 and α_1 depend on the operating point. The discrete-time transfer function is obtained by the application of the bilinear transform to the transfer a function from the current input to the cell voltage output, as obtained from the state space model:

$$\frac{Y(z^{-1}) - \alpha_0}{U(z^{-1})} = -\frac{b_2 z^{-2} + b_1 z^{-1} + b_0}{a_2 z^{-2} + a_1 z^{-1} + 1} \tag{2.3}$$

where $Y(z^{-1})$ and $U(z^{-1})$ are the z-transforms of the voltage output v_{T} and current input i_{L}, respectively. Then, the discrete-time relationship between the input and output samples is the following:

$$\begin{aligned} y(k) = &- a_1 y(k-1) - a_2 y(k-2) + \alpha_0(1 + a_1 + a_2) \\ &+ b_0 u(k) + b_1 u(k-1) + b_2 u(k-2) \end{aligned} \tag{2.4}$$

which is a second order ARX model of the cell, where k is the discrete time. The authors

demonstrate that $1 + a_1 + a_2 = 0$ by analyzing the dependency of the coefficients of the ARX model on the ECM parameters, so the previous equation can be reduced to:

$$\begin{aligned} y(k) - y(k-2) =& a_1(y(k-2) - y(k-1)) + b_0 u(k) \\ &+ b_1 u(k-1) + b_2 u(k-2) \end{aligned} \tag{2.5}$$

The last equation is used to build an overdetermined system by using the current and voltage samples within a time window. The system is solved using the Least Squares (LS) method, and the resulting vector $[a_1, b_0, b_1, b_2]$ is used to compute the ECM parameter vector $[R_0, R_1, C_1]$. The window is shifted in time to track the parameter variations during the cell operation.

Dual EKF

The Kalman Filter uses a set of measurements acquired over time to estimate the unknown state variables of a system. In the case of the lithium-ion cell SOC estimation, in which the ECM with a single RC group is used, the state vector can be composed by the SOC and the voltage across the RC group together whit the parameters of the ECM. This approach is called joint estimation in the literature. On the contrary, the Dual EKF (DEKF) technique is based on two cooperating Kalman Filters for non-linear systems, one for the state and another for the parameter estimation [64, 90]. The use of a dual estimation, instead of a joint estimation (in which only one Kalman Filter is used), reduces the state matrix dimensions and may improve the estimation robustness [80]. The parameter evolution is described by the process equation (2.6), which is used in combination with the measurement equation (2.8), in order to build the first EKF. Instead, the state evolution is represented by Eq.(2.7), which is again combined to the measurement equation (2.8) to form the second EKF.

$$p(k+1) = p(k) + \chi(k) \tag{2.6}$$

$$x(k+1) = F(x(k), i_{\mathrm{L}}(k), p(k)) + \xi(k) \tag{2.7}$$

$$v_{\mathrm{T}}(k) = G(x(k), i_{\mathrm{L}}(k), p(k)) + \psi(k) \tag{2.8}$$

The measurement equation (2.8) is the same for both filters. The measurement operator G is non-linear because of the non-linear relationship between OCV and SOC. These equations derive from the state space model of equation (2.1). In the above equations, k is the discrete time, p is parameters vector, x = [SOC; v_1] is the battery state vector. χ, ξ and ψ are the noise on the parameters, the state, and measurement, which have zero mean and covariance matrices Q_{q}, Q and R, respectively. The EKF recursively repeats two steps. First, the filter computes the estimate of the state variables and of their uncertainties during the prediction step. Then, these estimates are corrected by using the measured quantities in the update step. The full DEKF process is as below:

1. Initialization

$$x_0, P_0, q_0, P_{q_0} \tag{2.9}$$

2. Prediction

$$q_k^- = q_{k-1}^+ \tag{2.10}$$
$$P_{q_k}^- = P_{q_{k-1}}^+ + Q_{\mathrm{q}} \tag{2.11}$$
$$x_k^- = f(x_{k-1}^+, u_{k-1}, q_{k-1}^+) \tag{2.12}$$
$$P_k^- = A_k P_{k-1}^+ A_k^T + Q \tag{2.13}$$

3. Correction

$$L_{x_k} = P_k^- C_{x_k}^T (C_{x_k} P_k^- C_{x_k}^T + R)^{-1} \tag{2.14}$$
$$x_k^+ = x_k^- + L_{x_k}(y_k - g(x_k^-, u_k, q_{k-1}^+)) \tag{2.15}$$
$$P_k^+ = (I - L_{x_k} C_{x_k}) P_k^- \tag{2.16}$$
$$L_{q_k} = P_{q_k}^- C_{q_k}^T (C_{q_k} P_{q_k}^- C_{q_k}^T + R)^{-1} \tag{2.17}$$
$$q_k^+ = q_k^- + L_{q_k}(y_k - g(x_k^-, u_k, q_{k-1}^+)) \tag{2.18}$$
$$P_{q_k}^+ = (I - L_{q_k} C_{q_k}) P_{q_k}^- \tag{2.19}$$

The DEKF can provide very good results, but the determination of the covariance matrices to be used in the algorithm is very tricky and it is usually performed by using an empirical approach [62].

2.2.3 Cell balancing

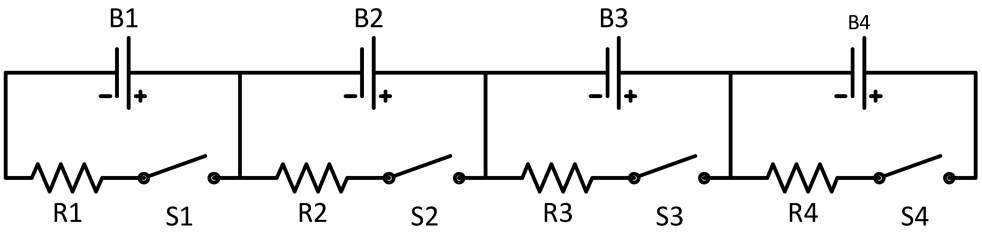

Figure 2.8: *The most simple passive balancing circuit [77].*

Let us now deal with another important problem found in series-connected batteries that the BMS is asked to manage and possibly to correct: the imbalance in the cell charges that arises from production mismatches and uneven operating conditions. As mentioned above, the problem of charge balancing has widely been studied in the literature and many charge balancing circuits have also been proposed [25, 32, 77]. The presented solutions can be divided in two families: the passive and the active topologies. Discharging the most charged cells with bleeding resistors is the techniques used to balance the stored energy of the cells in passive topologies. The simplest circuit is shown in Figure 2.8, where each cell can be parallel-connected to the bleeding resistor using a dedicated switch. Activating the switch lets the selected cell lose energy by Joule dissipation.

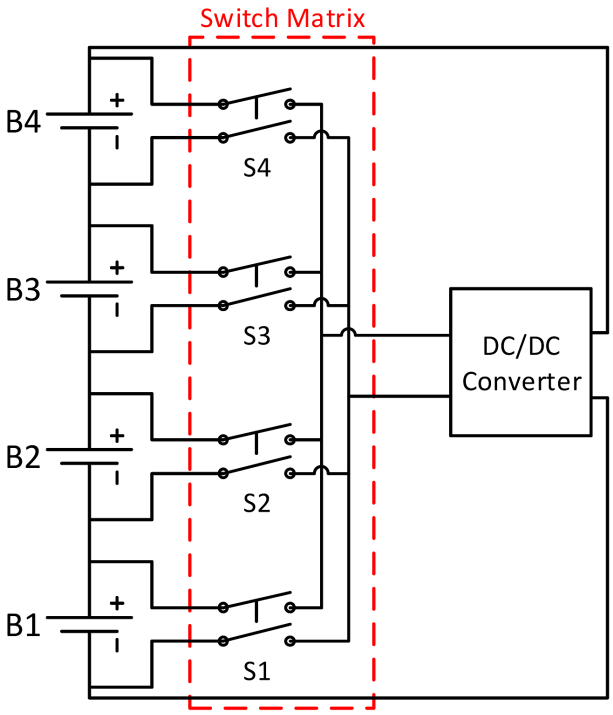

Figure 2.9: *Active battery to cell architecture balancing circuit based on DC/DC and switch matrix [77].*

The passive techniques are usually simple and cheap but require an appropriate thermal management, because the energy is dissipated as heat. For this reason, it is usually adopted only in medium/small format batteries and the resistors are sized to drain a limited current value, keeping the dissipated power low. As a drawback, the balancing time is usually rather high.

On the contrary, the active solutions aim at moving energy from the most charged cells to the less charged ones. These techniques can be divided into three categories: cell to cell, battery to cell, and cell to battery topologies. The first one directly moves energy between two cells of the battery, instead the second one utilizes the entire battery to charge the cell with the lowest energy. The opposite approach is used in the last solution, in which the energy of the most charged cell is distributed to the entire battery.

A promising active balancing approach is shown in Figure 2.9 and is based on the battery to cell architecture with a DC/DC converter powered by the battery voltage. Its output can selectively be connected to each cell by using a switch matrix, to provide the missing charge. The switch matrix control system is the most complex part, because one or more cells could be short-circuited if the switches were not correctly controlled. In the work [15], the authors presented a robust hardware logic driver to control the switches. It is used to avoid unsafe situations generated by an incorrect behavior of the balancing control software. Furthermore, they presented an interesting solution to apply the balancing approach to a distributed battery architecture also. In fact, the battery was divided into series-connected modules, each of them composed of 4 series-connected cells and equipped with a module management unit. Each MMU was provided with a charge equalized circuit, shown in Figure 2.10 and based on an isolated DC/DC converter powered by the module voltage that implements the battery

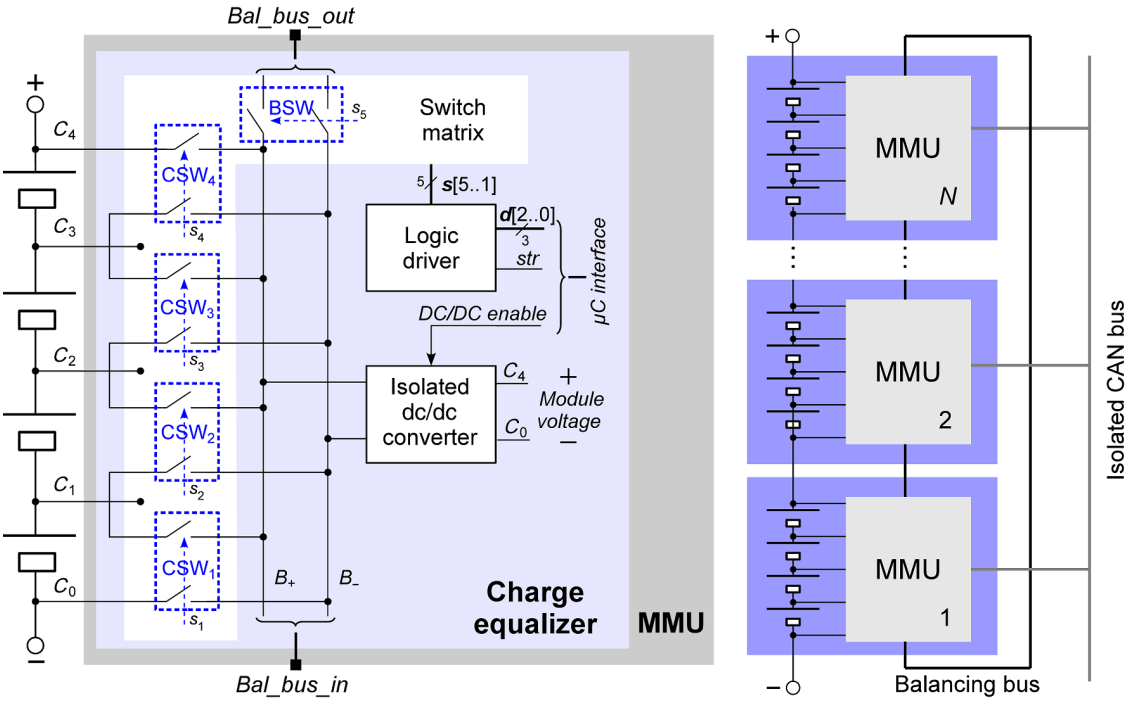

Figure 2.10: *Innovative active charge equalized circuit for a distrusted battery [15].*

to cell balancing topology. The peculiarity of this circuit is that the DC/DC output can not only be connected via the switch matrix to each cell of the module, but also to a global balancing bus that crosses all the modules as shown in Figure 2.10. In this way, a cell of another module can be recharged with the energy of another one, implementing an inter-module balancing.

CHAPTER 3

Platforms for Battery Management System development

In the previous chapter, we have shown the most important characteristics of the lithium-ion batteries, introducing their main issues and the most common solutions. Starting from this background, we have developed the innovative methodology of battery design that has been analyzed with simulative approaches in this chapter and applied to some interesting kinds of applications in the following chapters.

We have chosen to develop some dedicated simulation platforms to optimize the proposed methodology and provide a highly powerful tool for the battery design. In fact, this approach avoids the use of real lithium-ion cells in the development process, which can increase the development time and can lead to unsafe situations. The main part of these platforms is the cell model, used to emulate the cell voltage, whose complexity depends on the aim for which it has been developed. The most common used model is the equivalent circuit model, presented in Section 2.1.1, with one or two RC groups. The 1 RC group ECM is used to obtain a fast simulation in the cases in which we can accept a low precision in the simulation of the cell voltage. Instead, the 2 RC groups model allows us to obtain a good simulation accuracy with an increase of the simulation time [44]. The model parameters can be considered as constants to increase the simulation speed, or function of SOC, temperature and current to increase the model accuracy. The cell model is instantiated more times and arranged in an opportune way to obtain a cell pack model.

Usually, the simulation platforms can be divided in two categories: the software simulation platforms and the Hardware in the Loop (HiL) ones. The first platforms are developed as a part of firmware, in different simulation environments, such as MATLAB®, which is executed on a computer or in a dedicate system. Its aim is usually to demonstrate the potentialities of an algorithm, which can estimate the state of

the cell or control the behavior of the battery. On the contrary, the HiL platforms are composed of a hardware and software environment that can be used to emulate the realistic operating conditions, in which the BMS, or part of it, is used. In this way, it can test the implementation of the hardware and software parts of the BMS before that it is assembled on the cell pack. The HiL platforms can be categorized on the basis of the type of the signals provided as input to the BMS and in particular in according to the power exchange between the platform and the BMS [52]. In details, Power-HiL simulators generate the power flux from/to the battery cells, allowing the BMS hardware to be tested with or without employing a real cell or battery. The communication-based approach allows us to test only the software of the BMS by sending the simulated battery data (*i.e.*, current, voltage and temperature of each cell) to the main unit of the BMS via a communication link.

In the following sections, we have described three interesting methodology approaches and the three respective simulation platforms. The first one is the dynamic parallel-connection of the battery modules, which can introduce some remarkable advantages in the battery system design, as shown in the following chapters. This approach needs to be analyzed in-depth because it can involve unsafe situations that undermine the battery integrity. Therefore, a software simulation platform has been developed and presented in the first section of this chapter, where the details of this problem have also been explained. The second approach uses a Field-Programmable Gate Array (FPGA) to implement hardware accelerators with which to execute complex algorithms in time division multiplexing to estimate the internal state of a large number of cells, optimizing the battery usage. A communication-based HiL, based on an Intel FPGA and that emulates an electric vehicle system, has been developed. It allows the designer to develop, test, and compare novel algorithms in a controllable environment and with many repeatable stimuli. The remaining approach is focused on the BMS hardware and software test production phases. In particular, the last platform consists of a low cost Power-HiL to perform the end of line testing on a BMS, allowing it to increase the reliability of the battery.

3.1 Simulation platform for analyzing battery parallelization

When cells or batteries are parallel-connected, we need to pay particular attention to their mismatches in the State-of-Charge, capacity and internal resistance, because these may lead to degraded performances and accelerated aging [4]. Usually, the cell parallel-connection is hardwired [40], when the battery pack is assembled, whereas the parallelization of the battery strings (one or more batteries series-connected) is dynamically established and controlled in the software by means of dedicated power switches. This last solution makes the battery system more flexible and has allowed interesting design approaches as shown in Section 5.3 and in Chapter 6. This is a rather unexplored research topic, unlike the cell parallel-connection, which could definitely benefit from the availability of a simulation framework that can predict the battery system behavior in a wide range of operating conditions. Moreover, it can be used to develop, test and compare some parallelization algorithms which should maximize the battery lifetime and minimize the conduction losses over the internal resistance of the batteries and on the resistance of the parallelization switches.

In the following subsections, we propose an example of parallelization algorithm and a simulation platform to investigate the parallelization of two medium-format batteries effectively, which can also be easily generalized for a different number of batteries and with different size.

3.1.1 Parallelization algorithm

The key goal of the parallelization policy is to maximize the sharing of the current drawn by the load between the two batteries, while maintaining every battery cell inside the SOA. We note that at the beginning of the discharge, the two batteries are likely to have a different SOC. This yields a voltage mismatch that can cause a potentially harmful instantaneous current to flow from the most charged battery to the least charged one, if they are parallel-connected. This situation is not easy to be analyzed analytically, for this reason the simulation platform presented in the next subsection has been developed. However, it can be simplified to draw some general considerations which are useful to develop an efficient parallelization algorithm. In particular we can use the ECM with only the ohmic resistance (R_0) to model the battery cells and consider the parallelization of two batteries without any load. In these conditions the value of the current which flows into the two batteries is at maximum at the very moment in which they are connected together and it is equal to:

$$|I| = \frac{|V_1 - V_2|}{R_{01} + R_{02}} \tag{3.1}$$

where V_1 and V_2 are the voltages of the two batteries and R_{01} and R_{02} are their ohmic resistances. The flowing of this current balances the SOCs of the batteries because the most charged one recharges the other battery. In the equation, the contact resistances and the ones of the parallelization circuit have been neglected because their value must be very low to reduce the energy lost in the system connections. The value of this current is very high and it can easily exceed of the cell SOA because the divisor of the fraction is very low. In fact, the lithium-ion cells have a very low ohmic resistance which can go from hundreds of $\mu\Omega$ in cells with high capacity to dozens of $\mathrm{m}\Omega$ in a small cell [5]. Equation (3.1) can be used to find the maximum difference of the battery voltages (ΔV) which keeps the current of the two batteries lower than the maximum allowed values of their cells. Usually, the maximum charging current is lower than the discharging one, so this value is used in the next equation to obtain the ΔV.

$$|\Delta V| = (R_{01} + R_{02}) I_{\max} \tag{3.2}$$

In the equation I_{max} is the absolute of the maximum charging current.

We can note that ΔV represents the maximum voltage difference of the batteries under which they can be parallel-connected but we can decide to use any value less than ΔV in the parallelization algorithm. This choice can be made to reduce the peak current which flows into the batteries when they are parallel-connected.

Moreover, some additional considerations about the simplifications used are useful. The use of a more complex cell model, that includes one or more RC groups, does not change the previous equations. In fact, these equations describe the instantaneous condition of the parallel-connection of the two batteries and so the inertial behaviors of

the capacitors show no observable effect in the equations. For this reason, the groups do not change the peak current but at the same time they reduce the mean value of current which flows from/into the batteries before they reach the same SOC. Therefore, they increase the time needed to achieve the state of equilibrium but reduce the current stress for the cells. On the contrary, the analysis of the effects introduced by the load current is more complex. We can consider two batteries, battery 1 and battery 2, with a SOC difference that does not allow the parallel-connection of the batteries, and for example battery 1 is more charged than battery 2. Moreover, the load current (I_{load}) will be considered constant to simplify the following discussion. In this case, the system can connect the load only to battery 1 which will be discharged and so its voltage will decrease. In this way, the voltage difference of the batteries decreases and it can become lower than ΔV. If this happens, the system can connect the batteries in parallel and both of them to the load. Using the simplified cell model, we can write the equation that describes the system at the moment of the battery parallelization, as follows:

$$\begin{aligned} V_1 - V_2 &= |\Delta V| \\ OCV_1 - R_{01} I_{\text{load}} - OCV_2 &= (R_{01} + R_{02}) I_{\max} \\ OCV_1 - R_{01}(I_{\text{load}} + I_{\max}) &= OCV_2 + R_{02} I_{\max} \end{aligned} \tag{3.3}$$

Starting from this condition, the current which flows from battery 1 to battery 2 decreases until it reaches 0 when the following identity is satisfied:

$$OCV_2 = OCV_1 - R_{01}(I_{\text{load}}) \tag{3.4}$$

After that, the current of battery 2 changes sign and thus this battery, that was being charged by battery 1, starts the discharging phase. The discharge current increases until it reaches $I_{\text{load}}/2$ when the SOCs of the two batteries are the same and assuming that the two batteries have the same ohmic resistance. So from this moment forward, the batteries are discharged with the same current value which maintains the SOCs balanced until the end of the discharge phase.

On the contrary, if the load current reaches 0 after the batteries parallelization but before the moment in which the current of battery 2 changes sign, the value of charging current of battery 2 increases. In fact, we can use equation 3.3 to describe the system in the moment immediately before the drop of the load current, as:

$$\begin{aligned} OCV_1 - R_{01}(I_{\text{load}} + I^-_{\text{recirculation}}) &= OCV_2 + R_{02} I^-_{\text{recirculation}} \\ OCV_1 - OCV_2 &= R_{01}(I_{\text{load}} + I^-_{\text{recirculation}}) + R_{02} I^-_{\text{recirculation}} \end{aligned} \tag{3.5}$$

where $I^-_{\text{recirculation}}$ is the current which flows from battery 1 to battery 2 at that moment. In the moment immediately after the drop of the load current, we can write the following equations:

$$\begin{aligned} OCV_1 - R_{01} I^+_{\text{recirculation}} &= OCV_2 + R_{02} I^+_{\text{recirculation}} \\ OCV_1 - OCV_2 &= I^+_{\text{recirculation}}(R_{02} + R_{01}) \end{aligned} \tag{3.6}$$

where $I^+_{\text{recirculation}}$ is the recirculation current at that moment. Moreover, the OCVs of the batteries cannot change immediately, so we can calculate the $I^+_{\text{recirculation}}$ as:

$$R_{01}(I_{\text{load}} + I^{-}_{\text{recirculation}}) + R_{02}I^{-}_{\text{recirculation}} = I^{+}_{\text{recirculation}}(R_{02} + R_{01})$$
$$I^{+}_{\text{recirculation}} = \frac{R_{01}}{(R_{02} + R_{01})} I_{\text{load}} + I^{-}_{\text{recirculation}} \tag{3.7}$$

We can note that the recirculation current after the drop of the load one can be very high and if it is higher than $I_{\max}$, the batteries must be disconnected to prevent unsafe situations.

These theoretical observations can be summarized in a parallelization algorithm that is described as the finite state machine (FSM) shown in Figure 3.1. The FSM inputs are the voltages V_1 and V_2, the currents I_1 and I_2, and the status flags SF_1 and SF_2 of the batteries 1 and 2, respectively. The status flag of each battery is a Boolean signal that is set to 1 if the battery is in the safe operating area of current, voltage, and temperature, otherwise is equal to 0.

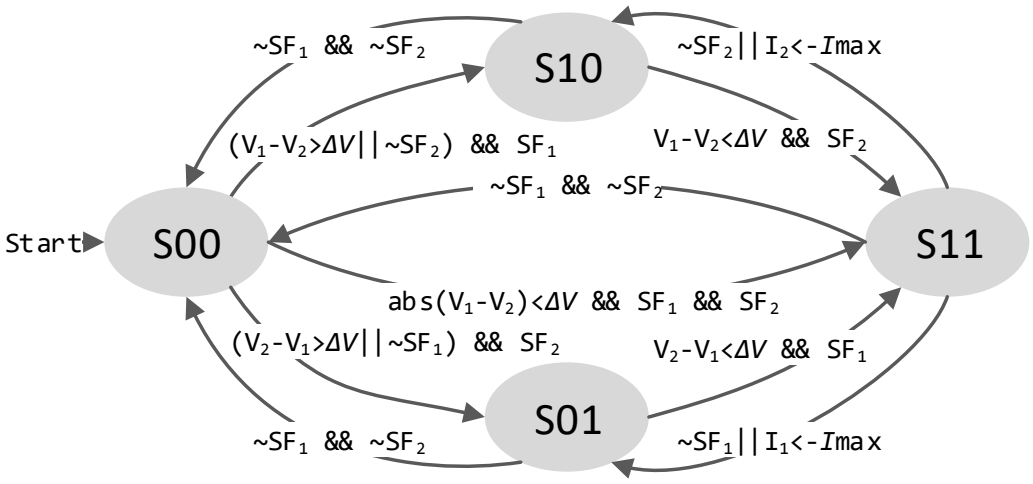

Figure 3.1: *Flow diagram of the finite state machine implementing the parallelization algorithm. V, I and SF are respectively the battery voltage, current (positive during discharge) and safety flag ,and $I_{\max}$ is the absolute of the maximum charging current. The symbols !, && and || mean the logic not, and, or operations, respectively.*

The FSM flow diagram consist of 4 states ($\mathrm{S00}$, $\mathrm{S10}$, $\mathrm{S01}$ and $\mathrm{S11}$). $\mathrm{S00}$ represents the condition in which both battery switches are off, $\mathrm{S11}$ where the two batteries are connected in parallel, whereas $\mathrm{S10}$ and $\mathrm{S01}$ are the states in which only battery 1 or 2 powers the load, respectively.

The FSM starts from the state $\mathrm{S00}$. If the battery voltage difference is less than ΔV and both the battery safety flags are set, then the FSM goes into the state $\mathrm{S11}$. In this state the two batteries are parallel-connected and discharged together. They reach the fully discharge condition at the same time, if they are identical. In this condition, the SF of both batteries is reset, and the FSM returns to the state $\mathrm{S00}$. On the contrary, if for any reason one battery, battery 1 for instance, discharges faster than the other, the FSM goes to the state $\mathrm{S01}$.

This state is also reached from $\mathrm{S00}$ when the SF of battery 1 is reset and the one of battery 2 is set or both the SFs are set but the SOC of battery 2 is greater than that of battery 1, and their voltage difference is higher than ΔV. In this state, only the battery 2 supplies the load, so it is discharged and the battery voltage difference decreases. As

soon as it becomes less than ΔV, the batteries can be parallel-connected, if the two SFs are set, and the FSM goes to $\mathrm{S11}$. It may happen that the parallelization condition ($|\mathrm{V}_1 - \mathrm{V}_2| < \Delta V$) is reached on a peak value of the load current and does not hold when the load current decreases. This causes a battery 1 charging current higher than I_{max}. If this happens, the FSM recognizes it and goes back to the $\mathrm{S10}$ state. As we can note in Figure 3.1, the FSM exhibits a symmetric behavior with respect to the battery position; in fact, the state $\mathrm{S10}$ is equivalent to $\mathrm{S01}$ if we exchange the battery position.

The described parallelization algorithm can be easily generalized for a larger number of batteries. In fact, we can connect the most charged battery to the load bus power first, and the other batteries can be parallel-connected to the first one as soon as their SF and voltage are compatible with the safe connection.

3.1.2 Simulation platform

The aim of the simulation platform is to predict the behavior of a battery system composed of two batteries when they are parallel-connected and power the load. This is very interesting to understand the effect of the parallelization on the batteries and to analyze the parallelization algorithm in order to find any bugs.

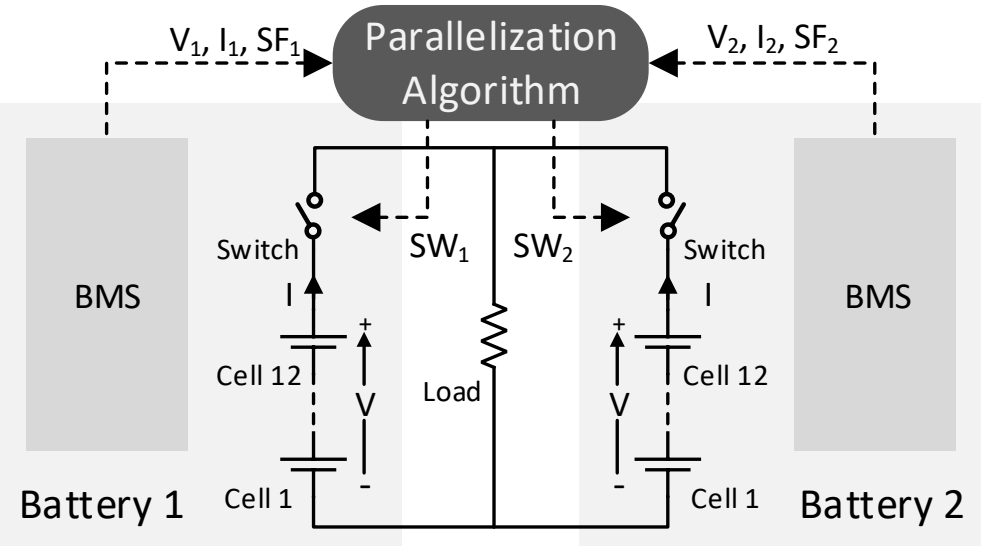

Figure 3.2: *Block diagram of the simulated battery system.*

The platform is developed in a MATLAB®/Simulink® environment and its top level is shown in Figure 3.2. The battery model is composed of 12 series-connected cell model instances and a power switch model and a very simple BMS model. The battery system is composed of two battery models connected with the load, which is modeled as a Simscape™ controlled current source block, whose instantaneous value is the desired power divided by the simulated voltage of the battery. In this way, the load model discharges the battery system with a desired power profile. Instead, the FSM of the parallelization algorithm is implemented using the Stateflow® environment which allows us to graphically design and debug the FSM. The FSM receives as input the safety flag SF_n, the voltage V_n and the current I_n $(n = 1, 2)$ from the two batteries and generates the signals SW_1 and SW_2, which control the two switches, one in each battery.

The cell model is based on the 1-RC equivalent circuit model shown in details in Section 2.1.1 and developed using the Simscape™ blocks. The equivalent circuit model uses the information of the cell capacity, the open circuit voltage, and the parameter R_0, R_1 and C_1, to predict the cell voltage starting from the cell current. The R_0 models the ohmic resistance of the cell, and the R_1 and C_1 group takes into account the fast dynamics due to the charge transfer and the double layer effects [51]. These parameters vary with the operating conditions, which are represented by the cell SOC, temperature, and current. Therefore, this dependency can be modeled by a multi-dimensional LookUp Table, but this requires an extensive test campaign to be carried out on the cell to obtain the LUT values. In this work, only the SOC dependency is considered. OCV can be assumed only as a function of SOC and it is a characteristic of the specific lithium-ion used technology. The relationship between OCV and SOC is stored in a LUT in order to be modeled by a dependent voltage source controlled by the SOC. The impact of the chosen model is analyzed in the next subsection, in which the behavior of the simulated batteries is compared with the real one.

The implemented BMS model simulates the monitoring and protection functions. In particular, it checks if all the predicted cell voltages and the battery current lie within the safe operating area. If this happens, it asserts the safety flag and enables the battery switch to be turned on. In addition to the safety flag, the model computes the overall battery voltage V from the cell voltages.

3.1.3 Simulation results

A battery gardening tool family has been chosen as case-study to configure the simulation platform. In this way, the algorithm results are as realistic as possible. The chosen gardening tool family is the same explained in detail in Chapter 6, and it is originally powered by one lithium-ion battery composed of 12 series-connected cell groups. Each group is obtained connecting in parallel two LGDBHE21865 cells manufactured by LG Chem, which are characterized by a nominal voltage of $3.6\,\mathrm{V}$, a nominal capacity of $2.5\,\mathrm{A\,h}$, and a cylindrical case 18650. Therefore, the battery has a nominal voltage of $43.2\,\mathrm{V}$, a nominal capacity of $5\,\mathrm{A\,h}$, and $8\,\mathrm{A}/40\,\mathrm{A}$ as maximum current of charge and discharge, respectively. The tool used in this case is a lawnmower which is very suitable to be used with two or more batteries dynamically parallel-connected. In fact, its physical characteristics allow us to accommodate the batteries without impairing the usability of the tool while increasing its runtime. However, this choice does not have any impact on the algorithm results.

The tool battery has been instrumented to acquire the cell voltages, the battery current and some points of temperature inside the cell pack. This battery has been used to power the lawnmower in some grass-cutting tests and the collected data have been used as input of the simulation platform. Another new battery has been disassembled to characterize the 12 cell groups using the conventional pulse current test [45] in a thermal chamber at the temperature of $25\,^{\circ}\mathrm{C}$ in order to extract the mean values of the parameter of the model. The extracted values of OCV, R_0, R_1 and C_1, as a function of SOC, are shown in Figure 3.3. The variability of the parameters among the cells are neglected in this work, which is focused on assessing the performance of the battery parallelization algorithm with respect to different SOC initialization mismatches. However, the simulation platform is capable to investigate the battery behavior even when

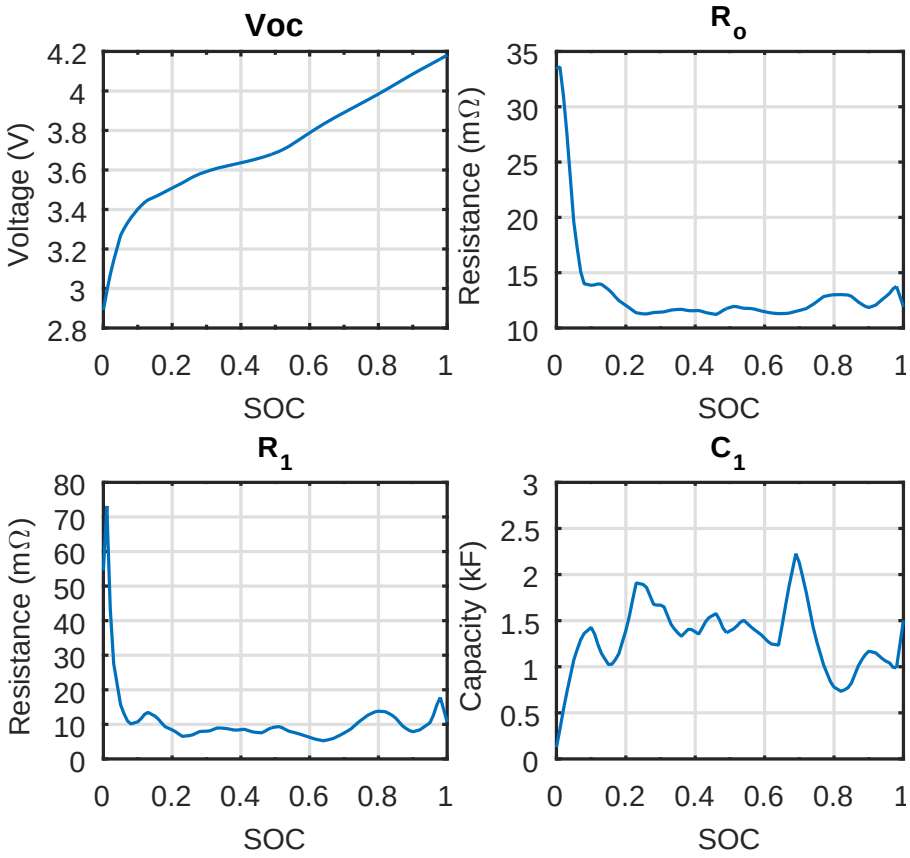

Figure 3.3: *Dependence of the cell parameters on SOC.*

the cells are not fully matched.

The extracted parameters and the battery voltage and current profiles acquired in the grass-cutting test have been used to verify the emulation of the batteries in the simulation platform. In fact, a single battery model has been initialized with the extracted parameters and discharged with the current profile starting from a fully charged condition. The simulated battery voltage and the measured one are shown in Figure 3.4. In particular, we can calculate the relative error as the difference between the measured battery voltage and the simulated one, divided by the first voltage. This error is in the range from $-2.97\,\%$ to $1.81\,\%$ and presents a rms value of $0.45\,\%$. The obtained errors are completely compatible with the application and consequently a more complex model is not needed.

Once the battery model is verified, the platform can be configured to test the parallelization algorithm. Starting from the battery information, we can calculate ΔV using Eq.(3.2) with I_{max} of $8\,\mathrm{A}$ and $\mathrm{R}_{01} = \mathrm{R}_{02} = 156\,\mathrm{m}\Omega$. This last value is obtained multiplying the mean value of the cell resistance R_0 (Figure 3.3) by the number of the battery cells. The obtained ΔV is about $2.5\,\mathrm{V}$.

The acquired power profile in the grass-cutting test has been used to generate the load power profile which discharges the simulated batteries. In particular, the test has been carried out with the lawnmower powered by a single battery, therefore the obtained profile is not able to discharge two fully charged batteries connected in parallel.

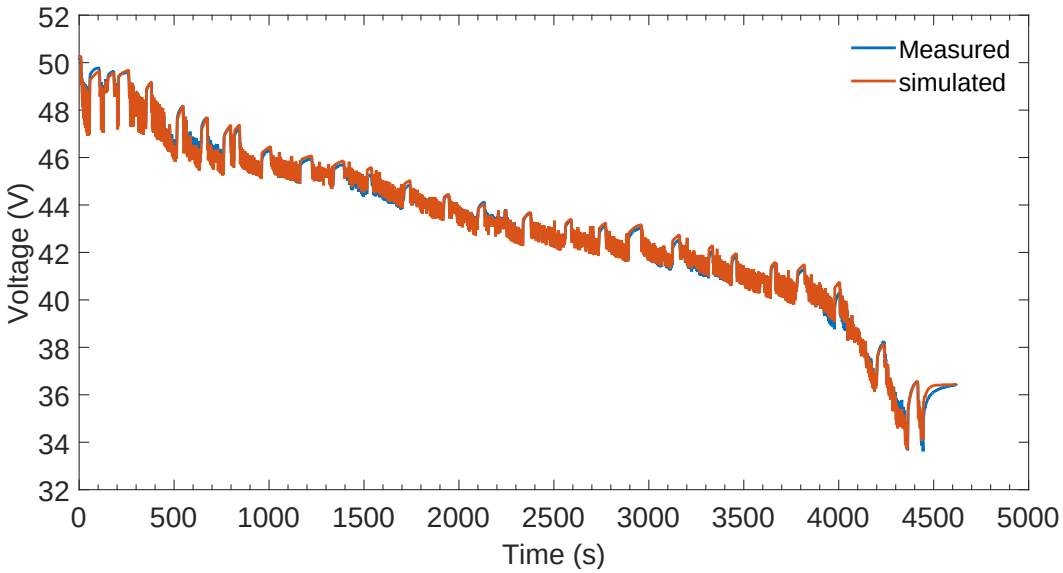

Figure 3.4: *Comparison between the battery voltage obtained by the model and the measured one.*

Furthermore, the power profile depends on the grass thickness that naturally changes in the test. Therefore, the mean and peak values of the power change during the test. To make the power profile more uniform and comparable to the results, $8\,\mathrm{min}$ of the test profile have been selected and repeated to obtain a very good profile which is invariant in respect to the mean and peak values during the time. The mean value of the selected part is equal to $327\,\mathrm{W}$ and presents a peak value of $753\,\mathrm{W}$. Battery 1 initial SOC is set to $100\,\%$ in all the tests, and the initial SOC of battery 2 has been varied within the range from $0\,\%$ to $100\,\%$. With the SOC equal to $0\,\%$ the system is equivalent to the case in which it is powered by only one battery. On the contrary, if battery 2 is initialized with a SOC equal to $100\,\%$ the system is powered by two fully charged batteries, so they are parallel-connected for all the testing time.

An example of the intermediate cases is shown in Figure 3.5, where the battery 2 SOC is initialized to $40\,\%$ and only battery 1 is initially connected to the load because it is more charged than the second one. Therefore, the FSM goes from $\mathrm{S00}$ to $\mathrm{S10}$ and remains in this state until the voltage of battery 1 becomes less than $\mathrm{V}^2 + \Delta V$. When this occurs, the batteries are parallel-connected, because the FSM reaches the state $\mathrm{S11}$.

During the minutes following this event, the load current is not evenly shared between the two batteries, inasmuch the battery 1 SOC is still higher than that of battery 2. Therefore, battery 2 provides the power to the load in some instants and is recharged by battery 1 when the load power decreases. Since the recharging current is always less than the I_{max}, the FSM remains in $\mathrm{S11}$, otherwise the FSM would have moved back to the $\mathrm{S10}$ state, to avoid damages of the battery 2 cells. This process tends to self-balance the SOC of the two batteries in some minutes, as we can see in Figure 3.5, where only the first $32\,\mathrm{min}$ of the simulation are shown to appreciate the algorithm behavior.

The simulations with the battery 2 SOC of $100\,\%$, $70\,\%$, $40\,\%$, and $0\,\%$ are compared in Figure 3.6, in which we have reported the probability density function (pdf) of the current value which flows in battery 1 in the four compared simulations. We can note the most important benefit of the parallelization, which is the decreasing of the battery

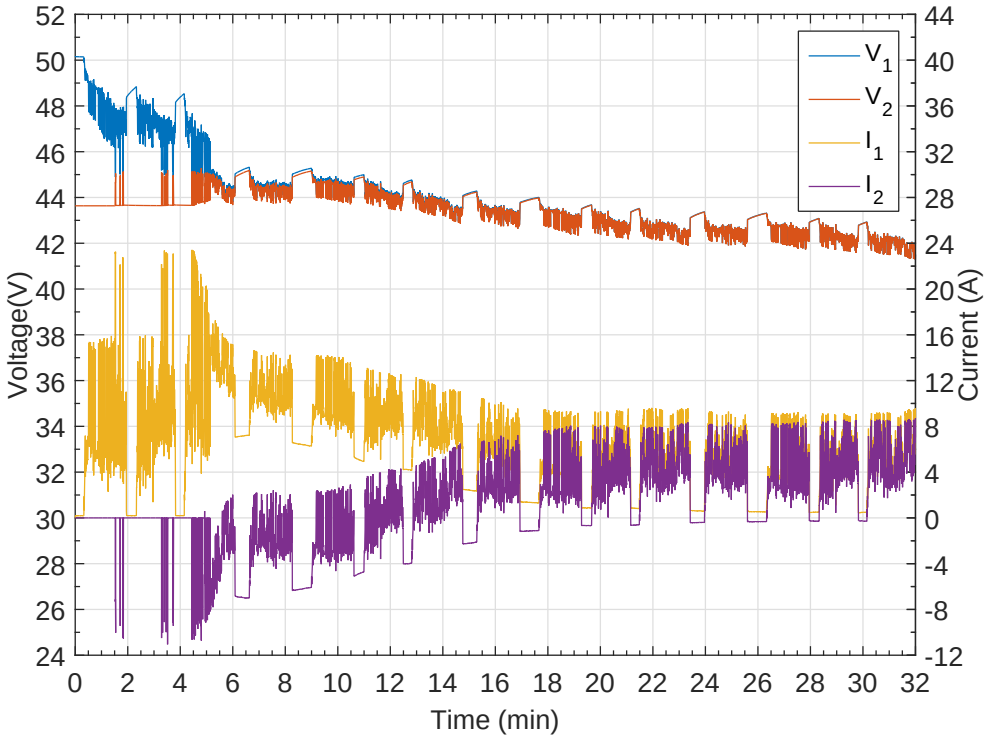

Figure 3.5: *Voltage and the current of the two batteries in the first 32 min of the simulation, where, battery 1 is initialized at* $100\,\%$ *of SOC and the second one at* $40\,\%$.

current rate. In fact, the mean current rate of the case with the battery 2 SOC of $0\,\%$, which is equivalent to the system powered only by battery 1, is of about $8\,\mathrm{A}$, which corresponds to $1.6\,\mathrm{C}$. This value is more than twice if compared to the one which flows in battery 1 when both batteries are fully charged and the parallelization is exploited to the full.

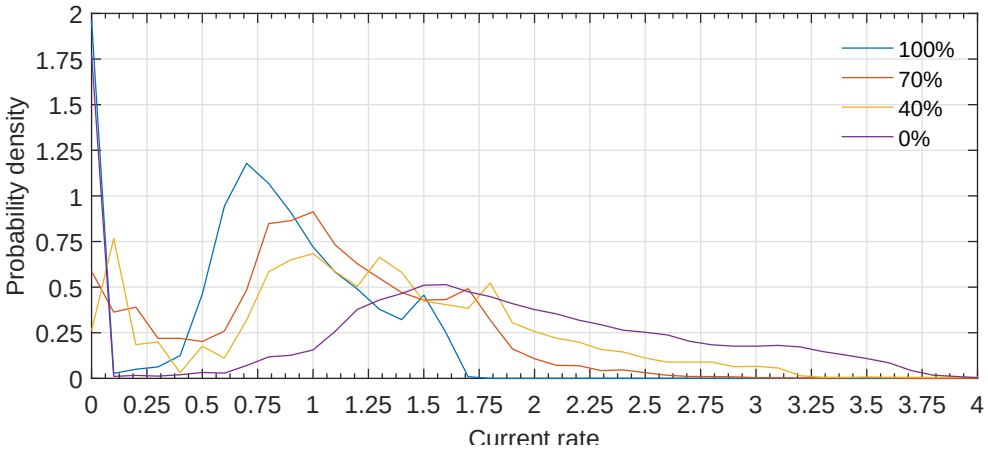

Figure 3.6: *Probability density function of the current rate which flows in the first battery on four simulations. In the all simulations, battery 1 is initialized at* $100\,\%$ *of SOC, instead, the second one is initialized respectively at* $100\,\%$, $70\,\%$, $40\,\%$ *and* $0\,\%$.

The reduction of the battery current rate gives two important benefits: the reduction

Table 3.1: *Performance comparison of different parallelization cases*

Battery 2	Available energy	Energy delivered	Runtime
0 % SOC	210 W h	204 W h	37 min
40 % SOC	285 W h	282 W h	51 min
70 % SOC	350 W h	350 W h	64 min
100 % SOC	421 W h	421 W h	77 min

of battery stress that increases its lifetime and the increment of the tool runtime. To compare the runtime and the delivered energy of the four cases, they are reported in Table 3.1, where also the available energy values of the battery system are shown. These last quantities are estimated multiplying the available energy of a fully charged battery, discharged with a current rate of 1 C, by 1, 1.4, 1.7 and 2 for the cases of initial battery 2 SOC of 0 %, 40 %, 70 % and 100 %, respectively.

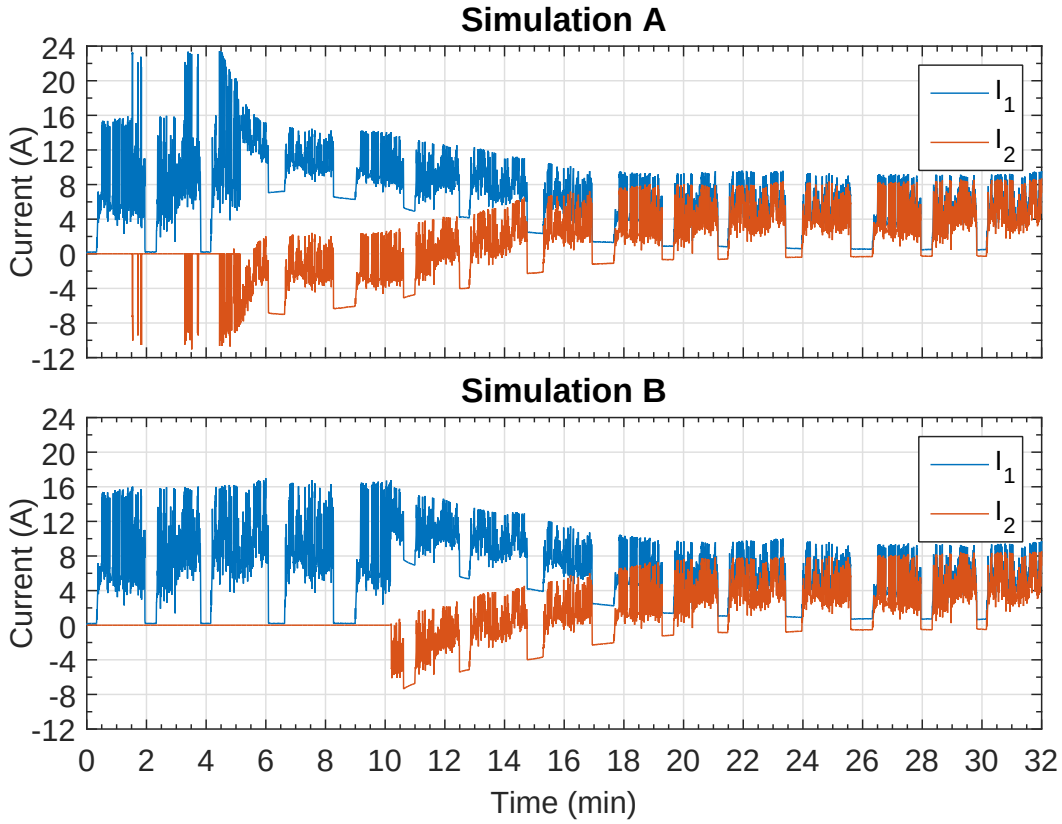

Figure 3.7: *Current of battery 1 and 2 in two simulations in which battery 1 is initialized with a SOC of* 100 %*, battery 2 SOC is* 40 % *and a lawnmower power profile has been used as load. In simulation A,* ΔV *has been set to the maximum allowed value of* 2.5 V *instead the* ΔV *value is equal to* 0.2 V *in simulation B.*

Another interesting use of the platform is the analysis of the influence of the algorithm parameters on the battery parallelization benefits. For example, we can analyze the effect of ΔV on the recirculation current which flows into the batteries. Figure 3.7 shows the current that flows into the batteries in two different simulations in which battery 1 is initialized with a SOC of 100 %, the SOC of battery 2 is 40 % and the power

load profile is the same of the previous tests. In the first simulation, we have configured the ΔV at the maximum allowed value of $2.5\,\mathrm{V}$, instead, in the second one, we have used a ΔV value much smaller than the first one and equal to $0.2\,\mathrm{V}$. We can note that in the second case the parallelization process starts later than in the first one but the peak current values are smaller when the batteries are parallel-connected. Moreover, smaller values of ΔV reduce the number of transitions between the states $\mathrm{S10}$ and $\mathrm{S11}$ making the algorithm more robust and the system more stable.

These simulative results can also be verified with the batteries and the lawnmower designed and reported in Chapter 6, where we have shown the parallelization of two real batteries, obtaining test results comparable with the latter.

3.2 Communication-based Hardware in the Loop framework for algorithm assessment

During the development of complex algorithms, such as some very accurate state estimation techniques, the use of a communication-based HiL platform can be very useful. In [62], we developed a platform to test real BMS functions for electric transportation under many different driving and operating conditions. In particular, we used this platform to verify the implementation and the performance of two SOC estimators implemented in the hardware on an Field-Programmable Gate Array (FPGA): the dual extended Kalman filter (DEKF) and the adaptive mix algorithm (AMA). Both algorithms have been described in details in Section 2.2.2. This platform is provided with a MATLAB®/Simulink® model of an electric vehicle with its battery and the entire acquisition system of the BMS. The battery can be emulated by using different driving cycles under different conditions of unbalancing among the cells, parameter variations and temperature. The platform sends the emulated acquired quantities from the current and voltage sensors to the FPGA JTAG interface. The hardware estimators use these information to compute the state estimation and then it sends the results to the PC in order for them to be stored and compared with the reference values generated from the model. A general block diagram is reported in Figure 3.8.

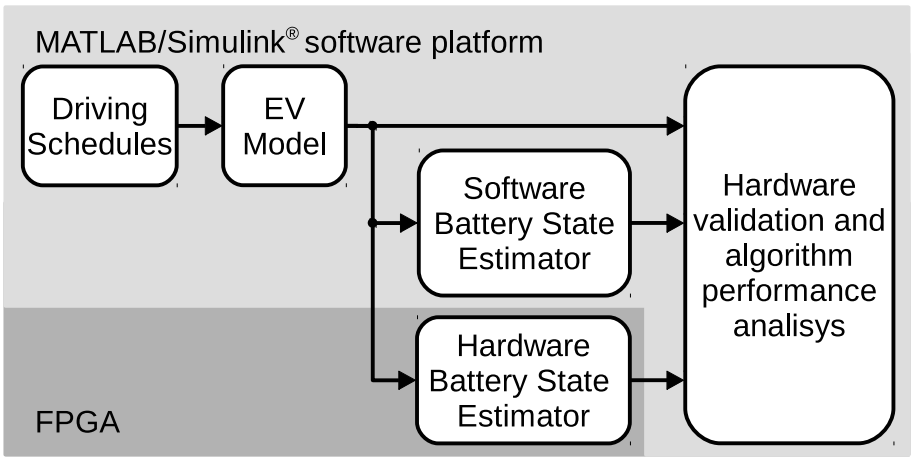

Figure 3.8: *Block diagram of the developed hardware-in-the-loop framework.*

The electric vehicle (EV) model block is the main part of the model. It uses as input

the speed profile provided by the driving schedule block, which allows us to select the driving scenario among 18 different cases. This block provides as output the emulated battery quantities to be sent to the main unit of the BMS under test. Figure 3.9 shows a block diagram of the EV model block.

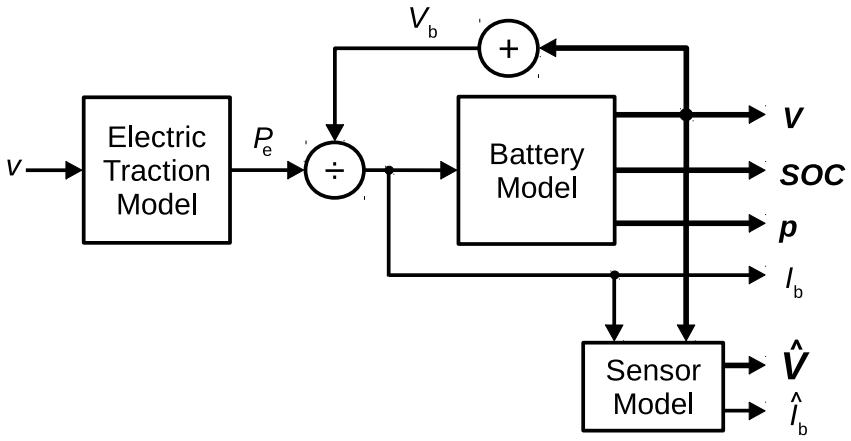

Figure 3.9: *Block diagram of the EV Model.*

The vehicle model consists of three blocks. The electric traction model simulates an EV traveling on a flat road by using a simple dynamic model, as in [14]. The mechanical power is calculated starting from the speed v, as the sum of three contributions: one linked to the acceleration, one to the air resistance and the other to the rolling resistance:

$$P_{\mathrm{m}} = \left(M\dot{v} + \frac{1}{2}\rho_{\mathrm{air}} S C_{\mathrm{X}} v^2 + \alpha_{\mathrm{R}} M g \right) v \tag{3.8}$$

Therefore, the electric power is obtained by using the following equation:

$$P_{\mathrm{e}} = \left(\frac{1}{\eta_{\mathrm{wheel}}} \frac{1 + sgn(P_{\mathrm{m}})}{2} + \eta_{\mathrm{reg}} \frac{1 - sgn(P_{\mathrm{m}})}{2} \right) P_{\mathrm{m}} \tag{3.9}$$

in which, two different energy efficiencies are taken into consideration, one for the traction (η_{wheel}) and the other one during the regenerative braking (η_{reg}). The model can be used to simulate different vehicles, by changing its parameters. In the developed model, we used the model parameters for the Nissan Leaf reported in Table 3.2 together with their description. The output of this model is the electric power P_{e}, which is used to compute the battery current (I_{b}), dividing it by the battery voltage V_{b} (equal to the sum of all the battery cell voltages).

The current is the input of the battery model block that is able to simulate a battery composed of M modules consisting of K series-connected cells, for a total of N=MK cells. As shown in Figure 3.10, the cell model is composed of two parts: the electric circuit model (ECM) and the cell thermal model (CTM).

The first one is based on the model presented in Section 2.1.1 with two RC groups and it is used to generate the cell voltage and SOC value arrays, as well as the value of

Table 3.2: *Model parameters for Nissan Leaf*

Symbol	Description	Value
M	Kerb weight	$1525\,\mathrm{kg}$
S	Frontal area	$2.27\,\mathrm{m}^2$
C_X	Drag coefficient	0.29
α_R	Rolling resistance	0.01
ρ_air	Air density	$1.2\,\mathrm{kg/m}^3$
g	Gravity acceleration	$9.82\,\mathrm{m/s}^2$
η_wheel	Efficiency from battery to wheels	0.7
η_reg	Efficiency from wheels to battery	0.5

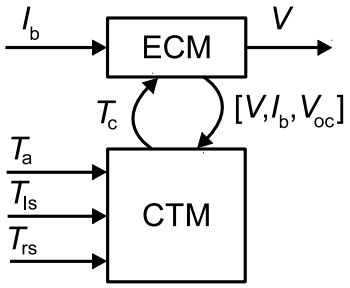

Figure 3.10: *Integration of the electric model with the thermal one.*

the model parameters. The model parameters are stored in 3D Look-Up Tables (LUTs) in order to take into consideration the dependencies on temperature, SOC and current. They have been obtained by performing Pulsed current tests (PCTs) at different temperatures and pulse amplitudes on a $1.5\,\mathrm{A\,hAh}$ NMC cell. The measured parameters are then adjusted to represent a cell from the same technology but with different capacity. At the same time, the temperature of each cell is determined by the CTM. The latter is an electrical equivalent model of the thermal system, as shown in Figure 3.11. The cell core temperature T_c is estimated as the voltage across the thermal capacitance (C_th) by using as input the ambiance temperature Ta and the surface temperature of the two nearest cells in the module (T_ls and T_rs). In fact, the model is able to emulate the cell-to-cell and the cell-to-ambiance heat transfers by using the Θ_cs and Θ_ca thermal resistance, respectively.

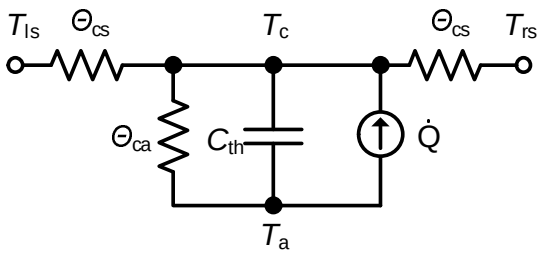

Figure 3.11: *Electrical equivalent thermal model of the battery cells.*

Table 3.3: *Thermal model parameters used in the platform*

Θ_{ca} [K W^{-1}]	Θ_{cs} [K W^{-1}]	C_{th} [J W^{-1}]
67 48	29 61	21 44

The values of the thermal model parameters have been chosen considering the cell chemistry and dimension and then optimizing these values in a MATLAB®/Simulink® environment using the data acquired during a test in a thermal chamber. The final values are reported in Table 3.3.

The current generator $\dot{Q}$ models the cell self-heating. It is the sum of a reversible contribution, the entropic heat flow, and an irreversible part, due to the ohmic losses inside the cell, as shown in the following equation:

$$\dot{Q} = I_b T_c \frac{\partial VOC}{\partial T_c} + I_b(VOC - V) \tag{3.10}$$

A model of the acquisition system has been also developed to consider the measurement errors and noise introduced by an acquisition system, in order to check the algorithm performance in a real system.

3.2.1 Implementation and results

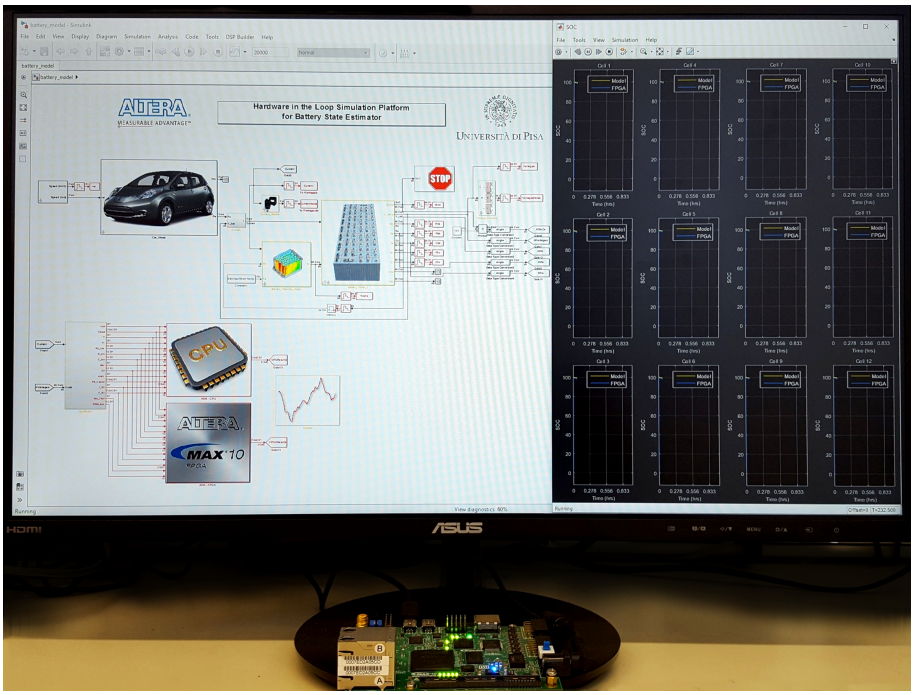

Figure 3.12: *Hardware-in-the-loop platform in action.*

The developed HiL platform is visible in the photograph of Figure 3.12, running on a PC during the execution of a test. The bottom of the figure shows the FPGA-based BMS board on which the estimators have been implemented. The platform has been

used to validate the hardware implementation of the AMA and DEKF estimators and to assess their performance without any power path. The used FPGA belongs to the Intel MAX 10 family. The EV model is used to simulate the Nissan Leaf traction battery, consisting of 96 series-connected NMC cells with a capacity of $66.2\,\mathrm{A\,h}$ and organized in 8 modules of 12 series-connected cells in order to reach the nominal voltage of $355.2\,\mathrm{V}$. The validation of the estimator implementation has been carried out by comparing the FPGA results and those obtained from the software-executed algorithms. Once the implementation is validated, various scenarios have been simulated in order to assess the algorithm performance. All the executed simulations consist in the repetition of one standard driving cycle that the driving schedule block can provide, until the SOC battery reaches $20\,\%$, starting from $80\,\%$. The rms error in SOC estimation is always below $5.1\,\%$ and $2.9\,\%$ for the AMA and DEKF, respectively. This results indicate that a good estimation is achieved by both estimators in all the driving cycles. As an example, Figure 3.13 shows the simulation results for one of the cells of the battery during the Urban Dynamometer Driving Schedule (UDDS) cycle, representative of urban driving.

The temperature of all the cells has been calculated by the thermal model, starting from a steady state of $10\,^{\circ}\mathrm{C}$, which is the value chosen for the ambient temperature. This ambient temperature value emphasizes the cell parameter variation during the test induced by self-heating. As we can note, the SOC estimation accuracy drops in the SOC range from $50\,\%$ down to $25\,\%$ because the SOC is poorly observable from the cell voltage there, as discussed in previous works [19, 64]. Figure 3.13 also shows the identified ohmic resistance R_0 and the time constant $\tau_1 = R_1 C_1$ of the single RC branch in the ECM estimated by the AMA and Dual EKF algorithms compared to the values used in the HiL battery model. It can be observed that both estimators well identify R0, even in the last part of the discharge when it changes significantly. This is a remarkable achievement, as R_0 significantly affects the model accuracy and is a good figure of merit of battery ageing. The time constant estimation appears to be noisier.

3.3 Power HiL for end-of-line verification

Platforms based on the power HiL approach are usually employed in tests of the BMS in the development and production phases. They are able to verify the BMS hardware and software functions, simulating the environment in which the BMS will be used. The power HiL platform generates both the power and communication input signals, unlike the communication-based platform presented in the previous part.

Usually, the solutions proposed in the literature or commercially available are rather expensive, because they are mostly used in the BMS design phase, when the battery behavior needs to be accurately reproduced, especially for the assessment of the complex algorithms used in the BMS to estimate the internal battery states [20, 30, 48, 84]. There are a lot of applications in which this accuracy is not needed and the cost of the proposed solutions is unacceptable. For example, many medium-power applications are characterized by rather low production volumes, as shown in Chapter 6. For this reason, the investments in the design of the system should be limited and classic solutions for power HiL testing might not be affordable. At the same time, the battery is one of the most important and expensive parts of the medium-power/energy systems. Thus,

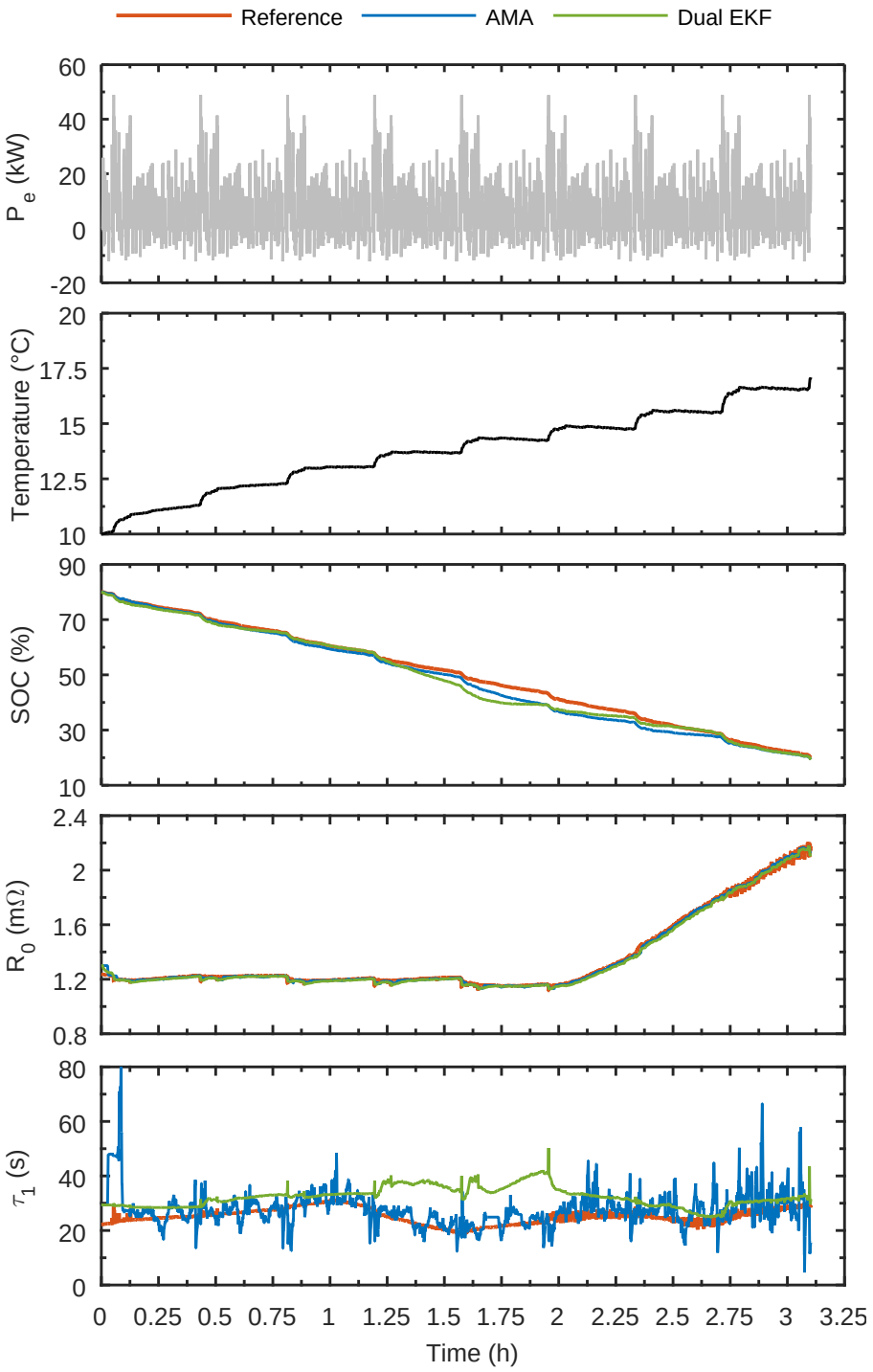

Figure 3.13: *Behavior of SOC and ECM parameters for one of the two central cells of the first module, during a UDDS test.*

a good design and an appropriate test procedure are fundamental to increase the reliability of these systems, to avoid product recalls and to enhance customer satisfaction.

For these reasons, we have developed and presented in the following Sections a low cost solution for the functional testing of a BMS at the end of the production line.

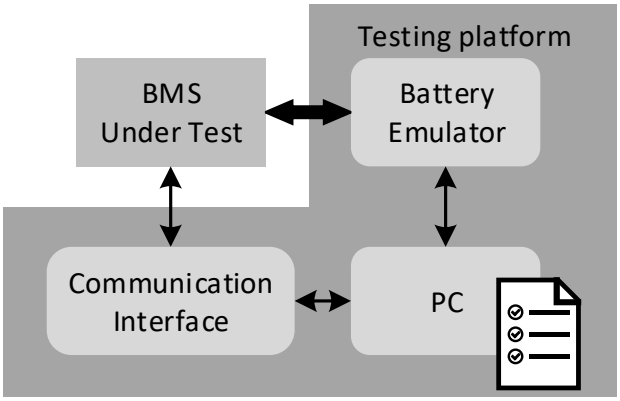

Figure 3.14: *Block diagram of the testing platform.*

3.3.1 Testing platform

The developed testing platform is able to check all the main functionalities of a BMS for medium-power applications shown in Section 6.1 and summarized in Table 3.4, where also the corresponding most probable causes of fault have been reported.

The block diagram of the testing platform is shown Figure 3.14. The battery emulator block reproduces the electrical behavior of the cells, of the load and of the charger, in accordance to the user interface developed in LabVIEW. It allows us to configure the battery emulator and to control the communication with the BMS through the communication interface block. The user interface can independently generate the input signals to stimulate the BMS according to a user defined test procedure and to check the functionalities by analyzing the responses.

The main function of a BMS is the activation of the protection system which can be stimulated with an emulated unsafe situation. The safe operation area is usually defined with respect to the cell voltage, temperature, and current and changes with the used lithium-ion technology [89]. The most common technologies have a cell voltage which varies in a range from $2.5\,\mathrm{V}$ to $4.2\,\mathrm{V}$, thus the platform must be able to vary the cell voltages in a wider range, for example from $2\,\mathrm{V}$ to $4.5\,\mathrm{V}$. For the same reason, the platform must be able to emulate the cell temperatures in a range larger than $-10\,^{\circ}\mathrm{C}$ to $60\,^{\circ}\mathrm{C}$, which is the typical operation range. Instead, the overcurrent values depend on the cell capacity (up to $15\,\mathrm{A\,h}$ for medium-power applications) and thus it is up to $30\,\mathrm{A}$ and $150\,\mathrm{A}$ in charge and discharge, respectively. The platform is also able to interact with the BMS using the communication interface, with which it can verify this functionality of the BMS. Using the communication skill and the ability to generate the cell voltage, current and temperature, the platform can easily check the functionalities of acquisition of these quantities, which the BMS shares on the communication bus.

3.3.2 Battery emulator

To obtain these specifics and to keep the cost low, a custom battery emulator has been developed. It is based on a modular approach to be adapted to BMSs which manage

Table 3.4: *Functions of the BMS and relative possible fault sources*

Function	Fault sources
Acquisition of the cell voltage	Manufacturing defects in the cells voltage measurement circuit The chip monitor does not work correctly There are issues in the communication between the microcontroller and the stack monitor There are malfunctions in the control algorithm of the stack monitor
Acquisition of the cell temperature	Manufacturing defects in the cells temperature measurement circuit The chip monitor does not work correctly There are issues in the communication between the microcontroller and the stack monitor There are malfunctions in the control algorithm of the stack monitor
Acquisition of the battery current	Manufacturing defects in the current sensor circuit The microcontroller does not acquire correctly the current sensor output signal.
Activation of the balancing circuit	Manufacturing defects in the balancing circuit The microcontroller cannot control correctly the activation of the balancing circuit There are malfunctions in the balancing algorithm
Activation of the protection switch	Manufacturing defects in the protection switch circuit The switch is not able to sustain the battery current The microcontroller cannot control correctly the switch There are malfunctions in the cell protection algorithm
Communication with the charger/load	Manufacturing defects in the communication interface There are issues on the communication bus There are malfunctions in the communication task

a different number of series-connected cells. The block diagram of a 12-cell battery emulator is shown in Figure 3.15.

It is composed of 12 stacked cell modules, an 8 bit microcontroller and two current generators. The microcontroller manages the cell modules in according to a LabVIEW interface with which it communicates through a USB port that implements a virtual serial port. The interface controls also the two current generators, one (I_{cell}) to power the cell modules and the other (I_{bat}) to emulate the charger and load currents. The latter is connected between the positive battery terminal (B+) and the positive power input of the BMS (+). Its current flows into the battery current sensor and the protection switch, so that the relative BMS functionality can be tested. In fact, the current value read by the BMS should be equal to the value set by the generator, if the protection switch is closed. Otherwise, this value drops to 0.

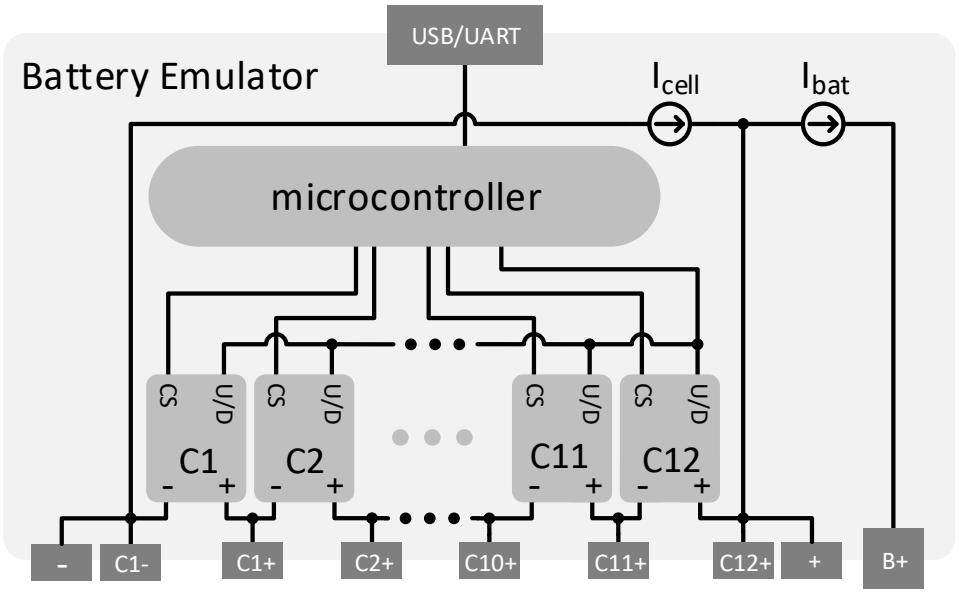

Figure 3.15: *Block diagram of the battery emulator.*

The current generator I_{cell} supplies the cell modules which are based on a bipolar transistor V_{BE} multiplier in which the multiply factor, and thus the cell voltage, is selected by a digital potentiometer controlled by the microcontroller output. The cell module circuit is shown in Figure 3.16 and the cell voltage can be calculated with the following equation:

$$V_{\mathrm{cell}} = \frac{V_{\mathrm{BE}} * (R_{\mathrm{u}} + R_{\mathrm{pot}} + R_{\mathrm{d}})}{R_{\mathrm{d}} + xR_{\mathrm{pot}}} \tag{3.11}$$

where R_{u} and R_{d} are the resistances shown in the figure, R_{pot} is the nominal resistance of the digital potentiometer and x is the fraction of R_{pot} which is connected between R_{d} and the base of the Darlington transistor Q, and V_{BE} is its base-emitter voltage.

The chosen potentiometer is the MCP4011, manufactured by Microchip Technology which is configurable with 64 resistance levels and is controlled with two digital signals: the chip select and the Up/Down. These signals are isolated by a two channel optoisolator, allowing the microcontroller to set the potentiometer using two simple GPIOs, though the cell modules are staked. A key feature of this potentiometer is the requirements in respect to the voltage supply. In fact, it can be supplied with a voltage in a range from $1.8\,\mathrm{V}$ to $5.5\,\mathrm{V}$ which is compatible with the desired cell voltage range. Therefore, it can be powered directly with the cell voltage of the module where it is used. This reduces the cell module cost because it avoids an additional supply source. This feature strongly simplifies the battery emulator architecture and improves the solution used in [31], in which the cell modules are based on a digital to analog converter that needs an isolated DC/DC converter to make them stackable. This solution is more accurate than ours, but it is considerably more complex and expensive, and so that seems less suitable for the considered applications.

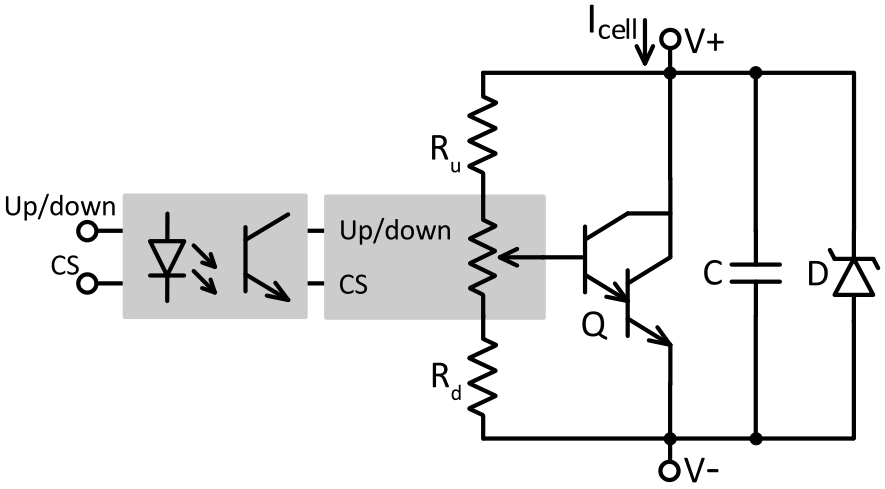

Figure 3.16: *Schematic of the stackable cell module.*

In Figure 3.16, we can note a Zener diode D connected in parallel to the V_{BE} multiplier circuit, which is normally not active and acts as protection. In fact, it limits the cell voltage and protects the BMS monitor input in case of a hardware fault in the cell module. In parallel to the diode D, there is also a capacity C to filter off the high frequency components of the current (I_{cell}).

The BMSs used in the medium-power applications are usually equipped with some negative temperature coefficient (NTC) resistances to measure the cell temperature. This type of transducer is usually measured by reading the output of a voltage divider that includes it. For this reason, the digital to analog converter peripheral of the microcontroller can be used to generate the voltage that, properly adapted, emulates the response of the NTC.

Table 3.5: *Experimental battery emulator components*

Component		Value
Microcontroller		Atmel ATxmega256A3BU
I_{cell} generator		TTI QPX1200SP
I_{bat} generator		TTI QPX1200SP
Cell modules	R_{u}	1.8 kΩ
	R_{pot}	MCP4011
	R_{d}	1.5 kΩ
	Q	BCV49
	D	SMAZ5V1
	C	0.1 µF

3.3.3 Platform implementation

The presented platform has been implemented to perform the functional testing of the BMS designed to manage a battery for gardening applications, which is composed of 12 series-connected cells. The Battery emulator has been realized with a PCB fast prototyping service and shown in Figure 3.17, instead the used components are reported in Table 3.5.

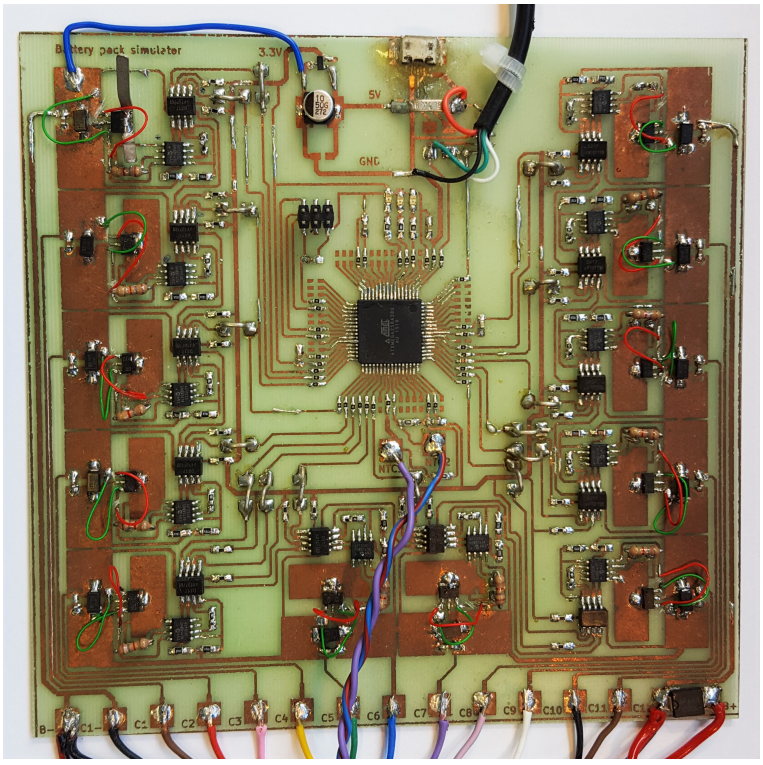

Figure 3.17: *Photo of the realized battery emulator.*

To control the platform and to communicate with the BMS, a user interface has been developed in LabVIEW. Figure 3.18 shows the experimental setup, in which the main components have been highlighted.

First of all, the functionality of the developed cell modules has been verified, com-

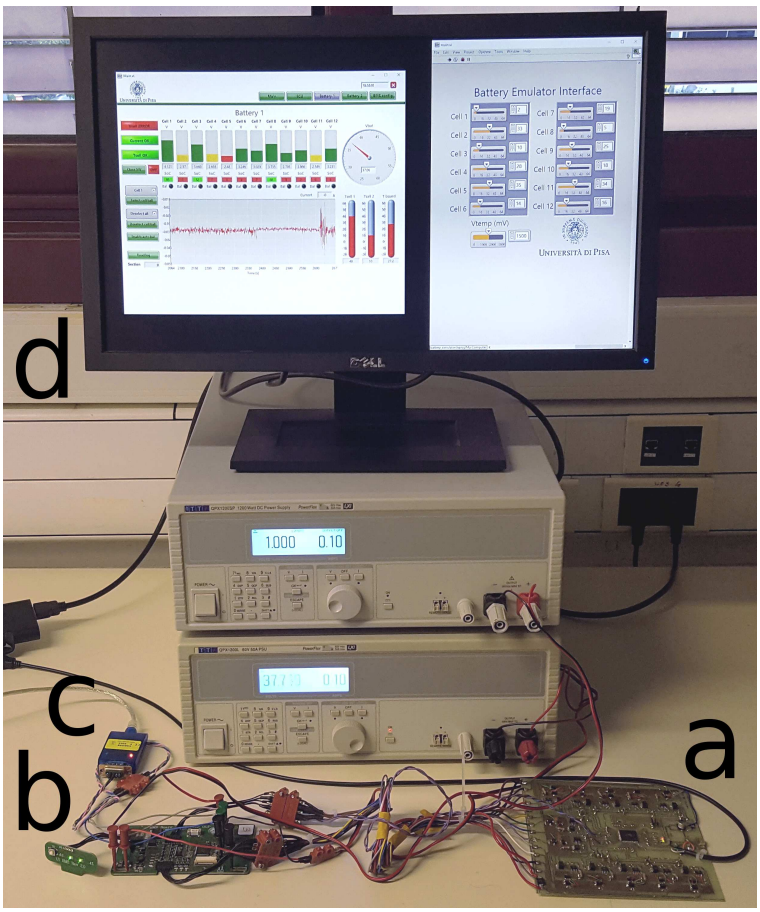

Figure 3.18: *A photo of the experimental setup, where the letter a indicates the battery emulator, b the BMS under test, c the communication interface, and d the control interface.*

paring the measured and the calculated cell voltage, which are functions of the digital potentiometer value, as shown in Figure 3.19. The calculated voltage is obtained by the Eq.(3.11) with the components summarized in Table 3.5 considering the V_{BE} of the Darlington transistor Q of $1.25\,\mathrm{V}$. This value is obtained from the component datasheet with a collector current of $100\,\mathrm{mA}$ and a temperature of $50\,^{\circ}\mathrm{C}$, which are the same current and temperature of the transistor during the acquisition of the cell module voltage when it is about $3\,\mathrm{V}$. We can note that the two voltages are quite similar and their difference increases at the end of the potentiometer values. This is the main issue of the presented circuit and it is due to the variability of the V_{BE} with respect to the variation of the transistor temperature, which depends on the power dissipated on the transistor and thus on the cell voltage.

Therefore, the measured cell voltage is lower than the calculated one for high cell voltage values because the transistor temperature is higher than $50\,^{\circ}\mathrm{C}$ causing its V_{BE} is lower than the one used to compute the expected cell voltages. On the contrary, the transistor temperature is lower than $50\,^{\circ}\mathrm{C}$ when the cell voltages are lower than $3\,\mathrm{V}$ and consequently the transistor V_{BE} is higher than $1.25\,\mathrm{V}$. This implies that the measured cell voltage is higher than the calculated one.

However, the consequent voltage inaccuracy does not impair the effectiveness of

the platform, which is designed to check the functionalities of the BMS and not to characterize the measurement features. Moreover, the cell voltage is in the range from $1.9\,\mathrm{V}$ to $4.5\,\mathrm{V}$, which is large enough to exceed the cell voltage limits that lead the BMS to activate the protection switch.

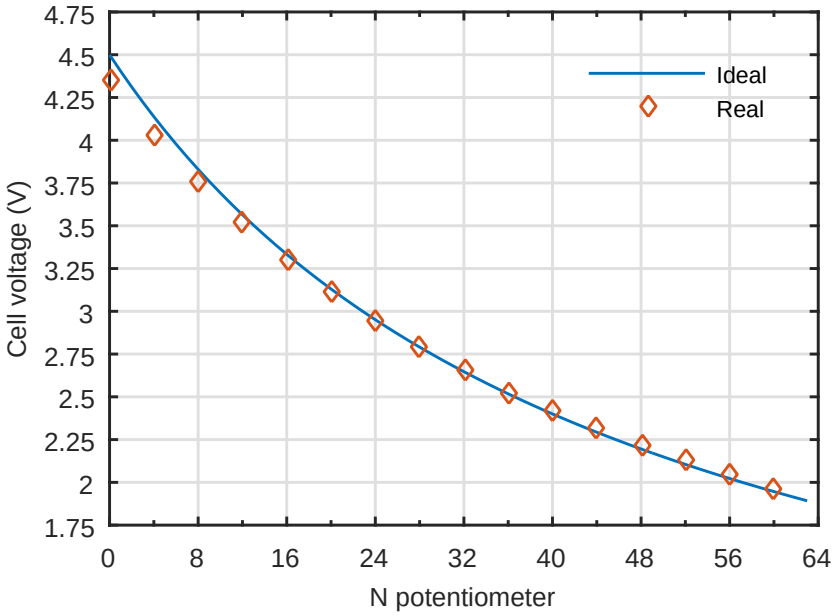

Figure 3.19: *Comparison between the cell voltage obtained by equation (3.11) and the measured one.*

However, this circuit presents a good advantage that allows us to check the balancing functionality of the BMS, because the module is able to source and sink current from/to the BMS. It is linked to the I_{cell} that is limited by the maximum collector current of Q. The chosen Darlington transistor withstands a maximum collector current of $500\,\mathrm{mA}$, so the transistor and the PCB board must be able to dissipate a power up to $2.25\,\mathrm{W}$. Therefore, the cell module can source a current approximately equal to I_{cell} and sink a current equal to the difference between the maximum collector current and I_{cell}.

3.3.4 Validation of a BMS for 12 cells

A BMS for medium-power applications, which manages 12 series-connected cells and is explained in details in Section 6.1, has been used to carry out all the functional tests described in Table 3.4. Figure 3.20 shows the platform interface during the test of the voltage acquisition function. The interface graphically represents the quantities measured by the BMS and shared through the CAN-bus. For example, the cell voltages are represented in the interface with the bars whose level is proportional to the measured value.

Figure 3.20a, it is reported the situation in which the BMS connected to the platform works well with an emulated battery that represents the normal behaviors of the cells. In fact, all the cell voltages read by the BMS show values compatible with those set by the battery emulator. On the contrary, Figure 3.20b shows the case in which the platform, starting from the same condition, tests another BMS with the cell 4 input channel short-circuited. In this case, the interface highlights the fault on this channel

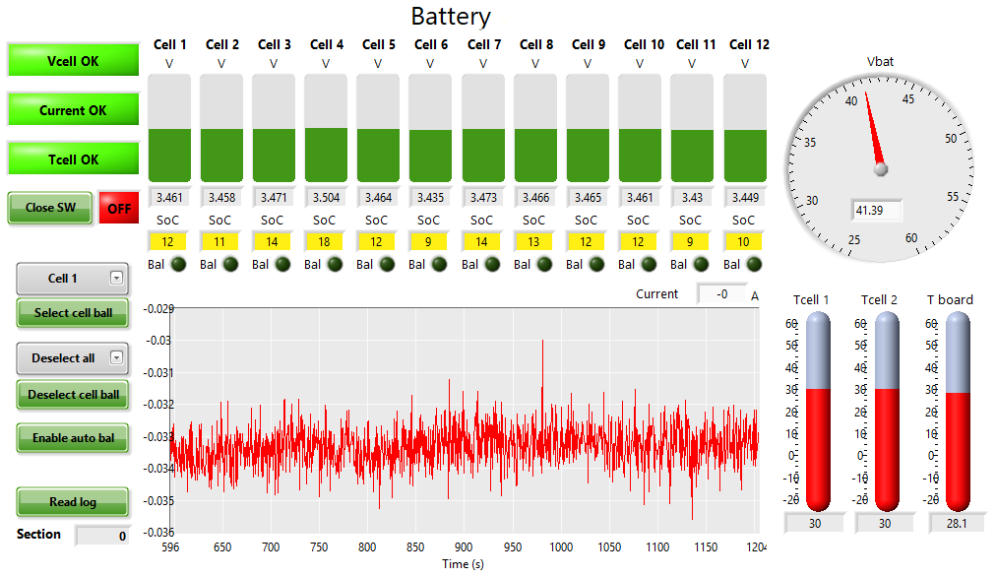

(a)

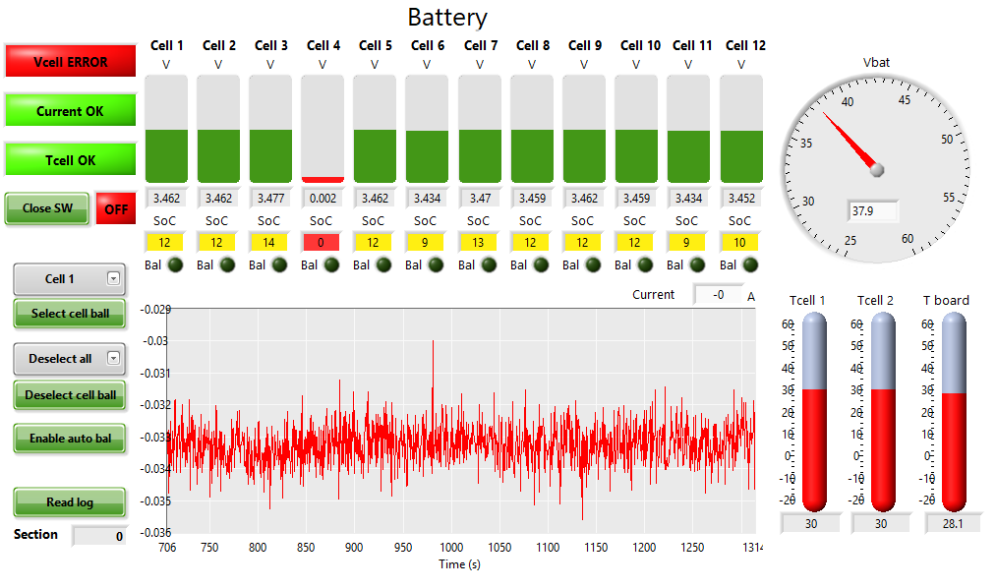

(b)

Figure 3.20: *Comparison of the control interface in the cases of BMS without faults (a) and with the short-circuit on the cell 4 (b).*

with a red indication.

With the measures of the cell voltage, the passive balancing circuit of the BMS can be also tested. When the BMS connects the bleeding resistance (R_{ball}) in parallel to the cell, the biasing current I_{cell}, which flowed earlier in the Darlington transistor Q, is now split between the transistor and R_{ball}. Assuming a BMS balancing resistance of $33\,\Omega$, an I_{cell} equal to $100\,\text{mA}$ and a cell voltage value higher than $R_{\text{ball}} * I_{\text{cell}}$ (e.g., $4.1\,\text{V}$), the cell voltage becomes lower than $3.3\,\text{V}$ when the BMS enables the balancing circuit. This effect is demonstrated in Figure 3.21, where we have reported the voltage drop in

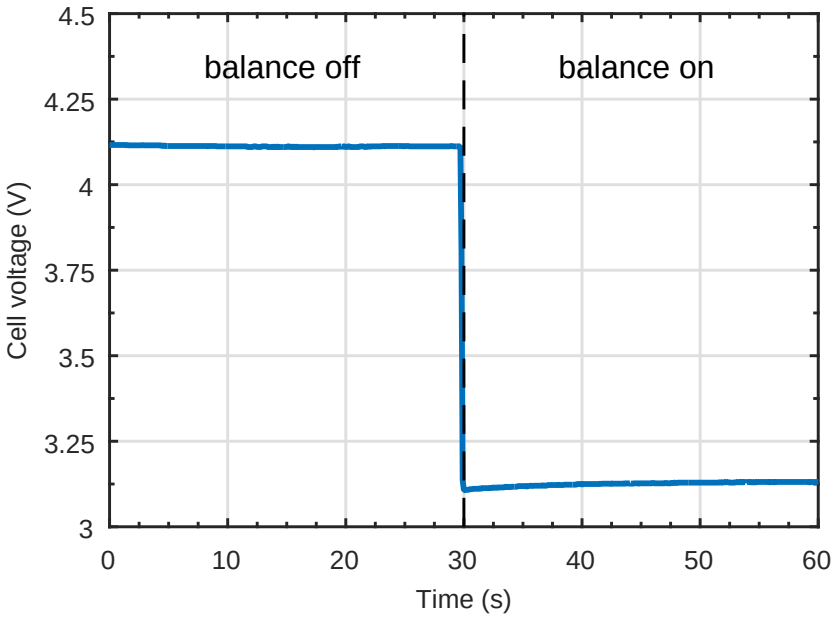

Figure 3.21: *Voltage of the cell module during the activation of the balancing circuit.*

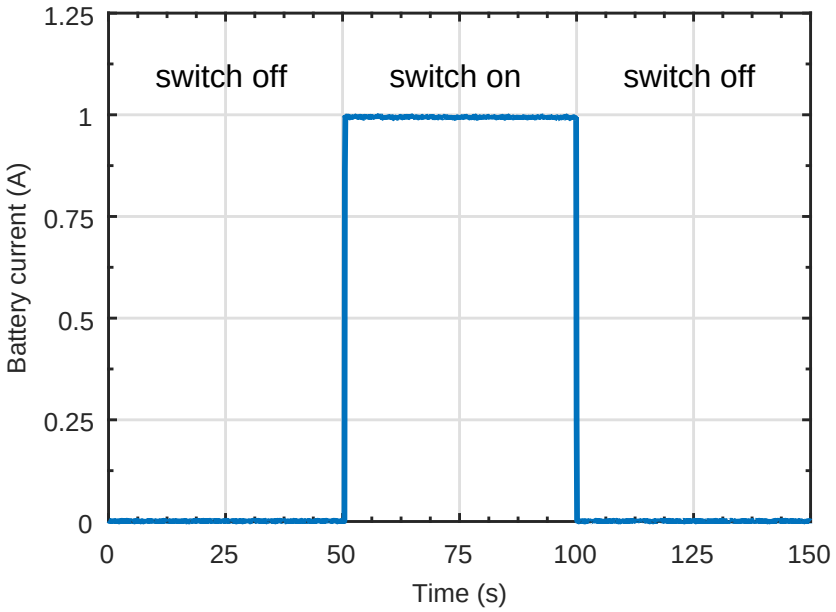

Figure 3.22: *Battery current during the functionality test of the protection switch.*

the cell module after the balancing circuit is enabled.

To test the battery current measurement and the protection switch activity, we have set I_{bat} to $1\ \mathrm{A}$ and the protection switch state is changed by sending a command through the BMS interface. The test results is reported in Figure 3.22, where the measured battery current is shown. We can note that the current is equal to the set one when the switch is closed and otherwise equal to 0.

In conclusion, the presented experimental results demonstrate the ability of the platform to perform the functional testing on a BMS designed to manage a battery for

medium-power application. It can be easily adapted to emulate batteries with different numbers of series-connected cells, because it is based on a modular approach. Finally, its cost is below 50 €, thus demonstrating the goal of designing a low cost battery emulator for functional testing of BMS for medium-power applications.

CHAPTER 4

Battery based on standard module

An important high-power application is represented by the medium/small vehicles. This category contains vehicles for the commercial and industrial activities, such as work machines for moving materials, street cleaning and horticulture, but also vehicles for the e-transportation, such as minibuses, minicars and little vans. In the above sketched scenario, the electrification is very promising [33, 94]. In fact, it can introduce many unquestionable advantages like the reduction of noise, the increase of maneuverability, and a lower impact on local pollution.

For this reason, the history of the small vehicles electrification is very long, and on the market there are a lot of electric solutions based on a lead-acid battery that present many limitations. The most important is the lifetime which imposes the battery replacement after a low number of cycles. This problem can be resolved using the lithium-ion technology which presents a lifetime much higher that the lead-acid one. Furthermore, this chemistry offers a higher energy/power density compared to the weight and volume, which allows us to reduce the battery weight and volume, keeping the energy and the maximum power of the old one. The high charging current is another important feature of the lithium-ion cells, and it can be used to reduce the size of the battery, introducing in the rest times the recharge phases in which the delivered energy, or part of it, can be recovered.

The success of the transformation from the lead-acid battery application to the lithium-ion one, is deeply connected to the availability of a low cost lithium-ion battery which has the same characteristics in terms of battery voltage and capacity of the lead-acid one. The major limiting factor for the electric transformation of these kinds of vehicles is the overall battery cost that can be significant reduced using the standardization approach. Thus, it is important to identify a standard battery module, which can be used to build up the battery for each type of machine by connecting in series or

Table 4.1: *Main characteristics of cell HP-PW-60Ah*

Item	Condition	Specification
Nominal Voltage		3.2 V
Nominal Capacity	C/3 Discharge @ 23 °C	60 A h
Available Capacity	1 C Discharge 2 C Discharge 3 C Discharge	>98 % >95 % >90 %
Specified Volumetric Density	C/3 Discharge @ 23 °C	133.7 W h L^{-1}
Specified Gravimetric Density	C/3 Discharge @ 23 °C	94.1 W h kg^{-1}
Specific Power	@ 23 °C	282 W kg^{-1}
Specific Power	@ 23 °C and 15 s	282 W kg^{-1}
Standard Charge	Constant current Constant voltage	20 A 3.65 V
Fast Charge	Constant current Constant voltage	120 A 3.65 V
Standard Discharge	Constant current End condition	20 A 2.5 V
Maximum Discharge	Constant current for 60 s for 5 s	180 A 250 A 500 A
Operation temperature	Charge Charge	0 °C to 45 °C −20 °C to 60 °C

in parallel the required number of standard modules [91].

4.1 Standard battery module

To define the main characteristics of a standard module, the study of the Italian market presented in [91] can be used, in which the authors have analyzed a list of 64 vehicles. They have considered vehicles with different battery voltage levels (48 V, 96 V, and 192 V) and battery capacities (120 A h and 180 A h) and have individuated the characteristics of a possible standard module. It can be used, taken individually or series/parallel-connected, to satisfy the requirements of the studied vehicles. To maximize the flexibility of this solution, they have proposed three 12 V standard modules with a capacity of 30 A h, 60 A h, and 100 A h, respectively.

The Lithium-Iron-Phosphate (LFP) cells seem to be the best choice to make the standard modules, because this chemistry provides good intrinsic safety and a voltage range that allows us to obtain a voltage of about 12 V by connecting 4 cells in series. These cells must be controlled by an electronic board called BMS, as shown in Section 2.2, on which the modularity approach and a hierarchical architecture can be also adopted to reduce the complexity and increase the flexibility of the system.

Because of this, the standard module is composed of 4 LFP series-connected cells controlled by an electronic board: the Module Management Unit. The modules are properly connected in series/parallel to compose the battery and are controlled by a higher

level control board: the Pack Management Unit. Starting from a commercial analysis of the LFP cells, the HP-PW-60Ah has been chosen, and its main characteristics are summarized Table 4.1.

4.1.1 Module Management Unit

The main aim of the MMU is to optimize the module usage, by monitoring and controlling the modules in according with the directives of the higher hierarchical level. Figure 4.1 shows the block diagram of the MMU.

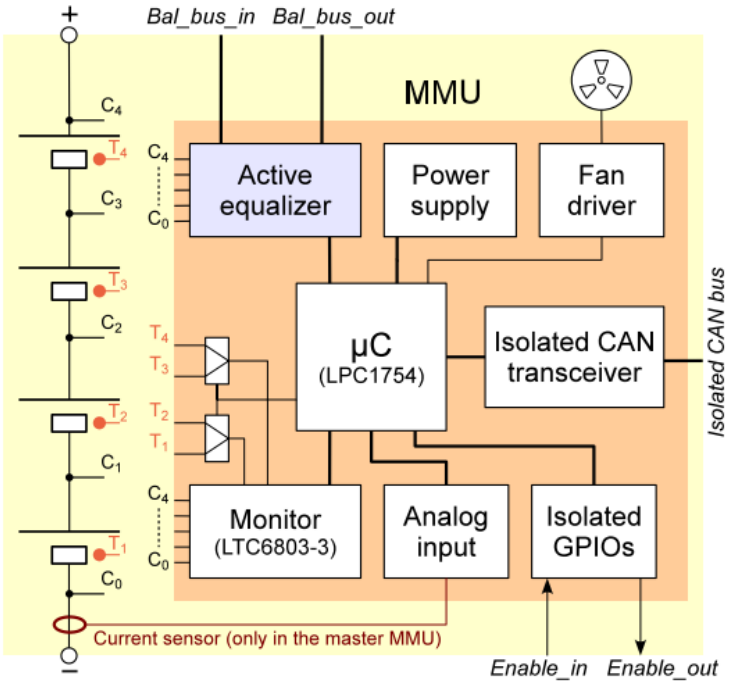

Figure 4.1: *Block diagram of a Module Management Unit.*

The core of the MMU is the LPC1754 microcontroller, manufactured by NXP and based on an ARM Cortex M3 processor with a 32 bit data bus. It acquires the voltage and temperature of the cells through a dedicate chip (the LTC6803-3 from Linear Technology) which is controlled via a Serial Peripheral Interface (SPI). The LTC6803-3 can measure the four cell voltages, with $10\,\mathrm{mV}$ accuracy, and two points of temperature using Negative Temperature Coefficient (NTC) resistors. To measure all the cell temperatures, the board is equipped with two 2-way analog multiplexers, controlled by the microcontroller, which connect the 4 NTC resistors to the two input channels. The NTCs are glued to each cell case in the spot where the highest temperature has been measured by an infrared camera during high current tests.

The MMU can measure the module current through an external Hall Effect transducer, connected to the board using an appropriate analog front-end and two inputs of the Analog to Digital Converter (ADC) peripheral of the microcontroller. Two inputs are needed because the vast majority of current sensors for these kind of applications is provided with two output channels with different measurement ranges in order to

increase the accuracy of the measurement, such as the sensors belonging to the DHAB family from LEM with $1\,\%$ typical accuracy. The current sensor is not incorporated in the board, because, if the module is connected in series with other modules, the same current flows into all of them. In this case, only one module is provided with the current sensor and it will share the measured information with the other ones.

To communicate with the other battery modules and the higher hierarchical level, the MMU is equipped with an isolated CAN-bus transceiver. The module is also provided with three isolated output and one input with which the special priority signals can be routed. For example, the input can be used to wake-up the microcontroller and the board when the key of the vehicle is turned. This is very important because the MMU is powered by the module cells so that its power consumption is critical, as it might dramatically worsen the self-discharge rate of the battery. Thus, the microcontroller can manage the power supply of the other blocks, turning them off when are not needed, and then it can go into a low-power operating mode when the battery is not used.

The Module is also provided with three fans, which the microcontroller can activate through a dedicated driver to cool the cells and the MMU board in the most stressful thermal situations, such as the fast charge phase and the vehicle power peaks.

Finally, the MMU is equipped with an active equalization system based on the solution presented in Section 2.2.3. The DC/DC convert is the Cincon EC6A01, which has been chosen because it can be powered directly by the module voltage and its output can be used as current generator, with a value equal to $1.5\,\mathrm{A}$. The DC/DC converter output is connected to a switch matrix which can connect it to each module cell or to an external balancing bus. The external bus allows us to transfer the energy from this module to each other cell of the other modules connected to the bus. To guarantee that the cells are never short circuited, in the MMU the switch matrix is provided with a Complex Programmable Logic Device (CPLD) programmed to safely manage the matrix regardless of any decision made by the microcontroller, implementing the switch logic driver.

The implemented equalization procedure is explained in detail in Section 5.4, because it is strongly dependent on the application in which the module is used.

4.1.2 Firmware architecture

A Real Time Operating System (RTOS) for embedded architectures has been used on the microcontroller to implement the firmware. This choice allows us to increase the flexibility of the system because each functionality can be developed as a specific thread, which exchanges the needed information with the other ones by sharing blocks of memory. In this way, a specific function can be changed in terms of code, timing or priority without changing the other threads. The chosen RTOS is the FreeRTOS which is completely free and can be used in a commercial device without paying any fees. Moreover, it guarantees a good trade-off among simplicity of use, performance, memory and time overhead.

The main tread executes the protection control algorithm which reads, from a specific memory structure, the cell voltage, temperature and current and controls the module in order to avoid unsafe situations. Moreover, it generates a priority signal, using the isolated output, to alert the high hierarchical level of the BMS. The measures of voltage, temperature and current are managed by three different treads to allow the optimum me-

asurement frequency of each quantity. These measurements and all the other interesting bits of information of the module are sent on the CAN-bus by a dedicated tread, which also manages the received commands.

The firmware is provided with a task which estimates the SOC, starting from the information on the cell capacity, current, and the relation between the OCV and the SOC, and using the coulomb-counting algorithm with OCV correction.

4.2 Standard module arrangement

The number of modules that compose the battery can be calculated starting from the vehicle characteristics and the application constraints. For example, the voltage of the vehicle control system provides the number of modules which must be connected in series, the available volume and the maximum weight reserved for the battery limit the number of usable modules, the maximum application power imposes the minimum number of modules to be connected in parallel, and so on. From this analysis, we can obtain the number of modules which must be connected in series and in parallel to compose the battery, which can be indicated with the letters s and p, respectively. These modules can be considered arranged in a matrix of s rows and p columns which can be connected together using many topologies. The chosen connection approach does not influence the battery characteristics if the modules are exactly identical to each other and are initialized with the same SOC value, but this condition is not realistic. For this reason, the choice of the connection topology is a key aspect of the battery development.

The most intuitive topology consists in dividing the modules in p strings composed of s series-connected modules, and connecting the strings in parallel to obtain the battery. Another possible solution is the opposite and consists in connecting s groups of modules in series, where in each group the modules are parallel-connected.

To the best of my knowledge, the identification of the best parallel/series configuration considering capacity spreading among the cells has not be investigated yet. Moreover, the choice of the best topology is not straightforward, because the recirculation current between parallel connected cells/modules with different characteristics is difficult to predict, as it depends also on the applied current, as it will be shown in Section 3.1. Furthermore, the problem is complicated by the non-linear relationship between SOC and OCV. To the best of my knowledge, this problem has not be faced in the literature yet.

From these reasons, we have proposed a simulation platform, developed in Simulink® environment using Simscape™ blocks, which is able to highlight the difference between the connection topologies [16].

In this work, we have studied the module connection problem for a battery composed of 24 standard modules, with a capacity of $60\ \mathrm{A\,h}$, and divided in a matrix with six rows and four columns. The modules have been emulated using four series-connected instances of the cell based on the 1-RC equivalent circuit, and a simple model of a MMU which controls a safety flag signal. The MMU sets this flag if the four emulated cell voltages and the module current are in a safe operation area (defined in the MMU model). In this work, four different topologies, showed in Figure 4.2, have been compared in terms of complexity, flexibility and performance. The configurations A and D

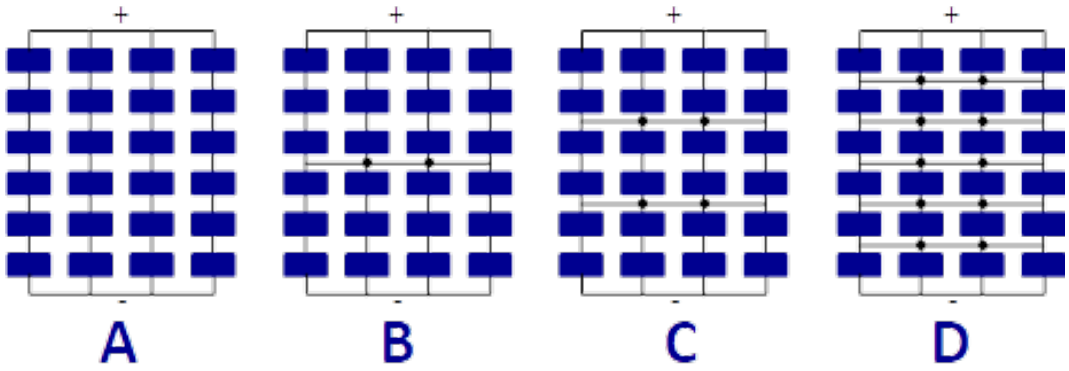

Figure 4.2: *Four possible architecture topologies.*

are based on the two intuitive topologies previously presented, whereas the configurations B and C are hybridizations between A and D. Starting from A, the strings have been divided in two substrings connecting together the middle point of all strings to obtain the configuration B. In topology C, the same procedure of B has been adopted but dividing each string in three substrings.

One of the most important metrics to define the topology performance is the maximum charge quantity which the battery can provide to a load, because it is connected to the application runtime. This quantity can be estimated using the simulation platform in which four batteries, based on the four topologies, are modeled. The characteristics of the modules used in the single battery can change, but all the batteries are composed of the same modules, arranged in the same way, and initialized with the same SOC to a fair comparison.

A statistical study has been carried out to compare the maximum charge quantity provided to a load by the batteries. In this way, the comparison does not depend on the module characteristics. The most significant parameter of the cells, which influences this quantity, is the cell capacity, so it is randomly generated with a Gaussian distribution having as mean value as the nominal capacity of the cells ($60\,\mathrm{A\,h}$) and three different values of the standard deviation: $2.5\,\%$, $5\,\%$ and $10\,\%$. The first value is representative of the capacity differences between the cells of the same pack at the beginning of their life. The other two values consider the aging of the cells, which tends to increase the cell differences [22]. We have performed 200 simulations for each value of the standard deviation, evaluating the behavior of the four previously described architectures for each randomly generated battery. Each simulation starts with a fully charged battery which is discharged with a current of $240\,\mathrm{A}$ (1C-rate) until one or more MMUs reset the safety flag signal. The charge quantity which the battery has provided in this simulation is defined battery capacity.

Figure 4.3 shows the histogram of the battery pack capacity in the condition of $2.5\,\%$, $5\,\%$ and $10\,\%$ as cell mismatch standard deviation. The height of each bin indicates the relative frequency of occurrences, *i.e.*, the number of occurrences of each bin divided by 200.

It is worth noting that in all the cases the configuration D statistically provides a higher capacity than the topology A, as also reported in the literature [41]. Instead, topologies B and C present statistical capacity between A and D, being hybridizations

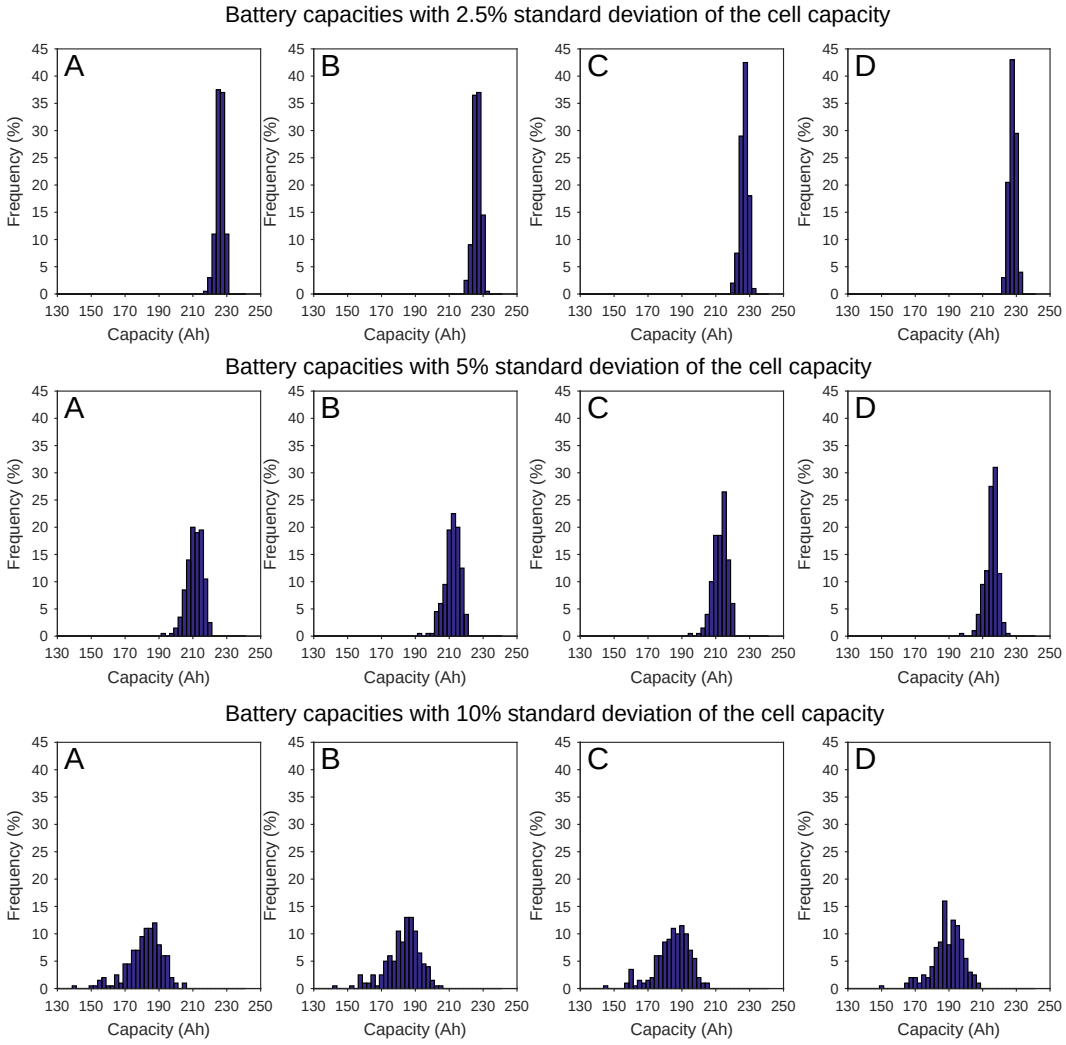

Figure 4.3: *Comparison of the Battery capacities with* $2.5\,\%$*,* $5\,\%$ *and* $10\,\%$ *standard deviations of the cell capacity.*

of these configuration.

An interesting aspect can be noted analyzing in details the capacity of the batteries in each cell extraction. The battery capacity (normalized with a nominal capacity of $240\,\mathrm{A\,h}$) in the first 25 random extractions has been reported in Figure 4.4, in which the minimum cell capacity of each extraction normalized with $60\,\mathrm{A\,h}$ has been also reported. We can note that, sometime, the normalized battery capacity is less than the minimum cell capacity of the pack.

These apparently odd results can be explained analyzing a more simple case with some theoretical considerations. We can use a battery composed of four cells whose capacities are indicated as C_1, C_2, C_3, and C_4 with $C_1 < C_2 = C_3 < C_4$ and $C_1 + C_4 > C_2 + C_3$. The cells are divided in two strings of two series-connected cells (C_1 and C_4; C_2 and C_3) which are parallel-connected. Starting with the fully charged cells, the battery is discharged with a constant current of 1C-rate. Using a very simple ECM model that takes into account only the OCV and the ohmic resistance (R_0), we can

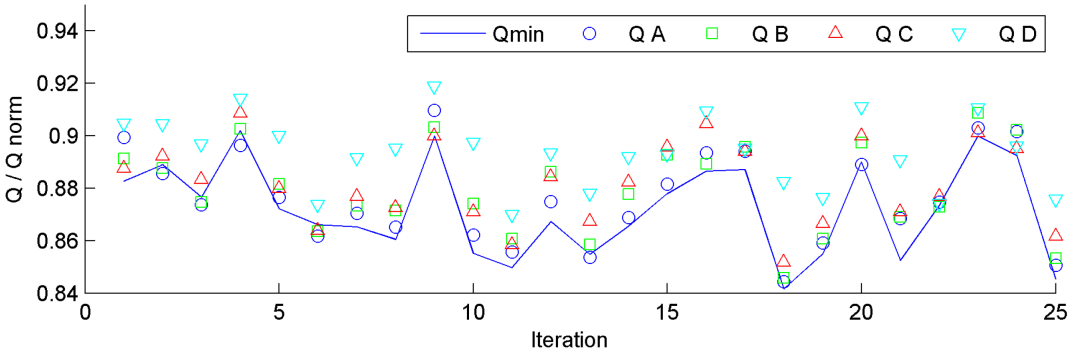

Figure 4.4: *First 25 results of the simulation at* $2.5\,\%$ *standard deviation.*

write the follow equation:

$$\begin{cases} OCV_1 + OCV_4 - (R_{01} + R_{04})I_1 = OCV_2 + OCV_3 - (R_{02} + R_{03})I_2 \\ \\ I_{\text{load}} = I_1 + I_2 \end{cases} \tag{4.1}$$

where OCV_{n} and R_{0n} with $n = 1, 2, 3$, and 4 are the OCV and R_0 of cell 1, 2, 3, and 4, respectively. Moreover, I_{load} is the discharging current, I_1 is the current that flows into cell 1 and 4, and I_2 is the one of cell 2 and 3. In the first moment of the discharge process, the OCVs of the cells are the same and if we consider the R_0 of the cells equal to each other, current I_1 and I_2 are equal. This equality is not continuous for all the discharge time because the capacities of cells are not equal. In fact, $C_1 + C_4 > C_2 + C_3$ and so $SOC_1 + SOC_4 > SOC_2 + SOC_3$ because the cells are discharged by the same current. For this reason, $OCV_1 + OCV_4$ becomes higher than $OCV_2 + OCV_3$ and consequently I_1 increases and I_2 decreases. The system reaches equilibrium when the sum of SOC_1 and SOC_4 is equal to the one related to SOC_2 and SOC_3 and the two decrease with the same velocity. In order to do this, I_1 must be greater than I_2, and so the charge extracted from the first string (Q_1), that is composed of cell 1 and 4, is higher than the second one (Q_2). The discharge process ends when one cell reaches the full discharge condition that in the studied case is represented by the full discharge of cell 1. The total charge extracted from the battery (Q) is equal to the sum of the charge extracted from the two strings. Therefore, Q is equal to $Q_1 + Q_2$ and it is consequently less than $2Q_1$ that is equal to $2C_1$, for the reasons which have just been expressed. In conclusion, we have demonstrated that in this case the normalized charge extracted from the battery that is equal to $Q/2C\text{n}$, where $C\text{n}$ is the nominal cell capacity, is less than $C_1/C\text{n}$ which is the normalized minimum capacities of the cells.

The considerations above suggest that the arrangement of a cell in the battery pack can influence the performance of the battery in terms of capacity. For this reason, the study of the cell arrangement is very interesting and can be done using the presented platform. Starting from a random extraction of the cell capacities, there is a very large number of ways to arrange the cells in the battery pack and, although many of those are equivalent, it is usually impossible to simulate them all. The equivalent permutations can be obtained changing the order of the cells in a string and/or switching one string

with another. For example, considering the battery used before that is composed of 4 strings ($p = 4$) and 24 cells for each string ($s = 24$), the number of all the possible cell arrangements is $(p * s)!$. The number of equivalent permutations depends on the used topology. For each permutation, there are other $p!(s!)^p$ equivalents, if topology A is used; else if the battery is based on topology B, each permutation is equivalent to others $s!(p!)^s$. Therefore, when topology A is used, the $p * s$ cells can be arranged in $(p * s)!/p!(s!)^p$ non-equivalent ways, otherwise they are $(p * s)!/s!(p!)^s$ if B is used. In both cases this number is up to 10^{53}, and so it is impossible to find the permutation which maximizes the capacity of the battery through a brute-force search.

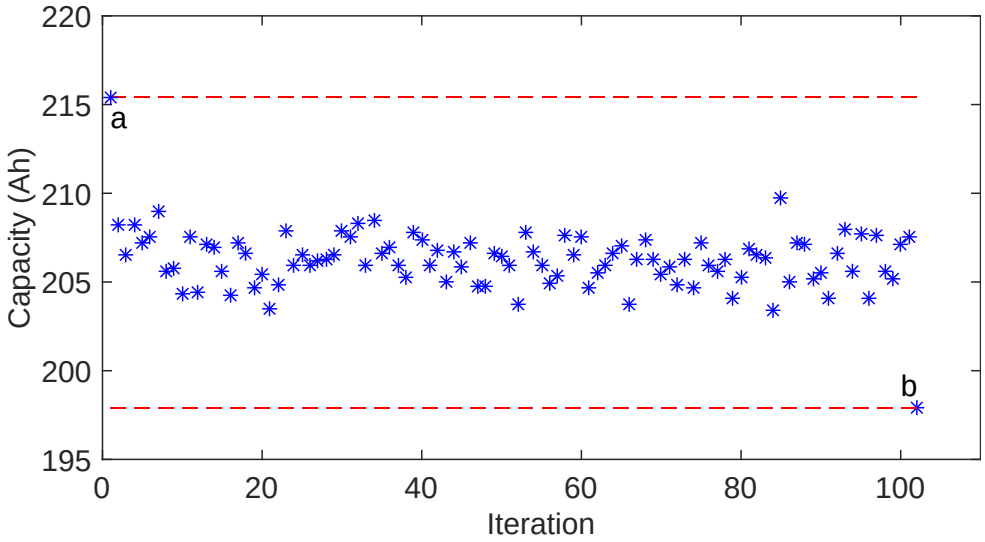

Figure 4.5: *Battery capacities for the best (a) and worst (b) configurations and 100 random permutations of the cells*

Figure 4.5, the capacity of a battery based on the topology A has been reported where the cell positions have been randomly permuted 100 times. Moreover, we have simulated some interesting cases which in our opinion can provide the "best" and "worst" performances. In the best case highlighted in the figure with the letter "a", we have sorted the cells by their capacity from the highest to the lowest and placed the 24 lowest capacity cells in the first string, the cells from 25 to 48 in the second one, the cells from 49 to 72 in the third string and the last 24 cells in the fourth one.

The configuration of the worst case (b) is obtained from the configuration of a, swapping the cells with the lowest capacity of the first and fourth strings, and then rearranging the cells in the first three strings to obtain an average cell capacity of each string as much similar as possible.

With this analysis we have shown some considerations on the dependency of the battery performance in terms of capacity of the connection topology and the arrangement of the cells in the battery pack, but this is not the only criterion in the design of a battery architecture. In some applications, the architecture flexibility, complexity and robustness in respect to the faults can be more important than the battery capacity.

To increase the flexibility and the robustness in respect to the faults, such as the internal short circuit [60], some switches can be added into the architecture with which the topology can be dynamically changed, excluding the problematic cells from the bat-

tery. Therefore, the battery can be auto repaired worsening their characteristics in terms of capacity and maximum deliverable power but allowing the application to conclude the task in execution. A possible application where this is very useful is the public transportation, in which a battery fault could generate a huge disservice for the users.

Unfortunately, the topology D, which is the best choice for the performance, requires a lot of switches to apply this concept. On the contrary, the configuration A requires only p switches, one for each string, to allow the disconnection of a problematic cell from the battery pack. Furthermore, this solution increases the flexibility of the battery, because its size can be easily adapted to the requested run-time from the application task, changing the number of strings assembled on the application. For example, all the vehicles of a minibus fleet can be designed to use a battery of the same size, but in each one only the number of strings which allows the minibus to execute the specific task can be assembled. This approach increases the efficiency of the application because it reduces the volume and the weight of the battery, and reduces the total cost of the minibus fleet.

4.3 Pack Management Unit

The pack management unit is the top hierarchical level of the battery and its main aim is to control the battery behavior according to the application. Therefore, it must be able to monitor and control the state of the modules, to communicate with the application control system, and to manage the connection of the battery with the load and the charger.

The first task can be executed through the communication systems of the modules, which in the presented case are the CAN-bus and the isolated GPIOs. The first one is used to send commands to control the behavior of the modules, such as the cell charge balance procedure and the activation of the fans, and to acquire their status which each module sends as message onto the bus. Instead, the isolated GPIOs are used to generate and receive the high priority signals. The peripheral used to communicate with the application control system depends on the complexity of the application, but it is usually a CAN-bus, which can be also used to communicate with the charger to control the charging phases.

The architecture of a PMU strongly depends on the application field and the relative requested functionalities. In the e-transportation, for example, a very high safety is required and so the battery must be equipped with a protection switch on both the power terminals, a precharge system to limit the rush current, due to the capacity load.

Moreover, complex algorithms can be necessary to estimate the cell internal status, and so the PMU must be based on a high computational power system, such as an FPGA. For example, an accurate SOC estimation is very important, because it is strictly connected to the remaining driving range, and then it is essential for the driver. Furthermore, the internal cell state can be used to extend the battery life, estimating the maximum power that the battery can provide and using the communication with the main control unit to limit it.

The battery can be equipped with a user interface which can be controlled by the PMU and allows the user to monitor and control the battery. In a complex system such as the e-transportation, it is incorporated in the dashboard and the battery information are mediated by the vehicles control system.

CHAPTER 5

72 V Minibus based on fast charging policy

To verify the real benefits of the modular battery, a minibus based on the standard modules and the fast charge policy has been realized in the framework of a collaboration with the ENEA research center in Casaccia. The project will be presented in the following sections, after the definition of the fast charge concept. The use of standard modules has been explained in the previous chapter.

5.1 Fast Charge concept

The lithium-ion technology allows a higher charging power than the other technologies, and then it can be recharged in less time. This feature is at the base of the fast charge concept, which aims to fully charge the battery in the least possible time, or to store the maximum quantity of charge in a fixed charging time. So, the main idea behind the fast charge concept is to charge the battery with the maximum power which it can accept. This technique can introduce many advantages in the public transportation, because this application field is characterized by fixed routes interspersed with rest time in which the buses are stopped in the bus stops, in the terminal stops or in the bus depot. So, if the stations are equipped with fast chargers, the dwell time can be used to apply the opportunity charge technique which consists in recovering the energy consumed in the route extending the bus runtime. In this way, the battery size can be dimensioned to store as much energy as it is required to travel between two recharge stations. Therefore, the electric minibus can be equipped with a small battery, reducing the vehicle weight, the size of the battery compartment, and especially the initial cost. At the same time, a charging infrastructure capable of quickly recharging the minibus battery is needed and this imposes to make an important initial investment [81, 85].

For example, Ke et al. evaluated the total cost of an electric bus fleet to replace

Table 5.1: *Commercial electric bus characteristics*

	Proterra FC	ABB tosa	Proterra XR	New flyer	Ebusco
Bus length (m)	10.6	18.75	10.6	11	12
Lithium-ion technology	LTO	LTO	NMC	NMC	LFP
Battery energy (kW h)	79	38	220	200	311
Charging power (kW)	350	200 (3 min) 400 (15 s)	175	300	308
Charging time per km (s)	16 to 38	67.5 to 33.75	23 to 46.6	21	19

the public transportation system of Penghu, an archipelago of Taiwan [49]. They have considered the costs of e-buses, batteries, infrastructures, and electricity for 10 years of service with different system configurations in term of e-bus battery capacity and charge policy. In particular, two different charge policies have been considered: the night charge one, in which the buses are fully recharged in parking lots at the end of their daily operation, and the night/day charge policy that adds opportunity charge to the first one. This study demonstrates that the opportunity charge reduces the cost of the system because it allows the buses to run more kilometer in a day and so it reduces the number of buses needed to cover the total service kilometers. Similar results are shown in [55], where the e-bus system is also compared with a conventional diesel bus one, demonstrating that this solution is more efficient in terms of energy and more economically convenient than the second system, but it presents a higher initial cost. Another interesting study has been carried out in [53]. The authors have shown that the system sizing problem is not easy to solve because there are many influencing factors, such as the city characteristics where it is applied, the weather condition, the technology of the battery and the type/power of charging stations. Instead in [95] and [78] the authors have developed a model to optimize the recharging schedule in a public transportation network. They show the importance of increasing the charging power of the opportunity charge phases and so the importance of using a fast charge profile to recover the greatest possible energy value in the dwell time.

We can note that each work presented considers only some factors, otherwise the problem becomes too complicated to be faced. Moreover, they conclude that the electrification of public transportation is economically advantageous if the cost of the bus fleet is kept low and they require a very flexible battery which must be able to be dynamically adapted to the bus routes. These two aspects have been used as the basis of this research project which aims to develop a low-cost modular battery.

In Table 5.1, we have reported some specifications of the most important commercial e-buses. We can note that their batteries have been based on different lithium-ion technologies and can store very different quantities of energy. In particular, the LTO lithium-ion technology allows to use very high charging currents but it presents a low density of energy and a high cost. In fact, the buses based on this technology have been equipped with a small battery to keep the cost and weight low. On the other hand, this technology allows to take full advantage of the opportunity charge policy using a very high charging current rate. Instead, the NMC technology has a very good density of energy but it is expensive and cannot be recharged with high charging current rates. Therefore, the NMC batteries are bigger than the LTO ones and the buses that

use them are designed to have a big driving range without the opportunity charge. The LFP cells present a very good trade-off among density of energy, charging current and cost. These characteristics allow them to be used in very different kinds of battery, for example, in the Ebusco bus the battery has been designed to have a very high driving range. At the same time, this technology can be used to design a small battery based on the opportunity charge policy, as it will be clear at the end of this chapter.

To formalize the opportunity charge concept, we can use as figure of merit the charging time needed to travel a specific distance, which represents the penalty on the bus operational time due to the charging time.

We can consider the balance between the energy consumed when traveling and the recharged one, which can be given by

$$P_{\text{chg}} T_{\text{chg}} = F D \tag{5.1}$$

where P_{chg} is the mean charging power, T_{chg} is the charging time, F is the energy consumption for the electric minibus to run $1\,\text{km}$ and D is the distance between two charging stations. So, the figure of merit is given by:

$$P_{\text{chg}} = \frac{F D}{T_{\text{chg}}} \tag{5.2}$$

To decrease the charging time per kilometer of traveled distance we can increase the P_{chg}, but this increases the cost of the charging infrastructures. Moreover, the charging power is limited by the battery capacity and the cell lithium-ion technology used.

The commercial buses present a charging time per km ranging from $16\,\text{to}\,67.5\,\text{s}$. These good values have been obtained in the Protera FC and ABB tosa using the LTO characteristics and in Protera XR, New flyer and Ebusco using a big size battery. The aim of this project is to obtain about the same value using the low cost LFP cells and a small battery to keep the cost low.

A good goal is to achieve $1\,\text{min}$ of charging time per kilometer of traveled distance. This means that: if we assumed an average speed of $10\,\text{km}\,\text{h}^{-1}$, the minibus needs to be recharged for $10\,\text{min}$ each hour of traveling time. Such a short charging time can easily be overlapped to the normal standstill time due to passenger boarding and alighting.

The most important problem introduced by the fast charge will be the accelerated aging of the battery. In fact, many works have been carried out on this topic, for example in [2, 3] the authors have studied the effect of the high charging current rate on different cell technologies. They conclude that the shape of charging current profile has more impact on the battery aging than the charging current rate. Moreover, a pulse current profile is better than the classic CC/CV one because it reduces the electrochemical stress in the cells.

To understand the effect of the fast charge on the characteristics of the cells used in this project a specific test campaign has been carried out and its results have been presented in [36].

In this test, we have simulated the use of the cells in the battery of the minibus in which the fast charge concept is applied. The HP-PW-60Ah cells are tested repeating a profile made of four steps: a discharge step with a constant current of $2/3\,\text{C}$ $(40\,\text{A})$ for

1200 s, a rest time of 60 s, a charge step with a constant current of 3 C (180 A) for 300 s which recharges the energy used in the discharging step and a rest time step of 60 s. After more than 2000 cycles the cells did not show a reduction of performance higher than the one due to the normal aging [9]. This demonstrates the usability of the chosen cells in the minibus which adopt a fast charge policy.

5.2 Case study

To reduce the development time, cost and complexity of the project, we decided to start from a commercial electric minibus, originally equipped with a lead acid battery which is replaced with a custom battery based on the modular architecture presented in the previous chapter.

5.2.1 Commercial electric minibus

The chosen minibus is a TECNOBUS Gulliver U520 model, shown in Figure 5.1, which is designed to work in an urban context such as historical city centers, university campuses or hospitals. This kind of minibuses is perfect to study the fast charge concept because its limited dimensions are not able to contain a big battery. So, the fast charge concept can increase their driving range making the minibuses able to perform an entire working day.

Figure 5.1: *Photograph of the electric minibus.*

The minibus characteristics are summarized in the Table 5.2. We note that the TECNOBUS Gulliver U520 is equipped with a 25 kW electric motor which provides a maximum torque of 235 N m at 950 rpm; its speed is limited to 33 $\mathrm{km\,h^{-1}}$ by the vehicle control unit and its nominal energy consumption is around 500 $\mathrm{W\,h\,km^{-1}}$. The minibus was originally powered by a 72 V and 585 A h lead-acid battery which was arranged in two cases of $(1210 \times 541 \times 375)\ \mathrm{mm^3}$.

5.2.2 Lithium-ion Battery

The standard module size of 60 A h is the best choice for this application because it offers the best trade-off between cost, maximum allowed power, and flexibility. In fact,

Table 5.2: *Characteristics of the case-study electric minibus*

Curb weight (without the traction battery)	$(2800 \pm 100)\,\mathrm{kg}$
Length	$5.1\,\mathrm{m}$
# Passengers	27 (10 of which are seated)
Traction power	$25\,\mathrm{kW}$ (peak), $20\,\mathrm{kW}$ (nominal)
Average energy consumption per kilometer	$500\,\mathrm{W\,h\,km^{-1}}$
Original lead acid battery	$72\,\mathrm{V}$, $585\,\mathrm{A\,h}$, $1500\,\mathrm{kg}$
Volume available for the battery	$2\times(1210 \times 541 \times 375)\,\mathrm{mm^3}$

Table 5.3: *Characteristics of the battery charger*

Input	$400\,\mathrm{V}$ three-phase AC , 50-60 Hz
Output voltage	$60\,\mathrm{V}$ to $87.6\,\mathrm{V}$
Continuous output current	$360\,\mathrm{A}$
Continuous power @ $72.8\,\mathrm{V}$	$26\,\mathrm{kW}$
Efficiency	$>85\,\%$

a battery composed of modules with cells of $30\,\mathrm{A\,h}$ is more flexible but has an over cost due to the necessity of using a double number of modules with respect to the $60\,\mathrm{A\,h}$. At the same time, the modules of $100\,\mathrm{A\,h}$ allow us to decrease the cost, but they are less manageable and the battery arrangement in the minibus is more complex.

To reuse as much as possible of the minibus structure and the control units, the developed custom battery has the same voltage and dimensions of the original one. In the volume reserved to the battery, we can arrange up to 24 modules which must be arranged in a matrix composed of 6 rows to obtain a battery voltage of $76.8\,\mathrm{V}$, compatible with the input voltage of the minibus control unit. We have chosen the connection topology A presented in Section 4.2, in which the modules are connected in series to compose a string, and the strings are parallel-connected to make the battery. In this battery, the strings are not statically connected, but each string can be dynamically connected to the others through a power switch. This choice makes the battery very flexible and allows us to dynamically change the capacity of the battery in order to verify the behavior of a minibus with a battery capacity of $60\,\mathrm{A\,h}$, $120\,\mathrm{A\,h}$, $180\,\mathrm{A\,h}$ and $240\,\mathrm{A\,h}$, using 1, 2, 3 or 4 parallel-connected strings, respectively.

The battery implementation is explained in detail in the follow section.

5.2.3 Charger

The used charger was selected from commercially available devices, its photo is shown in Figure 5.2, and in the Table 5.3 we have reported its main specifications.

This charger, manufactured by Zivan, has been chosen because it is based on a modular approach, so the maximum required charging power can be obtained connecting in parallel a variable number of modules. The basic module, called NG9, is shown in Figure 5.3.

Four modules have been used in this work to provide an overall continuous charging power of $26\,\mathrm{kW}$ and a continuous current of $360\,\mathrm{A}$ with a battery voltage of $72.8\,\mathrm{V}$.

Figure 5.2: *Photograph of the charger.*

Figure 5.3: *Photograph of the charger module.*

Another important feature of this charger is the CAN-bus interface with which the charging parameters can be changed and the most important internal variables and the measured quantities can be read.

5.3 Battery implementation

To implement the battery, 24 standard modules have been made using the $60\ \mathrm{A\,h}$ cells, MMU and a metallic case which allow us to easily assemble the modules in the in two battery cases of the minibus. The MMU is divided in two electronic boards. One board has been designed to simplify the assembly of the cells in the modules and the second one, the main board, to implement the functionalities presented in Section 4.1.1. The first one supports the aluminum bars used to connect the cells in series and the negative and positive terminals of the modules which are connected to the negative pole of the first cell and the positive one of the last cell, respectively. This board also organizes the wiring of the measurement of the temperature and voltage of each cell, grouping the relative signals on a single connector. In this way, a single flat cable can be used to route the signals from the cells to the main board.

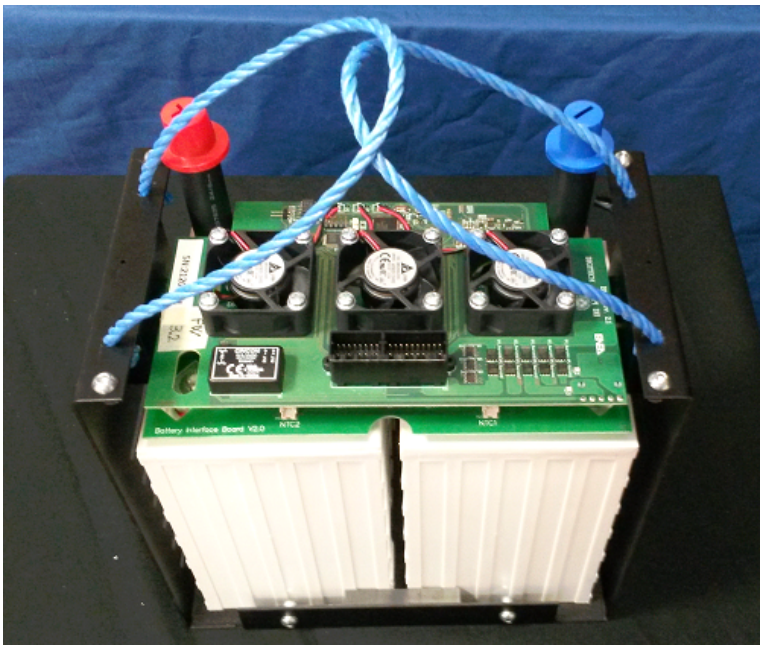

Figure 5.4: *Photograph of the standard 12V 60Ah battery module (the case lid has been removed to show the module management (MMU) electronic boards).*

The photo of a module is shown in Figure 5.4, where the upper part of the case has been removed to show the internal parts. From the figure, we can note the prismatic cells connected on the upper side to the connection board. On the top, the main board is assembled. It is characterized from the three fans which allow it to generate an air flux to cool the cells, and a main connector with which the modules are connected together and with the PMU to make the communication bus and the auxiliary signals.

The battery architecture is shown in Figure 5.5, in which the 24 modules arranged in 4 strings, the parallelization and protection switch, and the pack management unit have been reported. Each string is composed of 6 modules connected in series and is provided of a balancing circular bus with which the charge stored in the modules can be equalized using the balancing circuit presented in Section 2.2.3. The modules of all the strings are also connected on a CAN-bus which is extended in the battery and connects the modules to the PMU.

The first module of each string is provided with a current sensor, used to measure the current which flows in the string. To reduce the costs, the other modules are not equipped with a current sensor and receive this information through the CAN-but by the first one.

A contactor EV200, manufactured by Tyco, is connected in series to each string that can carry a continuous current $500\,\mathrm{A}$ @ $85\,^{\circ}\mathrm{C}$ and withstand a voltage of $320\,\mathrm{V}$. The switches are indicated in the figure as $\mathrm{Sw}_1 \ldots \mathrm{Sw}_4$ where we can see that they are controlled by the PMU in order to connect in parallel the strings. In the PMU a parallelization algorithm like the one presented in Section 3.1 has been implemented, whose key goal is to maximize the sharing of the current drawn by the minibus between the strings, maintaining every cell inside the safety operating area of voltage, current and temperature. The activation signal of a string switch, generated by the PMU, is

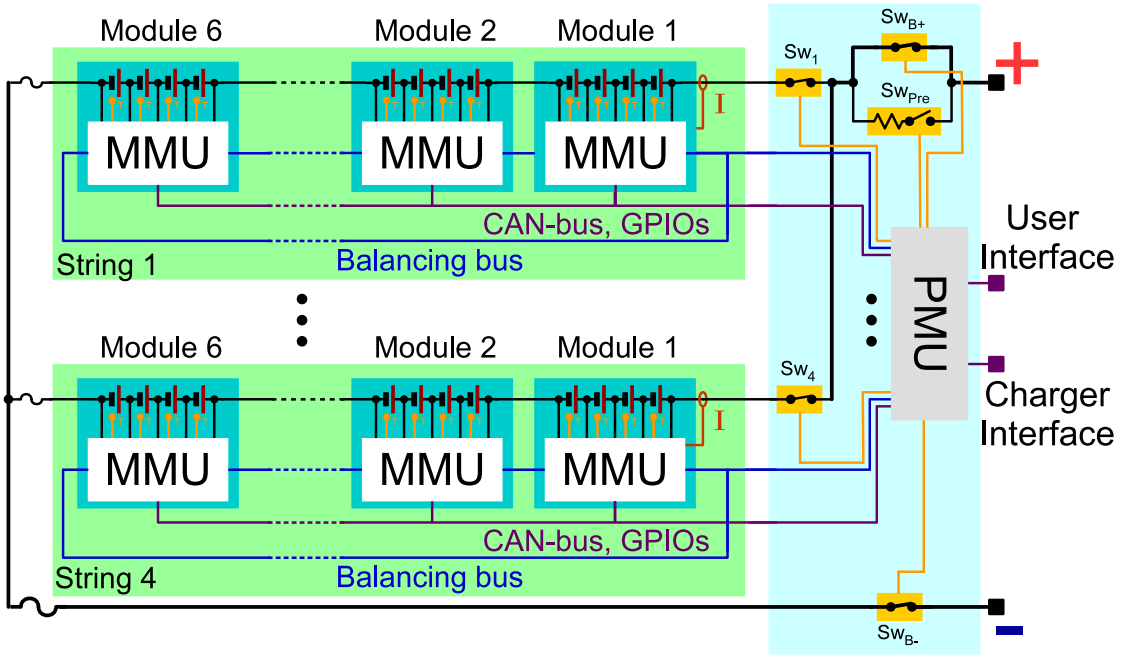

Figure 5.5: *Battery architecture.*

AND-wired with the safety signals produced by the 6 MMUs (and routed to the PMU through isolated GPIOs). In this way, each module can interrupt the current flowing in the corresponding string, independently by the PMU, to achieve a prompt and robust protection mechanism.

The battery is also provided with classic protection switches (S_{WB+} and S_{WB+}), connected in series to the positive and negative terminals, with which the PMU can control the connection of a battery with the load and the charger. To reduce the bill of material, these switches are implemented with the same contactor used to parallel-connect the strings. A percharge resistor and a relay are connected in parallel to the S_{WB+} switch to limit the in-rush current that flows when the battery is connected to a load with an input capacitance. To increase the battery safety, each string and the battery negative terminal are equipped with a fuse which has a nominal current of 200 A and 355 A, respectively.

The block diagram of the PMU is shown in Figure 5.6. This board is based on the NXP LPC1756 microcontroller, which belongs to the same family of the microcontroller used in the MMU. This microcontroller has been chosen because it is equipped with two CAN-bus peripherals, one used to communicate with the modules and the other with the UI and the charger. The possibility to communicate with the charger is very useful in this project, because the battery can configure the charger in the fast charge phases in according to the driver directives. The PMU has been equipped with isolated GPIOs with which it can read some signals of the minibus, such us the activation of the key, and can provide high priority signals to the modules, for example the wake-up signal.

The PMU also incorporates 4 isolated DC/DC converters (one per string), powered by the highest voltage string. The output of each converter is connected to the balancing bus of one of the 4 strings. Consequently, energy can be moved from the most charged

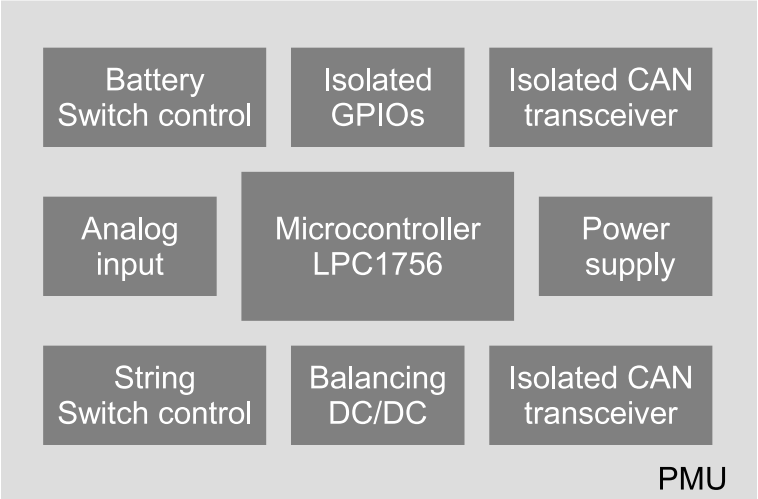

Figure 5.6: *Schematic block diagram of the PMU.*

string to a generic cell of the battery. With the addition of this system all the cells of the battery can be balanced. In fact, the implemented balance system of the MMU allows to balance the stored charge of the four cells of each module. The circular balancing bus allows us to balance the charge of the six modules of each string and the stored energy of each string can be balanced using the DC/DC converters of the PMU.

5.4 User interface

The User interface has been developed in LabVIEW environment and allows the driver to verify the battery status, to configure the control parameters and to control the charging phase.The interface saves all the battery data on a log file which can be analyzed to understand the benefits of the lithium-ion technology in the electric public transportation. These data are also indispensable to develop and test new algorithms or control procedures to improve the use of lithium-ion batteries. The UI is connected to the battery with a dedicate CAN-bus port, using a USB-CAN adapter. It is divided in some tabs.

Figure 5.7 shows the main tab of the user interface (UI). This tab shows on the top the battery information, such as voltage, current, SOC, the status of the safe flag signals of the strings and the parallelization and protection switch status. In this section, the driver can also send the most important commands, like the control of the switches, the SOC calibration and the power-up/power-down of the modules. In the middle part, the strings information are summarized and, in the low section, the information of a single selectable module are reported.

Another important function of the interface is to allow the driver to enable the energy equalization functionality. As mentioned before, the battery BMS is equipped with an innovative balancing circuit divided in two different layers: from the module to its cells and from the most charged string to each cell of the battery. The driver can activate the first balancing layer through the interface which sends the specific command to all the battery modules. Each module enables the equalization procedure whose aim is to balance the voltage of its cells. The equalization of the cell voltages guarantees

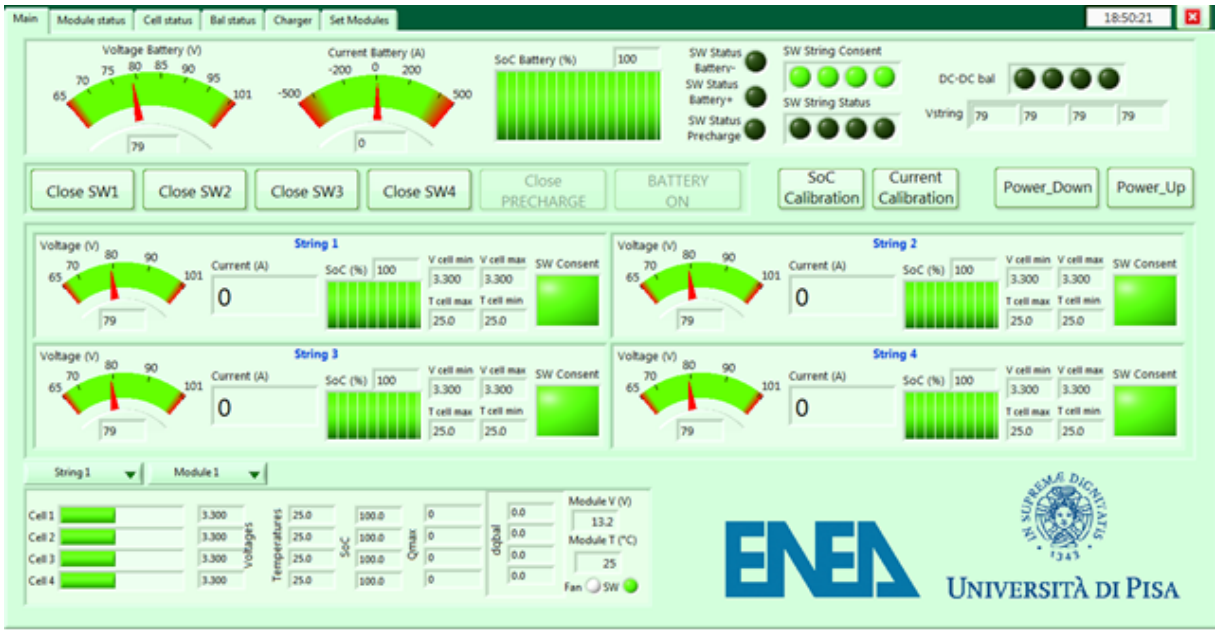

Figure 5.7: *Screenshot of the Main tab of the User Interface developed in LabVIEW.*

the balancing of the energy stored in the cells because the current of the equalization system is low and so the cell voltages are approximately equal to their OCV. Therefore, if the cell voltages are balanced, their SOCs are balanced as well. In order to do this, the module analyzes the cell voltages computing the maximum voltage difference. If this value is higher than a settable value (ΔV_{max}), the module enables the balancing DC/DC and selects the cell with the lowest voltage through the equalization switch matrix. This cell will be recharged for a specific period (Δt) after which the module analyzes the cell voltages again and repeats the procedure until the maximum cell voltage mismatch is lower than ΔV_{max}. When this procedure is completed, the SOCs of the cells of each module are balanced but the energy stored in the modules can be different.

To equalize the energy of each module, the second layer of the balancing system can be used. This layer is directly controlled by the interface which starts the equalization procedure after a driver's command. The interface calculates the differences between the highest cell voltage of the battery and the lowest cell voltage of each string. It compares each of these values to the ΔV_{max} and if they are higher than it, the interface enables the PMU balancing the DC/DC of the relative string and configures the switch matrix of the string modules to connect the DC/DC output to the cell with the lowest voltage. After a period of Δt the interface repeats the procedure until the differences between all the cell voltages are lower than ΔV_{max}.

We have decided to entrust the driver with the control of the equalization system because it is a time consuming maintenance procedure. Therefore, the driver can activate it when the bus has remained unused for a long time and the battery can be fully charged when the procedure is concluded.

5.5 Experimental validation

The battery pack has been assembled and, after the first successful laboratory test, has been mounted on the minibus, as shown in Figure 5.8. Three types of test have been conducted to assess the performance of the electric minibus in terms of driving range and charging time per unit of travel distance in a wide range of conditions. First of all, the minibus has been tested on a chassis dynamometer which allows us to verify the minibus behavior in a controllable and repeatable way and to acquire some mechanical quantities, such as torque and speed. The success of these tests and the encouraging results pushed us to carry out a road test campaign inside the ENEA research center of Casaccia. Three different routes has been identified to measure the average energy consumption in situations as close as possible to the real usage of the minibus. During all the tests, the PMU is connected to the user interface to record the current, voltage, and temperature of each cell and the general battery status in order to perform offline processing. Furthermore, the driver is able to control the battery pack behavior, for example, by choosing the number of parallel-connected strings. In fact, some tests have been carried out with all the 4 strings in parallel (full battery case), while others with only two strings (half battery case). The last case is used to verify the feasibility of a minibus with a very small battery which leads to a high reduction of weight, volume and cost.

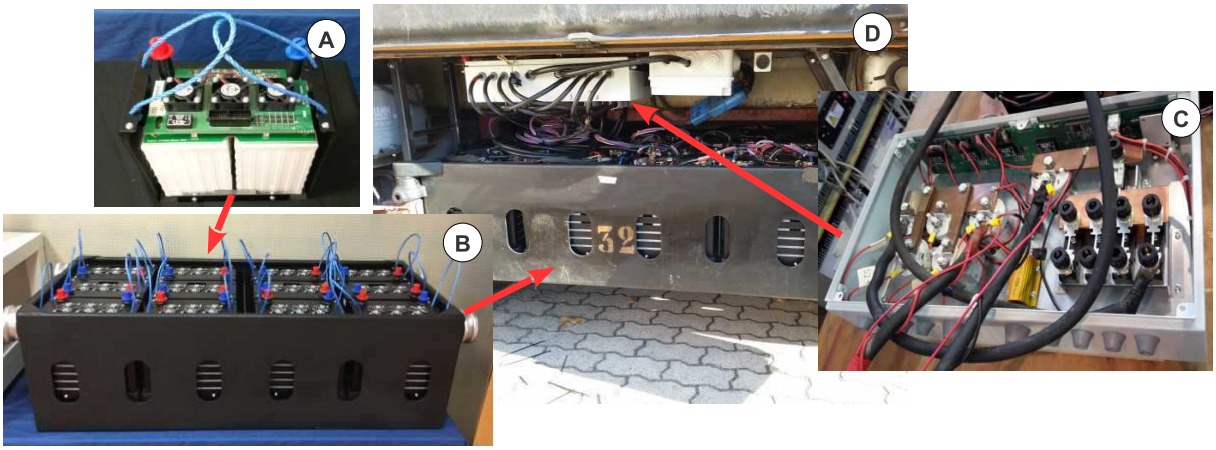

Figure 5.8: *Photograph of battery pack and its integration into the minibus. A shows the 12V standard module; B one battery housing containing 2 battery strings (without the power and signal wire harness); C the pack management unit; D the placement of one battery housing and the pack management unit in the minibus.*

5.5.1 Chassis dynamometer test results

A photo of the minibus running a chassis dynamometer test is shown in Figure 5.9. The first Standardized On-Road Test (SORT) driving cycle [34], defined by the international organization for public transport authorities and operators (UITP), has been chosen to emulate the urban driving scenarios and measure the performance of the minibus in terms of driving range and average energy consumption per kilometer. The SORT 1 cycle models a city route with a heavy traffic condition and then is characterized by continuous start and stop phases. The speed acquired by the dynamometer chassis and

Figure 5.9: *Photograph of the minibus during a test session on the chassis dynamometer.*

the electrical power provided by the battery, during two SORT 1 cycles, have been displayed in Figure 5.10.

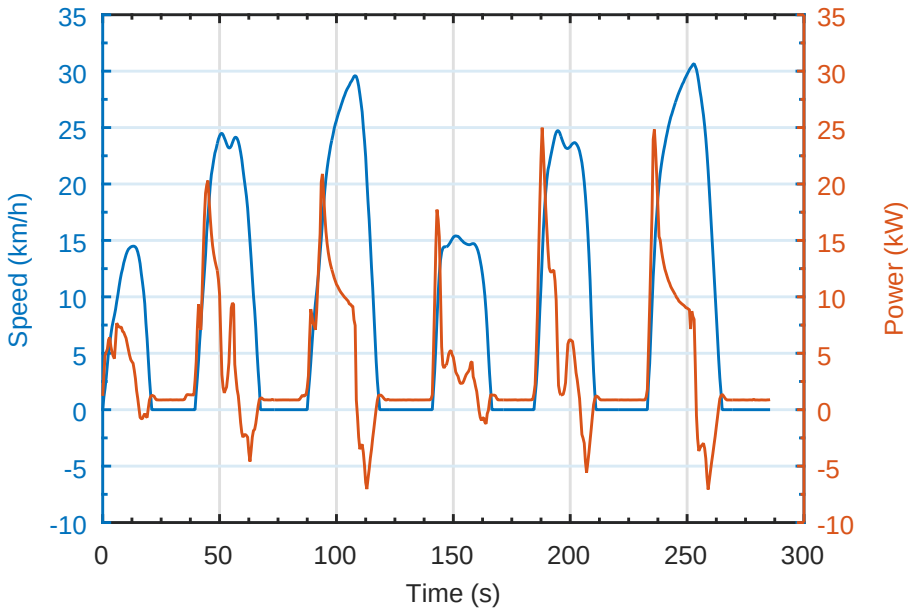

Figure 5.10: *Speed and electric power during two SORT 1 cycles.*

We can note that the SORT 1 cycle describes about 150 s, so it is repeated for a fixed number of times or until the battery is fully discharged. Using this speed profile, two situations have been tested: full battery case and half battery case.

Full battery case

The minibus has been driven on the chassis dynamometer repeating 86 SORT 1 cycles, starting from the fully charged battery condition. Table 5.4 reports the main results. In particular, the minibus consumed about $383\,\mathrm{W\,h\,km^{-1}}$, maintaining an average speed

Table 5.4: *Summary of chassis dynamometer tests (full battery)*

Time		$3.5\,\mathrm{h}$		
Length		$31.7\,\mathrm{km}$		
Number of SORT1 cycles		86		
Start / End voltage		$80\,\mathrm{V}$ / $77\,\mathrm{V}$		
	string 1	string 2	string 3	string 4
Charge delivered by ($\mathrm{A\,h}$)	35.0	40.5	41.0	44.4
Energy delivered by ($\mathrm{kW\,h}$)	2.64	3.07	3.09	3.34

Table 5.5: *Summary of chassis dynamometer tests (half battery)*

Time	$2.5\,\mathrm{h}$	
Length	$22.5\,\mathrm{km}$	
Number of SORT 1 cycles	61	
Start / End voltage	$81\,\mathrm{V}$ / $69\,\mathrm{V}$	
	string 3	string 4
Charge delivered by ($\mathrm{A\,h}$)	53.8	55.8
Energy delivered by ($\mathrm{kW\,h}$)	3.92	4.08

of $9.1\,\mathrm{km\,h^{-1}}$ and running about $31.7\,\mathrm{km}$. We can note that the energy and the charge delivered by the four strings is not balanced, and the string1 provided only the $22\,\%$ of the total energy respect to the $27.5\,\%$ delivered by the string 4. This behavior tends to degrade the usable capacity of the battery and then must be avoided. A specific test campaign has been carried out to individuate the source of this problem which can be attributed to the difference of the resistances in the power connections between the cells of a module and the external terminals. To measure these resistances, a current of 1 C-rate ($60\,\mathrm{A}$) has been applied to each module and the voltages across the contact resistances have been acquired. The results of this test highlighted a very wide range of the resistances value which changes from $0.1\,\mathrm{m\Omega}$ to $7\,\mathrm{m\Omega}$. This difference is due to the low precision of the mechanical processing which has been executed to assemble the battery prototype and can be easily solved in an industrial production line.

Half battery case

A similar test has been carried out using only two fully charged strings (string 3 and 4). In this case, the half battery has been discharged repeating 61 SORT 1 cycles which correspond of about $22.5\,\mathrm{km}$ ran by the minibus in about $2.5\,\mathrm{h}$. The main results of the test have been reported in Table 5.5. This test demonstrates that the minibus can be powered by a very small battery, inasmuch the battery current is lower than the maximum allowed by the used lithium-ion technology (equal to 3 C-rate), as shown in Figure 5.11. At the same time, the driving range is very limited and the minibus can be used only if a fast charge concept is applied.

5.5.2 Road test results

Three different routes in our private testing site (the ENEA research center of Casaccia) have been individuated to safely verify the behavior of the minibus on the road. All the

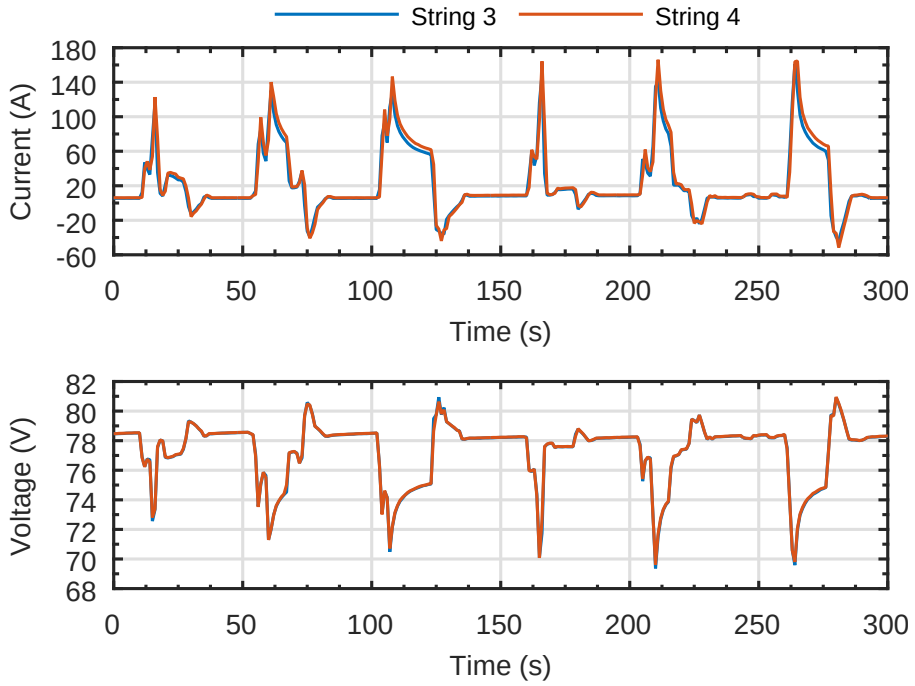

Figure 5.11: *Current and voltage of the string 3 and 4 in the half battery chassis dynamometer test.*

routes connect point A to point B, as shown in Figure 5.12, following three different ways. In Route 1, the minibus runs back and forth from point A to B using the street highlighted in yellow. Route 2 is longer than Route 1, because it follows the street highlighted in green. Instead, the minibus goes from A to B along the green street and comes back from B to A following the yellow street, when it runs on the Route 3 as highlighted in red. In Figure 5.13, we have shown the speed of the minibus, the power delivered by the battery and the energy delivered by the four strings during a test in which the minibus was running on the Route 2.

The results of the tests on the minibus running on the three routes are summarized in Table 5.6. We can note that the routes are not very long but are compatible with the real usage of a minibus in contexts such as hospitals, universities, airports or large factories. Finally, the measured average energy consumption per kilometer is around $370\,\mathrm{W\,h\,km^{-1}}$ which is reasonably less than the nominal value of $500\,\mathrm{W\,h\,km^{-1}}$, as the adoption of the lithium-ion batteries saves about $750\,\mathrm{kg}$ in the bus weight.

Moreover, we can note that the minibus in Route 2 requires an average energy consumption per kilometer lower than the other routes. This is because Route 2 has a slight uphill slope from A to B and a consequent downhill slope from B to A.

5.5.3 Fast charge test results

In the previous test phases the energy consumption per kilometer has been measured in different conditions. In this phase, our aim is to measure the maximum power at which the battery can be charged to quantify the benefits of a fast charge approach. They are carried out by applying a fast charge pulse to the battery and measuring the time needed to recharge it by $500\,\mathrm{W\,h}$.

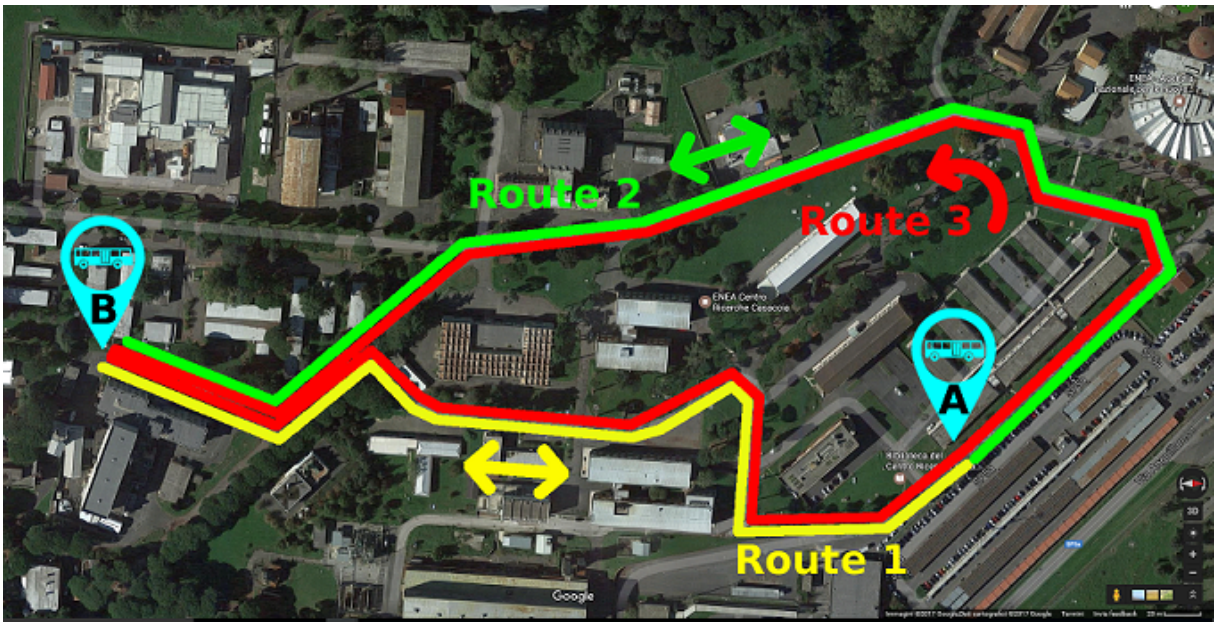

Figure 5.12: *Representation of the three routes inside the ENEA research center of Casaccia.*

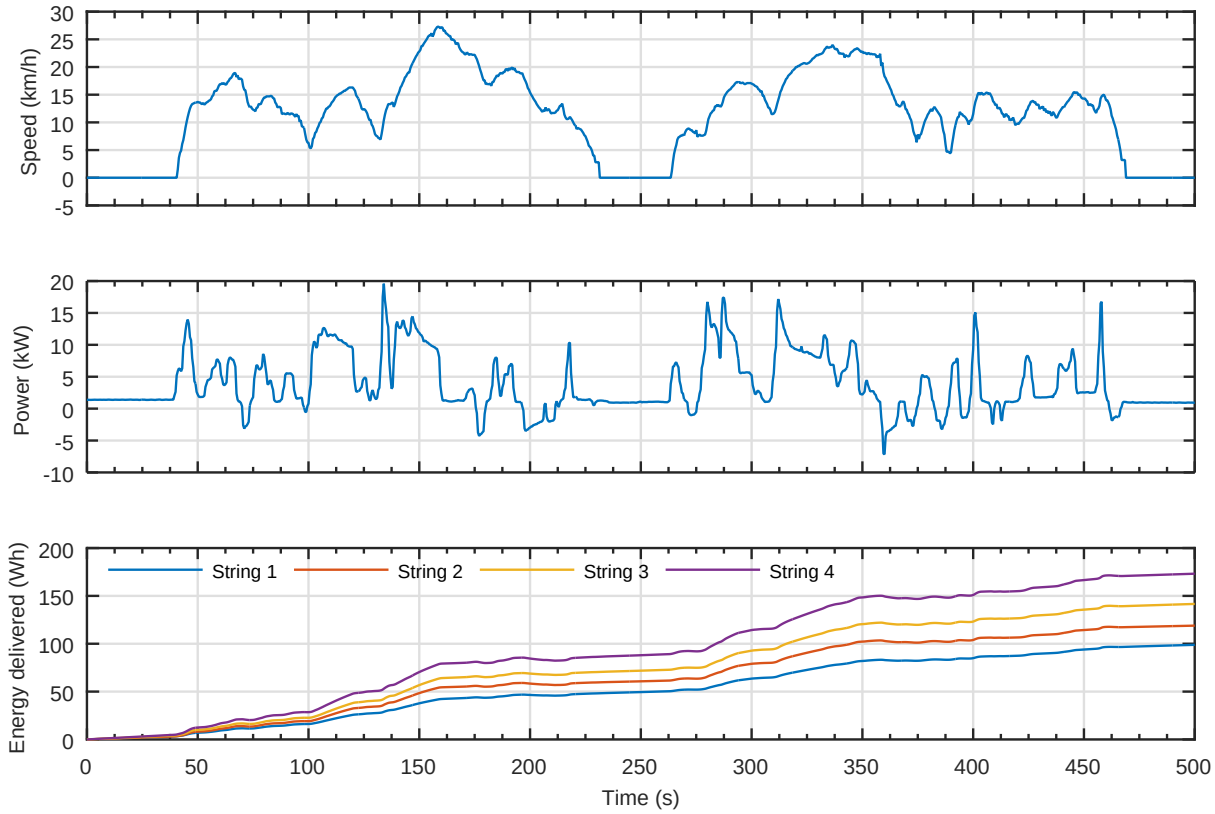

Figure 5.13: *Speed, electric power and energy delivered by the battery during the Route 2.*

This energy value has been chosen because is the nominal energy consumed per kilometer by the minibus. Moreover, this value is higher than the measured energy

Table 5.6: *Summary of road tests (full battery)*

	Route 1	Route 2	Route 3
Time (s)	438	500	417
Length (m)	1104	1599	1146
Average speed ($\mathrm{km\,h^{-1}}$)	9.08	11.50	10.57
Average Power (kW)	3.44	3.83	3.80
Charge delivered (A h)	5.41	6.86	5.71
Energy delivered (W h)	418	533	441
Energy for km ($\mathrm{W\,h\,km^{-1}}$)	379	333	385

consumed per kilometer by the minibus equipped with the designed lithium-ion battery, so the experimental results can be used also for lower energy consumptions, by just considering only the initial part of the pulse needed to recovery the used energy.

The charging procedure is based on a classic CC/CV mode, where the charger constant current is set to the maximum allowed by it (360 A) and the constant voltage value is of about 86 V. This is slightly lower than the maximum charging battery voltage, given by the cell cut-off charge voltage. Actually, we expect that the charger may never enter the CC mode and operate only in the CV mode for higher SOC levels, due to the ohmic voltage drop on the internal cell resistances and the connection ones. For this reason, we have applied the charging pulse to different values of the battery SOC to explore the charger-battery interaction and to measure the time needed to recharge the battery of a fixed energy quantity.

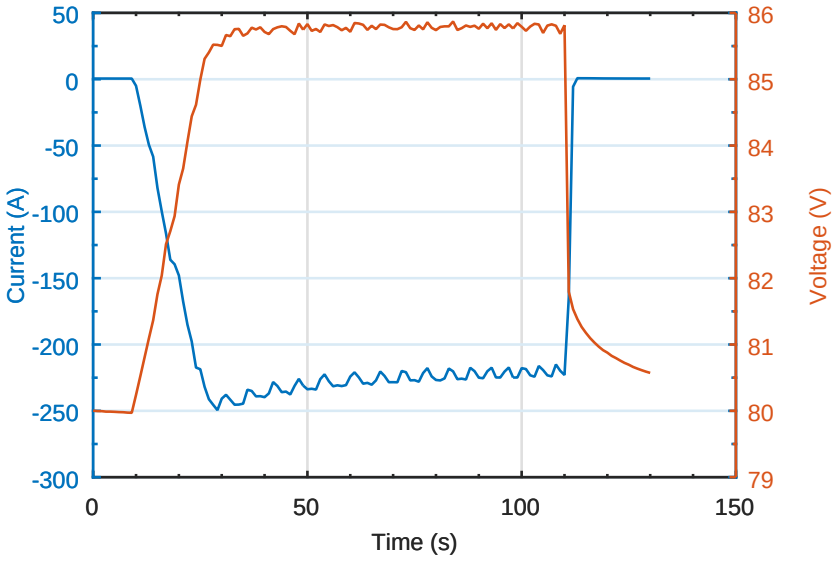

Figure 5.14: *Current and voltage of the battery during the fast charge experiment starting at SOC =* 70 %.

Due to the limitations on the maximum charging current imposed by the selected charger, these tests are performed with the battery consisting only of string 3 and 4. The results can be generalized doubling the maximum allowed power and halving the charging time needed to recover a specific energy quantity. The battery voltage and

Table 5.7: *Summary of fast charge tests (half battery)*

Initial SOC (%)	Charging time (s)	Average current (A)	Charging power (kW)
0	80	-279	22.50
10	80	-263	22.50
25	96	-222	18.75
70	100	-208	18.00

current of a pulse relative to the $70\,\%$ of SOC have been reported in Figure 5.14, where we can note that the rise time of the current is significantly long and the charger goes directly in CV with a charging current of about $225\,\mathrm{A}$ (1.87 C-rate of two strings). The first problem is due to the fact that the main driving factor in the choice of charger has been the low cost. However, this aspect does not change the validity of the results which could be improved using a higher performance charger.

The main results of the pulses are summarized in Table 5.7, where we can note that the average charging power is about $22\,\mathrm{kW}$ with the battery SOC up to $10\,\%$. When the SOC is higher than $70\,\%$ the average power becomes lower than $18\,\mathrm{kW}$.

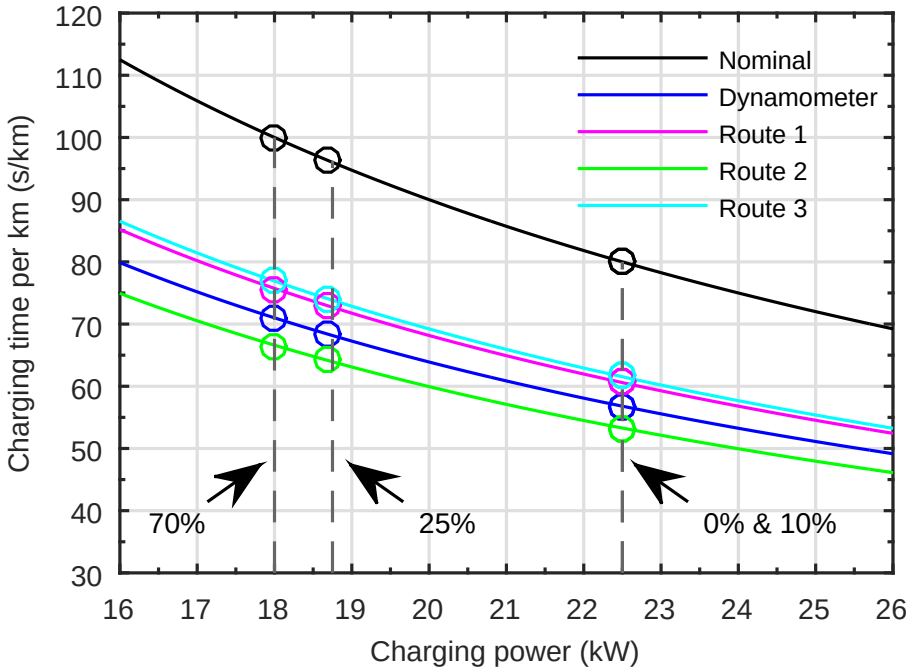

Figure 5.15: *Charging time to run* $1\,\mathrm{km}$ *in different conditions.*

5.5.4 Test results discussion

The charging time to recover the energy used in the three routes presented in the previous section is reported in Table 5.8. In particular, we have considered three different values of battery SOC to show the dependency between the recharging time and the battery SOC.

Figure 5.15 summarizes the presented results and highlights the effect of the fast

Table 5.8: *Summary of fast charge tests*

	Running time (s)	Charging time (s) @ SOC 10 %	25 %	70 %
Route 1	438	67	80	84
Route 2	500	85	102	107
Route 3	417	70	85	88

charge concept. We have plotted the Eq.(5.2) for different values of energy consumed per kilometer by the minibus, measured in the tests. This equation describes the relation among the charging time, the charging power to balance the recharged energy and the energy-per-distance value used in the traveling phases. In the figure, the charging power obtained in the fast charging test has been reported to identify the charging time needed to recover the energy used by the minibus to run $1\,\mathrm{km}$. It is worth noting that the charging time in all the driving conditions is about $1\,\mathrm{min\,km^{-1}}$ (which is the target value), if the minibus operation in the range from $0\,\%$ to $15\,\%$. Otherwise, the charging time is higher but stills very promising.

However, it is important to note that the shown results have been obtained using only two strings, the presented charger, and the experimental battery. Indeed, if we use all the strings of the battery and a charger with a double charging power, the charging time to recover the energy used in a kilometer will become the half of that just calculated. Moreover, this time can be also reduced using a higher performance charger in terms of current rise time because the charger used takes a long time to build up the charging power as shown in the previous subsection. Another factor that has limited this parameter is the homemade solution adopted to build the battery. In fact, an industrial assembly of the battery will reduce the wiring contact resistances thus increasing the time in which the battery can be maintained in the CC charging phase, thereby increasing the charging power. For these reasons, we can assert that the target value of the charging time can be obtained by using the describes approach and applying these design improvements.

CHAPTER 6

Standard battery for medium-power applications

In the last years, the use of lithium-ion batteries is growing in the medium-power/energy applications, such as e-bikes, e-scooters and power tools used for building, gardening, and horticulture applications. While the performance benefits of adopting the lithium-ion battery technology are unquestionable in these applications, the associated cost is still relevant. In fact, the battery is often the most expensive component of the system. Therefore, the manufacturers develop a large family of tools powered by the same battery in order to share its cost among many devices. This concept can be pushed to the limit using the modular approach, presented in Chapter 4, defining a smart battery system that can supply a very large number of devices with the same voltage but different requirements in terms of power and energy. The most suitable standard block is a standard battery with a small capacity and capable to be parallel-connected. In this way, the battery system is very flexible and allows us to obtain a good compromise between volume, weight, cost and application runtime, choosing the best number of parallel-connected standard batteries for each specific application. Furthermore, in these applications, the power requirement is not very high and can be easily provided by a battery with a capacity of some Ah (from $1\,\mathrm{A\,h}$ to $5\,\mathrm{A\,h}$). For this reason, the manufacturer can equip the tool with more slots, where the standard batteries can be connected using appropriate approaches. It allows the users to choose the number of the standard batteries to use, depending on the desired runtime and the cost that they are willing to pay.

Typically, these applications require a battery voltage of $36\,\mathrm{V}$ or $48\,\mathrm{V}$, a capacity in the range of $5\,\mathrm{A\,h}$ to $20\,\mathrm{A\,h}$ and use the high-power NMC cells, which allow a very high discharging power and present a good energy density. Therefore, two standard batteries can be defined to power the tool line with $36\,\mathrm{V}$ and $48\,\mathrm{V}$ as nominal voltages, respectively, and with $5\,\mathrm{A\,h}$ as nominal capacity.

Table 6.1: *Main characteristics of cell LG Chem LGDBHE21865*

Item	Condition	Specification
Nominal capacity	Std. Charge/Discharge	2500 mA h
Nominal voltage	Average for Std. Discharge	3.6 V
Standard Charge	Constant current	1250 mA
	Constant voltage	4.2 V
	End condition	50 mA
Fast Charge	Constant current	4000 mA
	Constant voltage	4.2 V
	End condition	100 mA
Standard Discharge	Constant current	500 mA
	End condition	2.5 V
Maximum Discharge	Constant current	20 000 mA
	End condition	2.5 V
Operation temperature	Charge	0 °C to 50 °C
	Charge	−20 °C to 75 °C

6.1 Standard battery

In this work, we have analyses the standard battery with 48 V as nominal voltage and capacity of 5 A h. It is composed of 24 high-power NMC cells that present a nominal voltage of 3.7 V and a capacity of 2.5 A h. The used cells are manufacture by LG Chem with the part number LGDBHE21865 and its main characteristics are summarized in the Table 6.1.

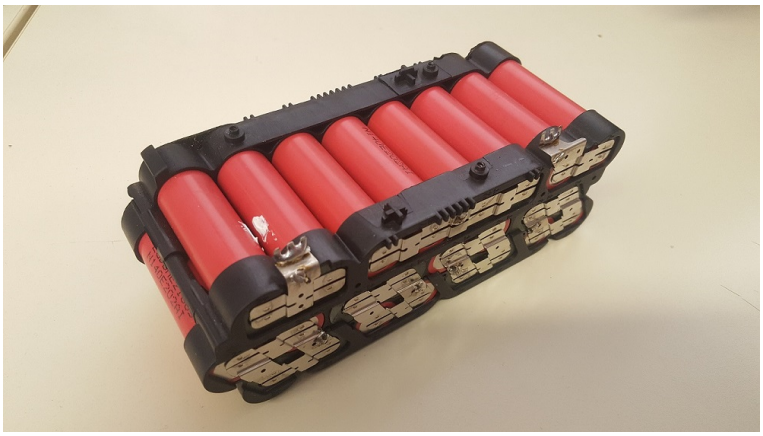

Figure 6.1: *Photograph of the used cell pack.*

The cells are divided in 12-cell groups of two parallel-connected cells, which are series-connected to compose the battery cell pack. We have chosen cells with a capacity of 2.5 A h to be connected in parallel, instead of cells of 5 A h, because it is almost the limit of the cells based on a cylindrical 18650 case, which is the less expensive choice. Anyway, the group composed of two parallel-connected cells is equivalent to a single cell with a double capacity respect to the external effects [4], so in the following work we have considered a battery cell pack composed of 12 series-connected cells with a

capacity of $5\,\mathrm{A\,h}$. A photograph of the used cell pack is shown in Figure 6.1.

The battery is provided with a BMS that manages the cells to optimize the usage of a battery. The BMS is equipped with a power switch which controls the battery parallelization avoiding the flowing of an unsafe current from the most charged battery to the other one. This problem has been explained in detail in Section 3.1, where a parallelization algorithm has been proposed to control the parallelization and maximize the total energy which the batteries can provide to the load. This algorithm is not implemented in the BMS but into the tool control system. It can control the activity of a BMS power switch through some apposite commands. At the same time, the BMS can open the switch to protect the cells in unsafe conditions, increasing the efficiency of the protection control system.

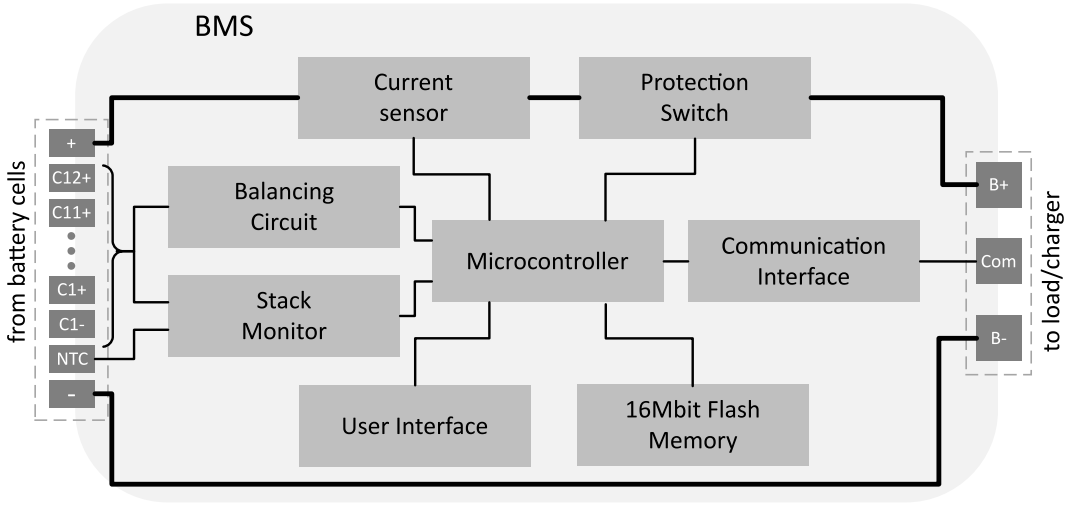

Figure 6.2: *Block diagram of the Battery Management System (BMS).*

The BMS block diagram is shown in Figure 6.2, where we can note the described power switch block and the communication interface which is used by the tool control system to acquire the state of the battery and to send the needed commands. The BMS block diagram is very similar to the one of the MMU presented in Section 4.1.1. In fact, it is based on the same microcontroller (LPC1754) and communication interface (CAN-bus) and uses the same dedicate stack monitor (LTC6803-3) to measure the voltage and temperature of the cells. In this case, only two points of temperature into the battery cell pack are acquired because cabling one temperature sensor for each cell is too expensive. For the same reason, the active balancing circuit has been replaced with a passive technique which balances the energy stored in the cells dissipating on some bleeding resistances the excessive energy quantity of the most charged cells, and to maximize the storable energy in the battery. The microcontroller can connect these resistances in parallel to the cells, through the LTC6803-3, which is provided with a dedicated switch for each cell.

The BMS is equipped with a current sensor based on a shunt resistor which generates a voltage drop proportional to the current, amplified by a bidirectional current-sense amplifiers with a voltage output (MAX4081). The output voltage, properly filtered, is read by the microcontroller that converts it into the battery current information. The BMS is also provided with a 16Mbit flash memory, where the microcontroller can

store all the measured and the estimated quantities, and with a simple user interface that consists of a push button to enable the visualization of the battery SOC and some LEDs, with which this information is encoded.

We can note that the designed hardware can be easily adopted to manage a battery with nominal voltage of 36 V and then composed of 10 series-connected cells. This is possible thanks to the flexibility of the dedicate chip monitor which can monitor from 4 to 12 series-connected cells.

The firmware of the microcontroller is based on the FreeRTOS operating system and is divided in tasks with which the functionalities of the BMS have been implemented. The main task controls the activation of the switch, in according to the command received from the CAN-bus, and manages the measurement of the cell voltage and the battery temperature and current. It is the most important task and has the highest priority. This task shares the acquired quantities with the other tasks, such as the memory control task that stores this information in the memory. When the load or the charger requires this information, the task reads from the memory and sends them to the CAN-bus. The CAN-bus interface is managed by the relative task that receives and executes the command and sends the measured quantities and the battery status.

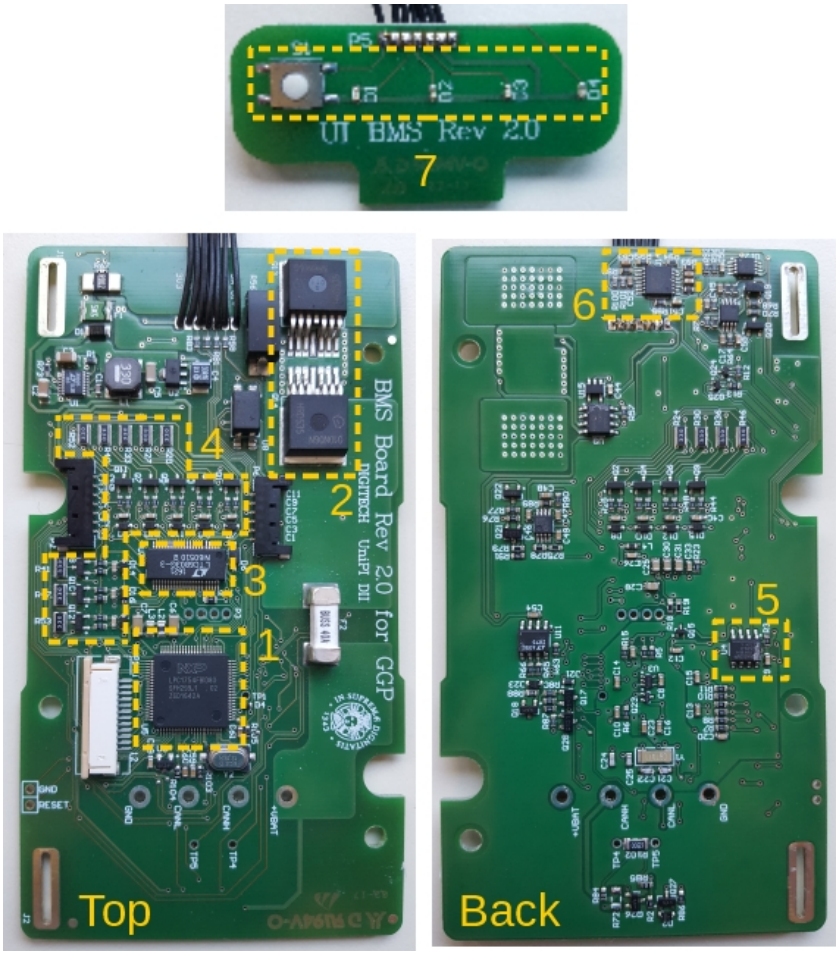

Figure 6.3: *Photograph of the implemented BMS. The main blocks are: 1. microcontroller, 2. protection switch, 3. stack monitor, 4. Balancing circuit, and 5. flash memory, 6. current sensor front-end, 7. user Interface.*

The BMS has been realized on a two layers PCB and Figure 6.3 shows its photo where the most important components have been highlighted. A photo of the assembled smart battery is reported in Figure 6.4.

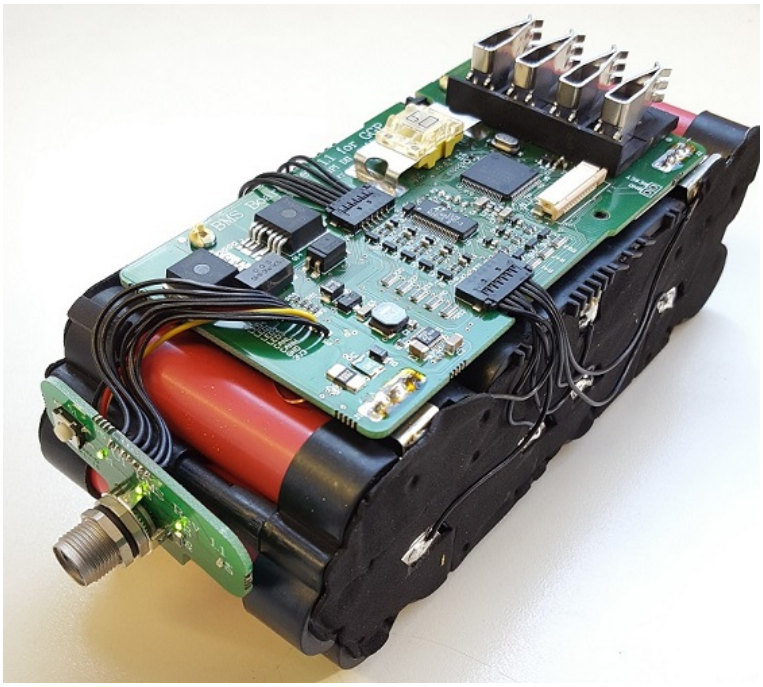

Figure 6.4: *Photograph of assembled battery.*

6.2 Case study Lawnmower dual batteries

The standard battery has been used to power an innovative gardening tools line developed in a collaboration project between the University of Pisa and the Global Gardening Product (GGP), which is the European leader in the production and distribution of lawnmowers and powered garden equipment. The aim of the project is the development of an electronic control unit (ECU) that can manage a large battery gardening tool family, equipped with a remote control interface which allows the user to control the behavior of the tools and to check the battery status.

The gardening tool family is based on the presented idea of using one or more standard batteries parallel-connected to power the tools. For this reason, the ECU must be able to manage the parallel-connection of the battery. These concepts are demonstrated through the design and the realization of a lawnmower powered by a dual battery system, analyzing the effective benefits of this technique on the battery life.

6.2.1 The innovative lawnmower

The mechanical parts of a commercial lawnmower have been used to develop the innovative lawnmower. It is equipped with the custom ECU, which is developed to control brushless and brushed motors. In this way, the same system can be used in a large family of tools with different types of motor and control strategies. Moreover, the ECU

allows the remote monitor/control of the tool by making it available to the user according to the IoT scenario. The tool system architecture is shown in Figure 6.5.

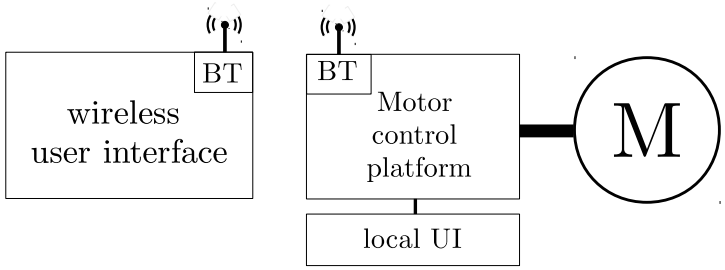

Figure 6.5: *Block diagram of the remotely controlled motor driver platform application.*

The ECU is based on a microcontroller and a Bluetooth interface that lead to a good trade-off between flexibility, performance and cost. The microcontroller must be able to manage in a safe mode the parallel-connection of the batteries using the algorithm presented in Section 3.1. For this reason, the ECU has been provided with a CAN-bus interface with which the microcontroller can communicate with the batteries and sends the commands to activate the battery power switch. The block diagram of the developed ECU is shown in the Figure 6.6.

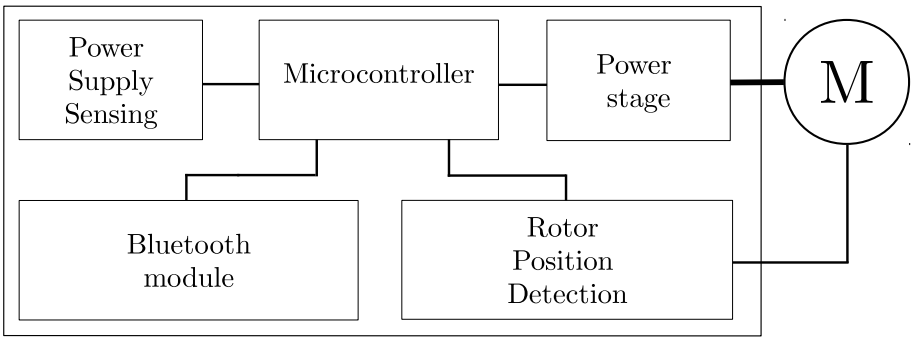

Figure 6.6: *Motor control platform block diagram.*

In addition to the microcontroller and the communication interface blocks, we can note the power stage, the rotor position detection and the Bluetooth blocks. The first one receives the control signals coming from the microcontroller and consequently supplies the motor windings. It is composed of a N-MOS three-phase inverter, managed by the gate driver DVR8301 manufactured by Texas Instrument. This chip drives the MOSFETs of the inverter and preserves the system integrity in case of malfunctions, with a built-in protection system. The rotor position detector is a circuit block able to read the most common position sensor used in a motor, such as encoders or hall sensors.

This is essential to control in a correct way the brushless motor, because the control signals must be closely dependent on the rotor position, otherwise the motor does not work. In some cases, the brushless motor is not equipped with the position rotor sensor to reduce its cost and that of wiring. Therefore, rotor position block is equipped with an auxiliary circuit to understand the rotor position of a brushless motor, starting from the phase voltages. It is based on the zero crossing detection technique, described in [102],

in which the zero crossing point of the back electromotive force (BEMF) induced on the stator coil when it is not powered is detected.

Instead, the rotor position sensor is only needed to measure the rotor speed in a brushed motor. In fact, this type of motor is usually easier to control, because it starts to work when a power source is applied to its terminals and the rotor speed can be controlled by changing the supply current.

The module BGM111, manufactured by Silicon Labs, is the base of the Bluetooth block and establishes a point-to-point communication link between the board and the external user interface. It is a Bluetooth low-energy module and uses Bluetooth Smart, a new type of protocol that presents some differences compared to the classic Bluetooth. In particular, it is designed for intermittent transfers of data to reduce the module power consumption. The remote interface can be developed for any device provided with the Smart Bluetooth protocol, such as any smartphone, tablet and laptop. The use of the interface on a portable device brings many advantages. In fact, it can be used for the online visualization of useful information, such as the instant speed of the motor and its power consumption, by using graphical indicators. Moreover, since these gardening tools are equipped with smart batteries, the UI is also capable of showing the state of the battery, in terms of voltage, current and residual charge. This aspect is very interesting because it allows the user to optimize the battery usage as a function of the remaining work to do.

The described ECU has been realized with a double-layer PCB, as shown in Figure 6.7, where the presented block are highlighted.

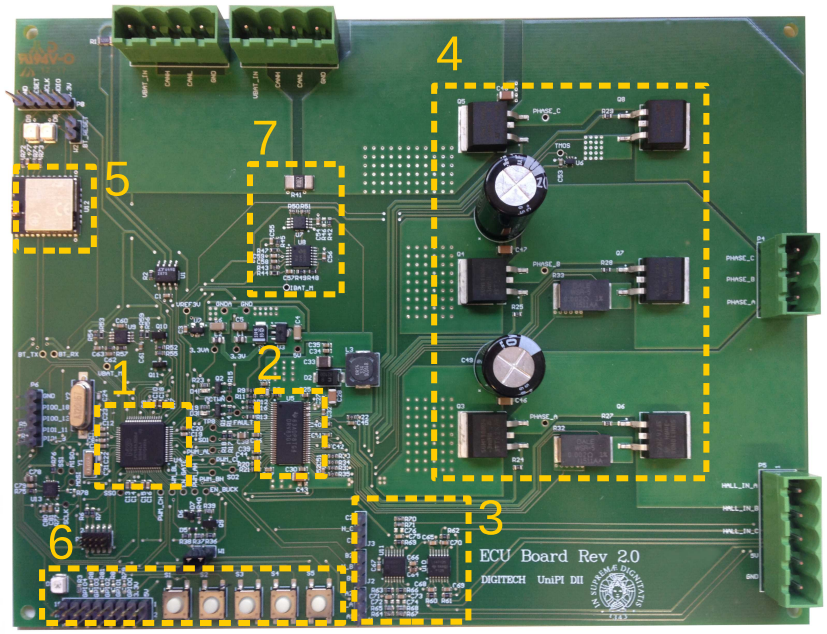

Figure 6.7: *Photograph of the implemented platform. The main blocks are: 1. Main unit, 2. Gate Driver, 3. Rotor Position Detection, 4. Inverter, and 5. Bluetooth module, 6. local user interface, 7. sensing block.*

6.2.2 Experimental setup

The realized ECU is assembled in the lawnmower equipped with two slots needed to connect the batteries and shown in Figure 6.8. The figure shows the experimental setup composed of a dual battery lawnmower and a laptop on which a user interface is running.

Figure 6.8: *Photograph of the lawnmower experiential setup.*

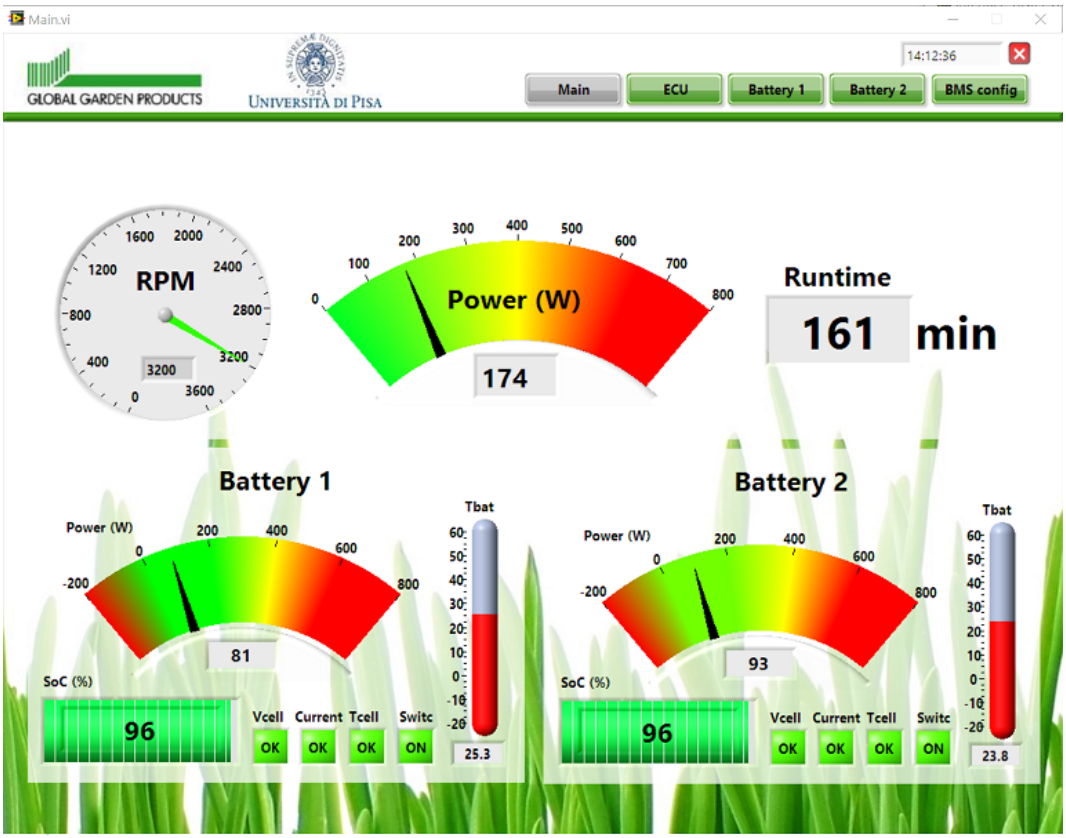

Figure 6.9: *Screenshot of the Main tab of the lawnmower User Interface developed in LabVIEW.*

A LabVIEW interface has been developed to control the system, to show the information coming from the ECU and to save these data for an offline analysis. The main tab is shown in Figure 6.9 and visualizes the lawnmower information (motor speed, absorbed electric power and residual run-time) and the status of the two connected batteries.

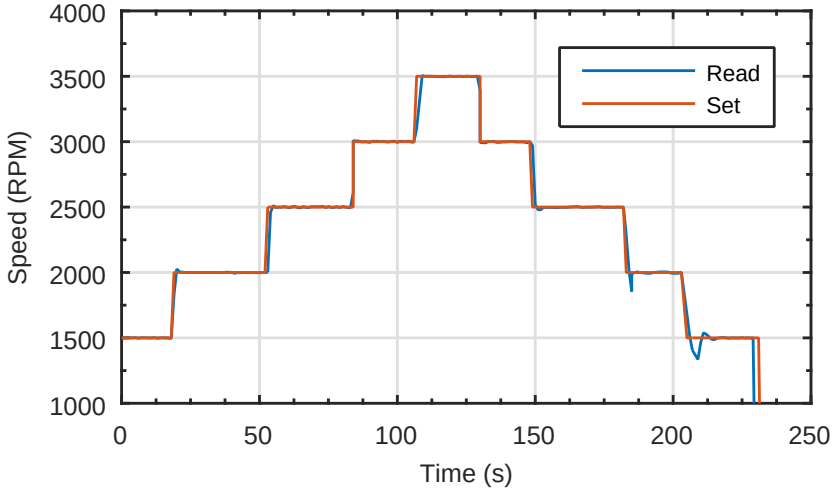

Figure 6.10: *Comparison between the read and set speeds acquired on the lawnmower.*

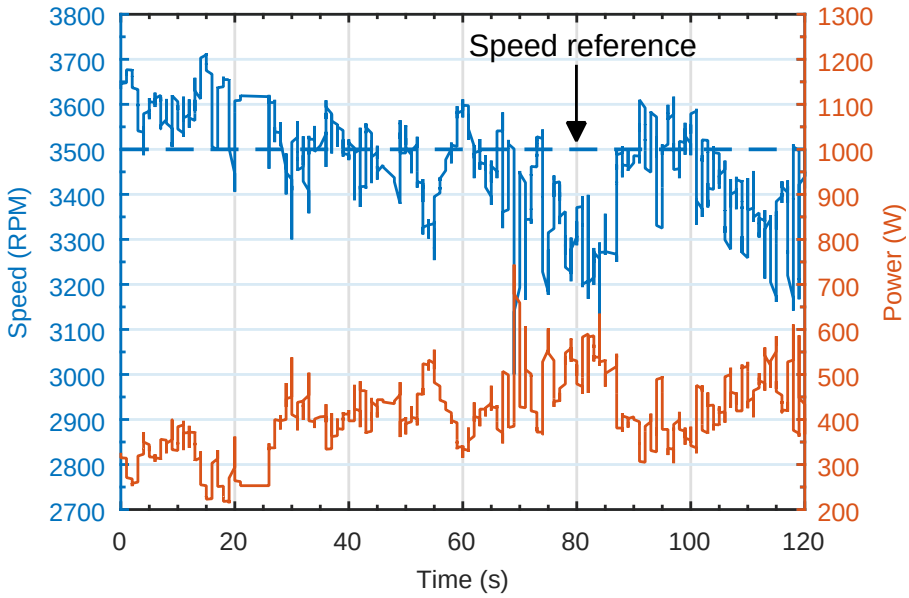

Figure 6.11: *Motor speed and instant power consumption of the lawnmower at work.*

The interface allows the user to dynamically change the motor speed adapting the lawnmower to the grass load. In Figure 6.10, we have shown the set speed and the measured one acquired in a specific test. The two speed values present a noticeable difference in the transients when the lawnmower motor speed is asked to step down. This is ascribed to the slow down policy implemented in the controller, which reduces the power provided to the motor without applying any breaking procedure. The large

inertia of the cutting blade attached to the motor free wheeling does not allow the speed to quickly slow down and to reach the set value.

Figure 6.11 shows the speed variations of the lawnmower motor during two minutes of grass-cutting. The speed is set to the reference value of $3500\,\mathrm{rpm}$, but the instantaneous speed of the motor changes because of the variable resistance offered by the grass. The controller counteracts these variations by changing the power provided to the motor: when the speed decreases the controller gives more power to the motor and vice versa.

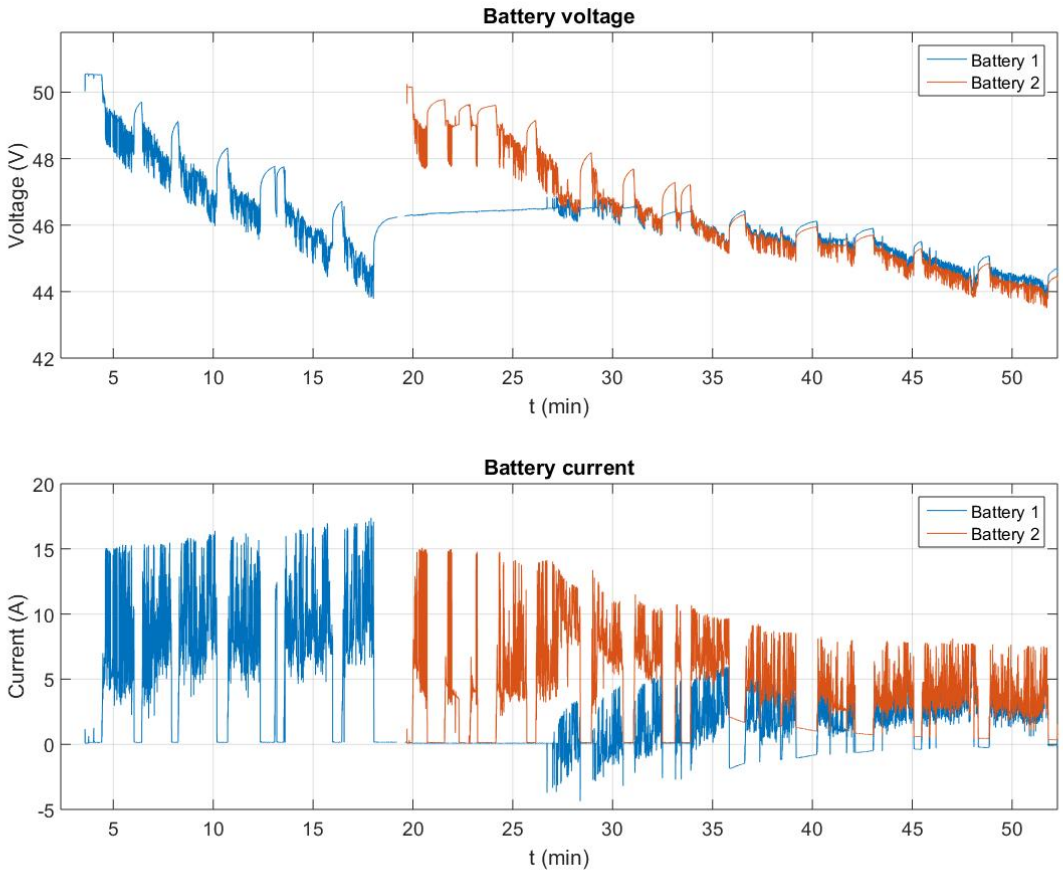

Figure 6.12: *Current and voltage of two battery in a parallelization test on the lawnmower at work.*

During a grass-cutting, the parallelization algorithm presented in details in Section 3.1 and implemented on the microcontroller of the lawnmower ECU has been tested. Figure 6.12 shows the results of this test starting from two fully charged batteries. The test starts with the insertion of battery 1 into the tool battery slot. Detecting only one battery, the parallelization algorithm connects it to the load and the operator starts the grass-cutting test. After about $20\,\mathrm{min}$ the second battery is inserted into the second tool battery slot. The parallelization algorithm notices the event and connects this battery to the load disconnecting battery 1. This happens because the second battery is more charged than the first one and their states are not compatible to be connected in parallel. As soon as the difference of the battery voltage becomes less than ΔV, defined in

the Eq.(3.2), the batteries can be parallel-connected. Thus, the algorithm sends the command to close the protection switch of battery 1, and the two batteries are parallel-connected. We can note that the currents of the two batteries are not balanced in the minutes after the parallelization because their SOCs are not the same. However, the mean current of battery 2 decreases because when the load requires more power, battery 1 helps it, otherwise battery 2 recharges battery 1, when the load requires little power. This process is interrupted, disconnecting battery 1, when the load power reaches 0 and the recharging current of battery 1 becomes higher than that allowed by the cell. After some minutes, this process balances the SOC of the batteries and the load current is equally divided between them. This effect reduces the cell stress, increasing the application run-time and reducing the cell temperature.

6.3 Smart charger

With the introduction of the standard batteries to power the tools, the user needs to recharge and control a large number of batteries. Classic chargers are able to charge a single battery at one time and so present many limitations. Usually, users buy only one charger for more batteries in order to keep the cost of the tools low. At the same time, the manufacturer cannot propose to sell each battery with the relative charger, otherwise the cost benefit of using standard batteries is erased or the system becomes even unsuitable. For this reason, the user must recharge the batteries one by one, ma-

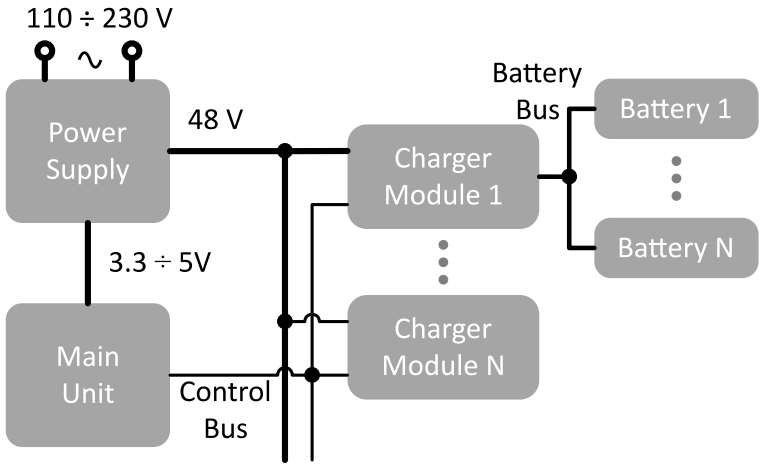

Figure 6.13: *Block diagram of the smart charger.*

king this process very uncomfortable and time-consuming, leading the user to forget some batteries discharged and not usable in the next work. Moreover, the batteries that are forgotten discharged for a long time can be damaged by the under-discharge effect which, in the best case, can reduce its capacity. In the worst cases, this effect can produce dendrites in the cell which can perforate the separator generating unsafe situations and making the cell and the battery unusable. This problem can be resolved developing a charger capable to manage a lot of standard batteries, which presents a cost comparable to the classic one. This is possible because the batteries can be connected at the same power bus in a safe mode thanks to the battery power switch. The charger can control the recharge phase of each battery activating in a smart way their

switches. Using this concept, a smart charger, capable of recharging and managing more batteries, has been designed.

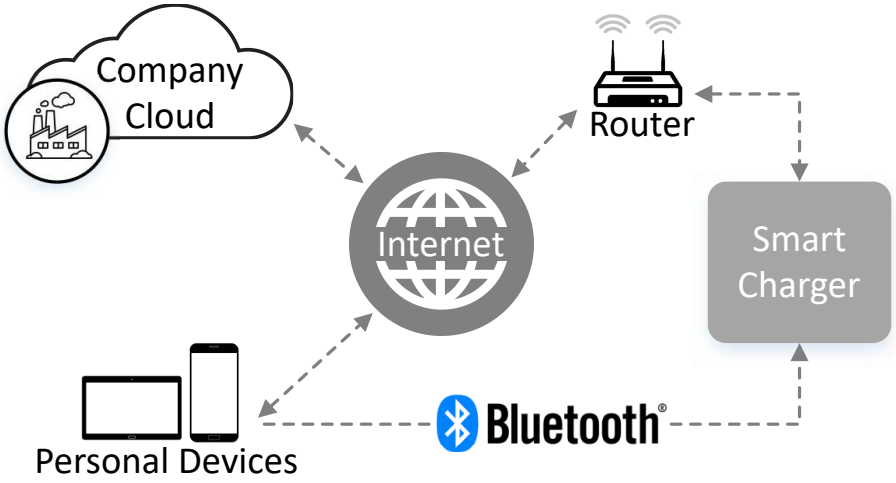

Figure 6.14: *Connection block diagram of the charger in the IoT scenario.*

It is based on a modular design, as shown in Figure 6.13, to make the architecture very flexible. Therefore, the system can be considered like a series of independent modules which can be connected together to implement the desired functionalities. The most important module is the main unit that manages all the other blocks and the general behavior of the charger. The main unit is equipped with a Wi-Fi module that implements the IoT paradigm making the charger controllable by the user through a remote interface on personal portable devices. This module allows the charger to be connected to a company cloud that stores the battery information and reads the configuration of the charging phases, as shown in Figure 6.14. The battery information is very useful for the user, but also for the manufacturer, because it can analyze the data of all the users and obtain statistical information, used for example to forecast potential development problems or to optimize the design of new devices. To configure the Wi-Fi module with the network information, this block is equipped with a Bluetooth module, which can be connected point-to-point to the remote interface, providing an easy communication channel between the user and the charger.

The power supply module provides all the Direct Current (DC) supply needed by the other blocks. It is pictured as a single block in the diagram, but it can be composed of one or more modules that the user can buy and connect to the charger to obtain all the needed power.

The battery charging profile is generated by the charger module which is controlled by the main unit and that manages the charging phase of the batteries. The charger module can be configured to provide a classic CC/CV profile with different constant current and voltage values, but also to generate a custom profile.

This functionality is very interesting in a smart charge because it can generate some diagnostic profiles with which the charger control unit can estimate the battery internal state, such as the battery resistance and capacity that are closely related to the SOH.

In fact, many online SOH estimation techniques are based on the data which are acquired in the charging phases, for example in [23,42,57] the authors use the charging voltage curve to apply the incremental capacity analysis. This technique relates the cell

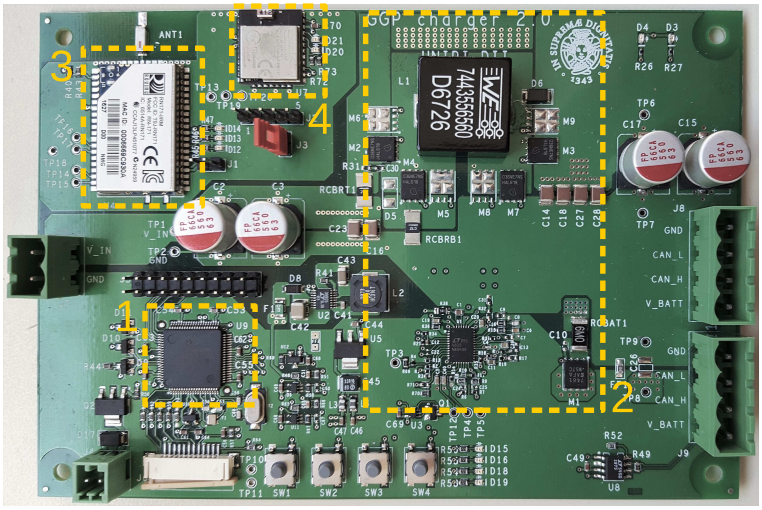

Figure 6.15: *Photograph of the electronic control board of the implemented smart charger. The main blocks are: 1. Microcontroller, 2. Charger module, 3. Wi-Fi module, and 4. Bluetooth module.*

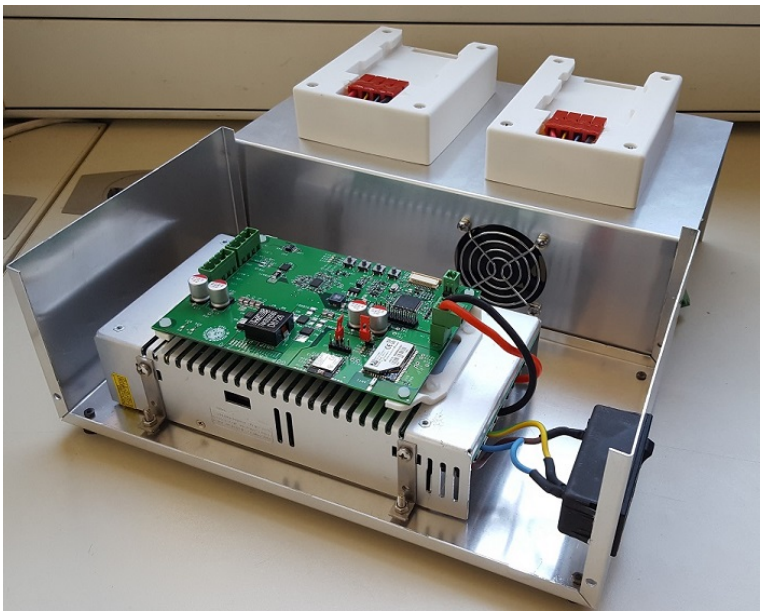

Figure 6.16: *Photograph of the assembled charger (the case has been opened to show the AC/DC converter and the electronic board).*

capacity to the one of the charge with respect to the cell voltage (dQ/dV – V curves) of the charging phase. A similar technique has been applied in [97] to estimate the capacity of the cells assembled in a battery pack. Instead, the relation between the duration of the CV charging phase and the SOH of a cell has been demonstrated in [99].

Another smart profile can be the fast charging, which the user can select to quickly recharge a fully discharged battery, allowing him to finish an uncompleted work. On the contrary, slow or maintenance profiles can be selected to preserve the battery lifetime if the user is sure that the batteries are remaining unused for a long time. Regarding

this, the charger can memorize all the user's batteries and can alert the user, through the remote interface, if a battery is not connected to it for a long period. This can avoid battery under-discharge situations caused by the user that forgets to recharge a battery after its usage.

6.3.1 Charger implementation

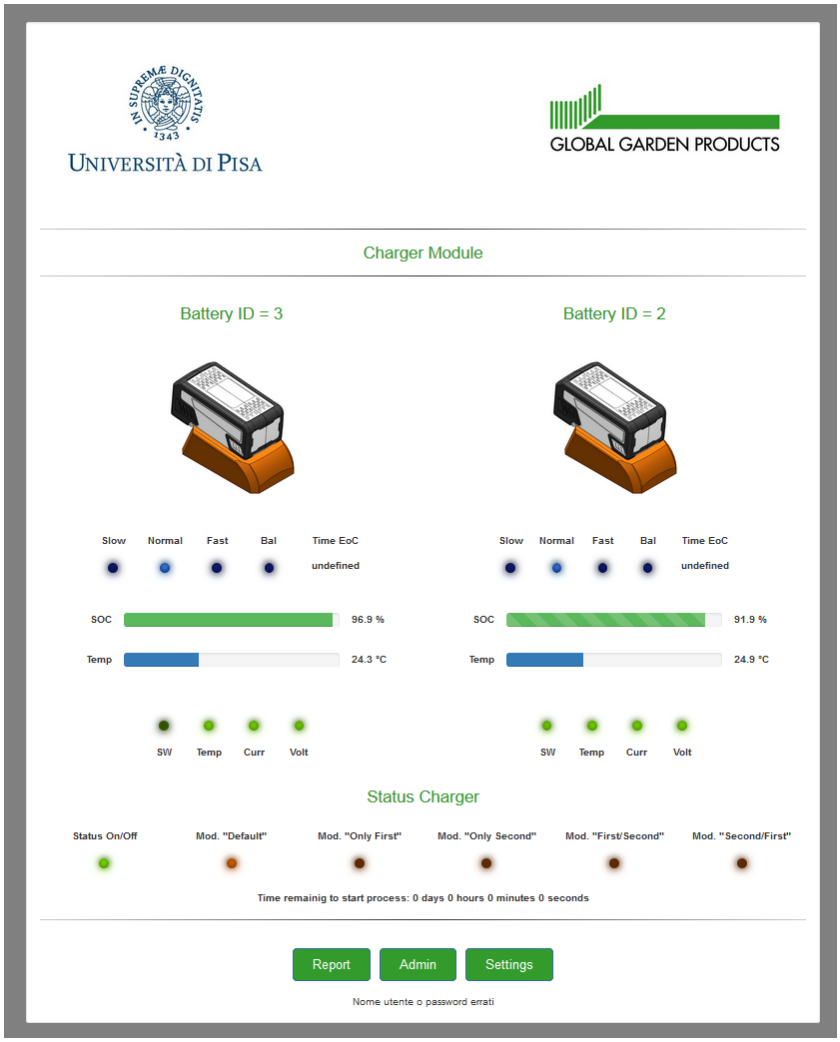

Figure 6.17: *Screenshot of the Main tab of the charger User Interface.*

An experimental version of the presented architecture has been implemented on the board shown in Figure 6.15, in which we have developed the control unit and one charger module. The main unit is based on a microcontroller LPC1754 by NXP, which manages the charger module and is equipped with the CAN-bus interface to communicate with the batteries. The microcontroller manages also the Wi-Fi module, which is based on the Wireless LAN Module RN171, manufactured by Microchip. This module is very simple to configure and use because it can be controlled through a list of commands sent via a UART interface. Moreover, the microcontroller manages the Bluetooth low energy module BGM111 by Silicon Labs with which it can establish a

point-to-point communication link with a device application. The communication link can be used to configure the network information by the user.

The charger module is based on the LTC4020, manufactured by Linear Technology: a specific charger chip that controls a Buck-Boost DC/DC converter to charge batteries with higher and lower voltage than the input one. This chip can control a charging phase following a CC/CV profile, where the constant current and voltage can be changed by two analog pins. The chip is also provided with the possibility to implement a trickle charging phase, which consists of a very low charging current that is applied to a fully discharged battery to increase its SOC [66, 68]. This phase is maintained until the battery SOC reaches a default value (about $20\,\%$) because in the literature it has been demonstrated that reducing the stress of a battery with low SOC can considerably increase its life time. In this chip, the switching condition between the trickle charging and the CC phase is configured to be verified when the battery voltage reaches a certain level, read through an analog input signal. The microcontroller can generate a different custom charging profile controlling opportunely the three configuration pins and the enabling of the LTC4020 chip. The board is provided with two equivalent battery connectors, which have the pins connected to the same signals. For this reason, we can easily increase the connectors number and then the number of the battery slots.

Figure 6.18: *Photograph of the charger experiential setup.*

The presented board has been assembled with a commercial $500\,\mathrm{W}$, $48\,\mathrm{V}$ AC/DC converter, which has been chosen to avoid problems with the high voltage rules. As shown in Figure 6.16, they are mounted in the case, over which two battery slots are fixed.

An HTML remote control interface has been developed and uploaded into an Apache HTTP Server installed on a Raspberry board. The interface is controlled by a JavaScript code that accesses a database, where it reads the information to display into the interface and writes the user commands to configure the charger. On the Raspberry, there is also a python script that implements a TCP-IP server which is used by the charger to establish a Wi-Fi connection to send and receive information. The python script

manages the communication with the charger and the database data. Moreover, this script stores the information of the batteries into log files, which can be downloaded from the remote interface.

Figure 6.17 shows the main page of the remote interface, where the most important information items of the two connected batteries are reported.

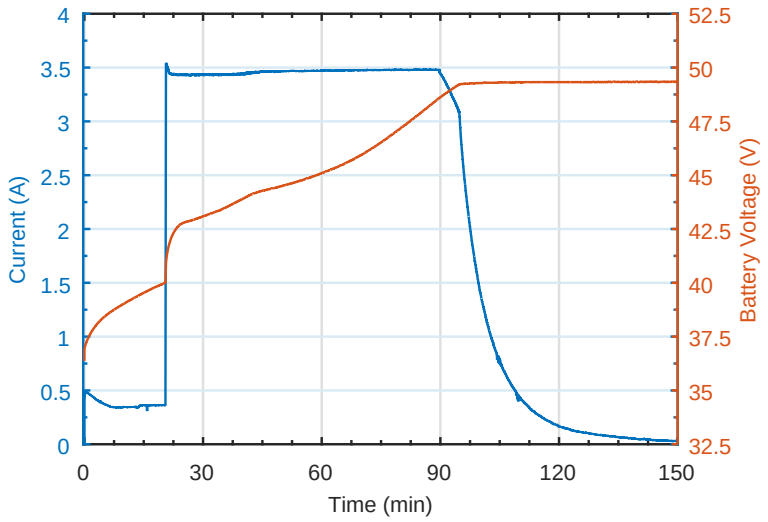

Figure 6.19: *Complete CC/CV charging profile of the smart charger.*

6.3.2 Experimental results

The presented charger has been tested using the experimental setup shown in Figure 6.18. In the figure, we can note, in addition to the charger, a raspberry and a router which are used to emulate the company cloud and a personal device with the user interface that controls the system.

Figure 6.19 shows the battery voltage and current of a charging test in which the charger module has been configured to execute the trickle, CC, and CV phases, with $40\,\mathrm{V}$, $3.5\,\mathrm{A}$ and $49\,\mathrm{V}$ as trickle voltage threshold, CC current and CV voltage, respectively.

CHAPTER 7

Conclusion

The goal of the activity carried out during the Ph.D. course and described in the present thesis was the study of a novel methodology to design smart battery systems for medium and high-power applications. We have analyzed the literature on the electrochemical storage technology identifying the lithium-ion chemistry as the most promising solution for this kind of batteries. The weak point of the technology is that any lithium-ion battery must be accompanied by an electronic control system, the Battery Management System, that provides the monitoring and safety functions necessary for a controlled and safe use of the battery. The functions required for a BMS has been studied, as well as the most common architectural solutions. They have been improved to obtain new approaches that apply to the design of a battery with innovative functions and characteristics. The development of the battery has been possible thanks to the development of simulation platforms, based on a software and hardware in the loop approaches, which allowed us to study the classic solutions, develop new ones, and compare them, to evaluate the best trade off with respect to the considered application. In particular, a proper software platform has been used to demonstrate the benefits of a smart parallel-connection of two or more batteries and the improvements in the reduction of the battery stress achieved by this approach. For example, considering two parallel-connected batteries, the load current is shared between them, so the current that flows in the single one is about one half of the total current. This is true if the batteries show the same internal state. Otherwise the parallel-connection is impractical or even dangerous because of the recirculation current.

Indeed, the very low resistances of the batteries allow a very high current to flow from the most charged battery to the other one if their voltages are not compatible. Therefore, the developed platform allows us to define hardware and software guidelines to keep the system in the safe states. Moreover, the best hardware architecture

and software-implemented parallelization algorithm have been found to maximize the global battery performance and to smartly control the parallelization.

Other realizations regard two platforms, based on the hardware in the loop approach, that have been implemented to verify the performance of complex estimation algorithms and to perform end of line testing of a battery management system for medium-power applications. The first platform emulates the battery response of an electric vehicle that is running one of several standard driving cycles and provides the voltage, current, and temperature of each battery cell. These data are used as input for the BMS, implemented in an FPGA device, in which some complex algorithms to estimate the internal state of the cell run. These model-based hardware-accelerated algorithms provides accurate estimates of the battery cell SOC, by also identifying the parameters of the cell equivalent circuit model and tracking their variations as a function of the battery operating conditions and aging. This innovative solution is very appealing because the FPGA provides a hardware acceleration that reduces the run time of the algorithms and allows the time multiplexing of the same hardware module among many cells. The goal achieved is that a complex and innovative BMS for batteries with hundreds of cells may be realized with a simple low-cost FPGA based electronic board. The second platform has been designed to perform the end of line testing of a BMS for up to 12 cells. The main feature of the realization is the low cost that allows the manufacturer to carry out this kind of test on the produced devices for low production volumes and small investments. The modular approach to compose a battery system is one of the most important methodologies studied in this work, as standardization is one of the most promising means to keep low the development cost of a battery. A $12\,\mathrm{V}$ standard module has been proposed in this work as the basic unit with which a larger battery is formed. The module is designed to be compatible with a standard $12\,\mathrm{V}$ lead acid battery, simplifying the replacement of this chemistry with a lithium-ion one. This is very interesting from an industrial point of view, because the lead acid technology has been the most used for the battery in first generation electric vehicles. Therefore, there is an increased interest for the vehicle refitting, in which the old battery is exhausted and must be replaced with a new technology one. In particular, the standard module and the fast charger concepts have been applied to the design of a new battery for an electric minibus originally equipped with a $72\,\mathrm{V}$ lead acid battery. The fast charge concept is another important methodology that exploit the high charging power of the lithium-ion technology and some specific characteristic of the application to reduce the size of the battery.

The sizing of the system in terms of battery capacity, charging power, and distance between two recharge stations gives rise to a multi-dimensional optimization problem where the system cost is the optimization function and the constraints of the problem parameters are usually derived by heuristics analysis. For this reason, only generic considerations can be drawn by resolving this problem. At the same time, the implementation details may lead to a significant impact on the aforementioned constraints, so we have developed an experimental demonstrator using reasonable parameters to obtain experimental data with which we can deduce some realistic constraints. Therefore, we have proven that a small battery with a capacity of only $240\,\mathrm{A\,h}$ can supply a public transportation minibus for an ideally infinite time if it is recharged for about 1 minute (with the maximum allowed power) each routed kilometer, and with the maxi-

mum distance of about $40\,\mathrm{km}$ between two consecutive recharge stations.

This is a very promising result because it is compatible with the normal bus operation, as this time is comparable to that needed for boarding and alighting of the passengers.

Moreover, a future analysis of the experimental data can be used to find some guidelines to improve the development of the battery bus service and to increase the spread of electric vehicles on the market.

The modular design approach developed in this work has also been applied to the battery system for medium-power applications, such as gardening and power tools. Therefore, a standard battery with a nominal voltage of $48\,\mathrm{V}$ and a capacity of $5\,\mathrm{A\,h}$ has been defined with innovative features. It can be parallel-connected with other similar ones only when the inner states of the batteries are compatible with a safe connection, making a smart battery system. This possibility increases the number of applications that can be powered by the same battery system. In fact, a battery system composed of n standard batteries parallel-connected can provide an energy and a power about n times greater than a single battery, increasing the number of application that can be powered by it. To demonstrate this design methodology a dual battery lawnmower has been developed and the proposed parallelization algorithm has been tested. As shown in the discussion of the experimental results, the parallelization approach duplicates the application runtime, increasing its usability, but it also halves the current that flows in each battery. This effect in very useful to increase the battery time life because it decreases the stress due to the current level and the cell temperature due to the dissipated power. In fact, the reduced current decreases the energy dissipated in the cell, and thus the temperature. In conclusion, we have presented innovative design methodologies of the electronic circuits necessary to control an electrochemical storage system based on lithium-ion cells, analyzed its benefits with simulative and hardware in the loop approaches, and demonstrated its applicability with some case studies, in which the batteries were applied in real applications obtaining innovative results and new features that advances the knowledge in both the scientific and industrial points of view.

Bibliography

[1] IEEE Guide for the Characterization and Evaluation of Lithium-Based Batteries in Stationary Applications. *IEEE Std 1679.1-2017*, pages 1–47, Dec 2018.

[2] Mohamed Abdel Monem, Khiem Trad, Noshin Omar, Omar Hegazy, Bart Mantels, Grietus Mulder, Peter Van den Bossche, and Joeri Van Mierlo. Lithium-ion batteries: Evaluation study of different charging methodologies based on aging process. *Applied Energy*, 152:143–155, Aug 2015.

[3] Mohamed Abdel-Monem, Khiem Trad, Noshin Omar, Omar Hegazy, Peter Van den Bossche, and Joeri Van Mierlo. Influence analysis of static and dynamic fast-charging current profiles on ageing performance of commercial lithium-ion batteries. *Energy*, 120:179–191, Feb 2017.

[4] Fuqiang An, Jun Huang, Chengyu Wang, Zhe Li, Jianbo Zhang, Sean Wang, and Ping Li. Cell sorting for parallel lithium-ion battery systems: Evaluation based on an electric circuit model. *Journal of Energy Storage*, 6:195–203, May 2016.

[5] David Anseán, Manuela González, Juan Carlos Viera, Juan Carlos Álvarez, Cecilio Blanco, and Victor Manuel García. Electric Vehicle Li-Ion Battery Evaluation Based on Internal Resistance Analysis. *2014 IEEE Vehicle Power and Propulsion Conference (VPPC)*, pages 1–6, Oct 2014.

[6] David Anseán, Juan Carlos Viera, Manuela González, Víctor Manuel García, Juan Carlos Álvarez, and José Luis Antuña. High power LiFePO4 cell evaluation: Fast charge, depth of discharge and fast discharge dependency. *World Electric Vehicle Journal*, 6(3):653–662, Nov 2013.

[7] Ines Baccouche, Asma Mlayah, Sabeur Jemmali, Bilal Manai, and Najoua Essoukri Ben Amara. $implementation of a Coulomb counting algorithm for SOC estimation of Li-Ion battery for multimedia applications. In *12th International Multi-Conference on Systems, Signals and Devices, SSD 2015*, pages 1–6. IEEE, Mar 2015.

[8] Bharat Balagopal and Mo Yuen Chow. The state of the art approaches to estimate the state of health (SOH) and state of function (SOF) of lithium Ion batteries. In *Proceeding - 2015 IEEE International Conference on Industrial Informatics, INDIN 2015*, pages 1302–1307. IEEE, Jul 2015.

[9] F. Baronti, R. Di Rienzo, R. Moras, R. Roncella, R. Saletti, G. Pede, and F. Vellucci. Implementation of the fast charging concept for electric local public transport: The case-study of a minibus. In *Proceeding - 2015 IEEE International Conference on Industrial Informatics, INDIN 2015*, pages 1284–1289. IEEE, Jul 2015.

[10] F. Baronti, G. Fantechi, E. Leonardi, R. Roncella, and R. Saletti. Effective modeling of temperature effects on lithium polymer cells. *2010 17th IEEE Int. Conf. Electron. Circuits Syst.*, pages 990–993, Dec 2010.

[11] F Baronti, G Fantechi, E Leonardi, R Roncella, and R Saletti. Enhanced model for Lithium-Polymer cells including temperature effects. In *IECON 2010 - 36th Annu. Conf. IEEE Ind. Electron. Soc.*, pages 2329–2333. IEEE, Nov 2010.

[12] F. Baronti, G. Fantechi, E. Leonardi, R. Roncella, and R. Saletti. Hierarchical platform for monitoring, managing and charge balancing of LiPo batteries. In *2011 IEEE Vehicle Power and Propulsion Conference, VPPC 2011*, pages 1–6. IEEE, Sep 2011.

[13] F. Baronti, G. Fantechi, R. Roncella, R. Saletti, G. Pede, and F. Vellucci. Design of the battery management system of LiFePO4 batteries for electric off-road vehicles. In *IEEE International Symposium on Industrial Electronics*, pages 1–6. IEEE, May 2013.

[14] F. Baronti, W. Zamboni, N. Femia, H. Rahimi-Eichi, R. Roncella, S. Rosi, R. Saletti, and M.-Y. Chow. Parameter identification of Li-Po batteries in electric vehicles: A comparative study. In *2013 IEEE Int. Symp. Ind. Electron.*, pages 1–7. IEEE, May 2013.

[15] Federico Baronti, Cinzia Bernardeschi, Luca Cassano, Andrea Domenici, Roberto Roncella, and Roberto Saletti. Design and Safety Verification of a Distributed Charge Equalizer for Modular Li-Ion Batteries. *IEEE Trans. Ind. Informatics*, 10(2):1003–1011, May 2014.

[16] Federico Baronti, Roberto Di Rienzo, Nicola Papazafiropulos, Roberto Roncella, and Roberto Saletti. Investigation of series-parallel connections of multi-module batteries for electrified vehicles. In *2014 IEEE International Electric Vehicle Conference, IEVC 2014*, pages 1–7. IEEE, Dec 2014.

[17] Federico Baronti, Gabriele Fantechi, Roberto Roncella, and Roberto Saletti. Intelligent cell gauge for a hierarchical battery management system. In *2012 IEEE Transportation Electrification Conference and Expo, ITEC 2012*, pages 1–5, Dearborn, Jun 2012. IEEE.

[18] Federico Baronti, Gabriele Fantechi, Roberto Roncella, Roberto Saletti, and Pierangelo Terreni. Hardware building blocks of a hierarchical battery management system for a fuel cell HEV. In *IECON 2012 - 38th Annu. Conf. IEEE Ind. Electron. Soc.*, pages 4041–4047. IEEE, Dec 2012.

[19] Federico Baronti, Roberto Roncella, Roberto Saletti, and Walter Zamboni. FPGA implementation of the mix algorithm for state-of-charge estimation of Lithium-ion batteries. In *IECON Proceedings (Industrial Electronics Conference)*, pages 5641–5646. IEEE, Oct 2014.

[20] Jorge Varela Barreras, Christian Fleischer, Andreas Elkjaer Christensen, Maciej Swierczynski, Erik Schaltz, Soren Juhl Andreasen, and Dirk Uwe Sauer. An Advanced HIL Simulation Battery Model for Battery Management System Testing. In *IEEE Transactions on Industry Applications*, volume 52, pages 5086–5099, Nov 2016.

[21] Andrew C. Baughman and Mehdi Ferdowsi. Double-tiered switched-capacitor battery charge equalization technique. *IEEE Transactions on Industrial Electronics*, 55(6):2277–2285, Jun 2008.

[22] Thorsten Baumhöfer, Manuel Brühl, Susanne Rothgang, and Dirk Uwe Sauer. Production caused variation in capacity aging trend and correlation to initial cell performance. *Journal of Power Sources*, 247:332–338, Feb 2014.

[23] Maitane Berecibar, Floris Devriendt, Matthieu Dubarry, Igor Villarreal, Noshin Omar, Wouter Verbeke, and Joeri Van Mierlo. Online state of health estimation on NMC cells based on predictive analytics. *Journal of Power Sources*, 320:239–250, Jul 2016.

[24] Martin Brand, Simon Glaser, Jan Geder, Stefan Menacher, Sebastian Obpacher, Andreas Jossen, and Daniel Quinger. Electrical safety of commercial Li-ion cells based on NMC and NCA technology compared to LFP technology. *World Electric Vehicle Journal*, 6(3):572–580, Nov 2013.

[25] Jian Cao, Nigel Schofield, and Ali Emadi. Battery balancing methods: A comprehensive review. In *2008 IEEE Veh. Power Propuls. Conf.*, pages 1–6. IEEE, Sep 2008.

[26] Mohammad Charkhgard and Mohammad Farrokhi. State-of-charge estimation for lithium-ion batteries using neural networks and EKF. *IEEE Transactions on Industrial Electronics*, 57(12):4178–4187, Dec 2010.

[27] M. Chen and G. A. Rincon-Mora. Accurate Electrical Battery Model Capable of Predicting Runtime and I-V Performance. *IEEE Trans. Energy Convers.*, 21(2):504–511, Jun 2006.

[28] Chao-Yang Wang Christopher D. Rahn. *Battery Systems Engineering*. John Wiley & Sons Inc, 2013.

[29] Fabio Codeca, Sergio M Savaresi, and Giorgio Rizzoni. On battery State of Charge estimation: A new mixed algorithm. In *2008 IEEE Int. Conf. Control Appl.*, pages 102–107. IEEE, Sep 2008.

[30] Alexandre Collet, Jean-Christophe Crebier, and Alexandre Chureau. Multi-cell battery emulator for advanced battery management system benchmarking. In *2011 IEEE Int. Symp. Ind. Electron.*, pages 1093–1099. IEEE, Jun 2011.

[31] Haifeng Dai, Xiaolong Zhang, Xuezhe Wei, Zechang Sun, Jiayuan Wang, and Feng Hu. Cell-BMS validation with a hardware-in-the-loop simulation of lithium-ion battery cells for electric vehicles. *Int. J. Electr. Power Energy Syst.*, 52:174–184, Nov 2013.

[32] Mohamed Daowd, Noshin Omar, Peter van den Bossche, and Joeri van Mierlo. A review of passive and active battery balancing based on MATLAB/Simulink. *International Review of Electrical Engineering*, 6(7):2974–2989, Sep 2011.

[33] Aníbal T. de Almeida, Carlos Inverno, and Luís Santos. Integration of renewable energies for trolleybus and mini-bus lines in Coimbra. *World Electric Vehicle Journal*, 3(1), Jan 2009.

[34] R. Di Rienzo, F. Baronti, F. Vellucci, F. Cignini, F. Ortenzi, G. Pede, R. Roncella, and R. Saletti. Experimental analysis of an electric minibus with small battery and fast charge policy. In *2016 International Conference on Electrical Systems for Aircraft, Railway, Ship Propulsion and Road Vehicles and International Transportation Electrification Conference, ESARS-ITEC 2016*, pages 1–6. IEEE, Nov 2017.

[35] K. C. Divya and Jacob Østergaard. Battery energy storage technology for power systems-An overview. *Electric Power Systems Research*, 79(4):511–520, Apr 2009.

[36] F. Cignini F. Vellucci, G. Pede, F. Baronti, R. Di Rienzo. Effects of fast charge on a lithium-ion battery system. In *EVS29 Symposium*, pages 1–14, Jun 2016.

[37] Guodong Fan, Ke Pan, and Marcello Canova. A comparison of model order reduction techniques for electrochemical characterization of Lithium-ion batteries. In *2015 54th IEEE Conference on Decision and Control (CDC)*, volume 2016-Febru, pages 3922–3931. IEEE, Dec 2015.

[38] L. Garnier, D. Chatroux, S. Carcouet, and J. Dauchy. Comparison Between Standard and Innovative Solutions to exchange Energy between High Energy Storage Systems. In *PCIM Europe 2016; International Exhibition and Conference for Power Electronics, Intelligent Motion, Renewable Energy and Energy Management*, pages 1–8, May 2016.

[39] Mehdi Gholizadeh, Alireza Yazdizadeh, Mohsen Rahmati, and Abbas Aliabadi. SOC estimation for a lithium-ion battery by designing a nonlinear observer based on an equivalent circuit model. In *2017 IEEE 15th International Conference on Industrial Informatics (INDIN)*, pages 628–632. IEEE, Jul 2017.

[40] Radu Gogoana, Matthew B. Pinson, Martin Z. Bazant, and Sanjay E. Sarma. Internal resistance matching for parallel-connected lithium-ion cells and impacts on battery pack cycle life. *Journal of Power Sources*, 252:8–13, Apr 2014.

[41] Martin J. Klein Gregory L. Plett. Simulating Battery Packs Comprising Parallel Cell Modules and Series Cell Modules. In *EVS24*, pages 1–17, Jan 2009.

[42] Xuebing Han, Minggao Ouyang, Languang Lu, Jianqiu Li, Yuejiu Zheng, and Zhe Li. A comparative study of commercial lithium ion battery cycle life in electrical vehicle: Aging mechanism identification. *Journal of Power Sources*, 251:38–54, Apr 2014.

[43] M.A. Hannan, M.S.H. Lipu, A. Hussain, and A. Mohamed. A review of lithium-ion battery state of charge estimation and management system in electric vehicle applications: Challenges and recommendations. *Renewable and Sustainable Energy Reviews*, 78:834–854, Oct 2017.

[44] Hongwen He, Rui Xiong, and Jinxin Fan. Evaluation of lithium-ion battery equivalent circuit models for state of charge estimation by an experimental approach. *Energies*, 4(4):582–598, Mar 2011.

[45] T. Huria, M. Ceraolo, J. Gazzarri, and R. Jackey. High fidelity electrical model with thermal dependence for characterization and simulation of high power lithium battery cells. In *2012 IEEE Int. Electr. Veh. Conf.*, pages 1–8. IEEE, Mar 2012.

[46] Ala Al Haj Hussein and Issa Batarseh. An overview of generic battery models. In *IEEE Power and Energy Society General Meeting*, pages 1–6. IEEE, Jul 2011.

[47] Yong-Min Jeong, Yong-Ki Cho, Jung-Hoon Ahn, Seung-Hee Ryu, and Byoung-Kuk Lee. Enhanced Coulomb counting method with adaptive SOC reset time for estimating OCV. In *2014 IEEE Energy Convers. Congr. Expo.*, pages 1313–1318. IEEE, Sep 2014.

[48] Theodoros Kalogiannis, Erik Schaltz, and Andreas Elkjær Christensen. Functional Assessment of Battery Management System Tested on Hardware-in-the-Loop Simulator. *2017 International Conference on Electrical and Information Technologies (ICEIT)*, pages 1–6, Nov 2017.

[49] Bwo Ren Ke, Chen Yuan Chung, and Yen Chang Chen. Minimizing the costs of constructing an all plug-in electric bus transportation system: A case study in Penghu. *Applied Energy*, 177:649–660, Sep 2016.

[50] Taesic Kim, Wei Qiao, and Liyan Qu. Series-connected self-reconfigurable multicell battery. In *Proc. Twenty-Sixth Annu. IEEE Appl. Power Electron. Conf. Expo.*, pages 1382–1387, Mar 2011.

[51] Taesic Kim, Wei Qiao, and Liyan Qu. Real-time state of charge and electrical impedance estimation for lithium-ion batteries based on a hybrid battery model. In *Conference Proceedings - IEEE Applied Power Electronics Conference and Exposition - APEC*, pages 563–568. IEEE, Mar 2013.

[52] Oliver Konig, Christoph Hametner, Gunter Prochart, and Stefan Jakubek. Battery Emulation for Power-HIL Using Local Model Networks and Robust Impedance Control. *IEEE Trans. Ind. Electron.*, 61(2):943–955, Feb 2014.

[53] Alexander Kunith, Roman Mendelevitch, and Dietmar Goehlich. Electrification of a city bus network—An optimization model for cost-effective placing of charging infrastructure and battery sizing of fast-charging electric bus systems. *International Journal of Sustainable Transportation*, 11(10):707–720, Nov 2017.

[54] Xin Lai, Yuejiu Zheng, and Tao Sun. A comparative study of different equivalent circuit models for estimating state-of-charge of lithium-ion batteries. *Electrochimica Acta*, 259:566–577, Jan 2018.

[55] Antti Lajunen. Lifecycle costs and charging requirements of electric buses with different charging methods. *Journal of Cleaner Production*, 172:56–67, Jan 2018.

[56] Jianchao Li, Shunli Wang, Carlos Fernandez, Ni Wang, and Hongqiu Xie. The Battery Management System Construction Method Study for the Power Lithium-ion Battery Pack. *2017 2nd International Conference on Robotics and Automation Engineering (ICRAE)*, pages 285–289, Dec 2017.

[57] Xue Li, Jiuchun Jiang, Le Yi Wang, Dafen Chen, Yanru Zhang, and Caiping Zhang. A capacity model based on charging process for state of health estimation of lithium ion batteries. *Applied Energy*, 177:537–543, Sep 2016.

[58] Xueyan Li and Song-yul Choe. State-of-charge (SOC) estimation based on a reduced order electrochemical thermal model and extended Kalman filter. *2013 American Control Conference*, pages 1100–1105, Jun 2013.

[59] Languang Lu, Xuebing Han, Jianqiu Li, Jianfeng Hua, and Minggao Ouyang. A review on the key issues for lithium-ion battery management in electric vehicles. *Journal of Power Sources*, 226:272–288, Mar 2013.

[60] Hossein Maleki and Jason N. Howard. Internal short circuit in Li-ion cells. *Journal of Power Sources*, 191(2):568–574, Jun 2009.

[61] Jinhao Meng, Mattia Ricco, Guangzhao Luo, Maciej Swierczynski, Daniel Ioan Stroe, Ana Irina Stroe, and Remus Teodorescu. An overview of online implementable soc estimation methods for lithium-ion batteries. In *Proceedings - 2017 International Conference on Optimization of Electrical and Electronic Equipment, OPTIM 2017 and 2017 Intl Aegean Conference on Electrical Machines and Power Electronics, ACEMP 2017*, pages 573–580. IEEE, May 2017.

[62] Rocco Morello, F. Baronti, X. Tian, T. Chau, R. Di Rienzo, R. Roncella, B. Jeppesen, W. H. Lin, T. Ikushima, and R. Saletti. Hardware-in-the-loop simulation of FPGA-based state estimators for electric vehicle batteries. In *IEEE International Symposium on Industrial Electronics*, volume 2016-Novem, pages 280–285. IEEE, Jun 2016.

[63] Rocco Morello, Roberto Di Rienzo, Federico Baronti, Roberto Roncella, and Roberto Saletti. System on chip battery state estimator: E-bike case study. In *IECON Proceedings (Industrial Electronics Conference)*, pages 2129–2134. IEEE, Oct 2016.

[64] Rocco Morello, W. Zamboni, F. Baronti, R. Di Rienzo, R. Roncella, G. Spagnuolo, and R. Saletti. Comparison of state and parameter estimators for electric vehicle batteries. In *IECON 2015 - 41st Annual Conference of the IEEE Industrial Electronics Society*, pages 5433–5438. IEEE, Nov 2015.

[65] S. Nejad, D. T. Gladwin, and D. A. Stone. A systematic review of lumped-parameter equivalent circuit models for real-time estimation of lithium-ion battery states. *Journal of Power Sources*, 316:183–196, Jun 2016.

[66] Hao Nguyen-Van, Thang Nguyen, Vu Quan, Minh Nguyen, and Loan Pham-Nguyen. A topology of charging mode control circuit suitable for long-life Li-Ion battery charger. In *2016 IEEE 6th International Conference on Communications and Electronics, IEEE ICCE 2016*, pages 167–171. IEEE, Jul 2016.

[67] Sascha Nowak and Martin Winter. Elemental Analysis of Lithium Ion Batteries. *J. Anal. At. Spectrom.*, 32(10):1833–1847, Oct 2017.

[68] Khairi Bin Omar, Norhayati Soin, Wan Nor Liza Mahadi, and Hassan Malik. A new charger system approach: The current and voltage control loops. In *IEEE International Conference on Semiconductor Electronics, Proceedings, ICSE*, pages 165–170. IEEE, Jun 2010.

[69] S. Panchal, M. Mathew, R. Fraser, and M. Fowler. Electrochemical thermal modeling and experimental measurements of 18650 cylindrical lithium-ion battery during discharge cycle for an EV. *Applied Thermal Engineering*, 135:123–132, Feb 2018.

[70] Maral Partovibakhsh and Guangjun Liu. An Adaptive Unscented Kalman Filtering Approach for Online Estimation of Model Parameters and State-of-Charge of Lithium-Ion Batteries for Autonomous Mobile Robots. *IEEE Transactions on Control Systems Technology*, 23(1):357–363, Jan 2015.

[71] B. Pattipati, B. Balasingam, G. V. Avvari, K. R. Pattipati, and Y. Bar-Shalom. Open circuit voltage characterization of lithium-ion batteries. *Journal of Power Sources*, 269:317–333, Dec 2014.

[72] Sabine Piller, Marion Perrin, and Andreas Jossen. Methods for state-of-charge determination and their applications. In *Journal of Power Sources*, volume 96, pages 113–120. Elsevier, Jun 2001.

[73] G. (Gianfranco) Pistoia. *Lithium-ion batteries : advances and applications*. Elsevier, 2014.

[74] Gregory L. Plett. Extended Kalman filtering for battery management systems of LiPB-based HEV battery packs: Part 3. State and parameter estimation. *J. Power Sources*, 134(2):277–292, Aug 2004.

[75] Gregory L. Plett. Extended Kalman filtering for battery management systems of LiPB-based HEV battery packs Part 2. Modeling and identification. *Journal of Power Sources*, 161(2):1356–1368, Aug 2006.

[76] Andreas Poullikkas. A comparative overview of large-scale battery systems for electricity storage. *Renewable and Sustainable Energy Reviews*, 27:778–788, Nov 2013.

[77] Jian Qi and Dylan Dah-Chuan Lu. Review of battery cell balancing techniques. In *2014 Australasian Universities Power Engineering Conference, AUPEC 2014 - Proceedings*, pages 1–6. IEEE, Sep 2014.

[78] Nan Qin, Azwirman Gusrialdi, R. Paul Brooker, and Ali T-Raissi. Numerical analysis of electric bus fast charging strategies for demand charge reduction. *Transportation Research Part A: Policy and Practice*, 94:386–396, Dec 2016.

[79] Rocco Restaino and Walter Zamboni. Comparing particle filter and extended kalman filter for battery State-Of-Charge estimation. In *IECON 2012 - 38th Annu. Conf. IEEE Ind. Electron. Soc.*, pages 4018–4023. IEEE, Dec 2012.

[80] Rocco Restaino and Walter Zamboni. Rao-blackwellised particle filter for battery state-of-charge and parameters estimation. In *IECON 2013 - 39th Annu. Conf. IEEE Ind. Electron. Soc.*, pages 6783–6788. IEEE, Nov 2013.

[81] Matthias Rogge, Sebastian Wollny, and Dirk Uwe Sauer. Fast charging battery buses for the electrification of urban public transport-A feasibility study focusing on charging infrastructure and energy storage requirements. *Energies*, 8(5):4587–4606, May 2015.

[82] D.U. Sauer, Georg Bopp, Andreas Jossen, and Jürgen Garche. State of charge–what do we really speak about? In *INTELEC'99*, Jun 1999.

[83] Daniel Sauerteig, Nina Hanselmann, Arno Arzberger, Holger Reinshagen, Svetlozar Ivanov, and Andreas Bund. Electrochemical-mechanical coupled modeling and parameterization of swelling and ionic transport in lithium-ion batteries. *Journal of Power Sources*, 378:235–247, Feb 2018.

[84] Shuaijun Wu, Yijun Zou, Xin Peng, and Hongbiao Li. Hardware-in-loop verification of battery management system with RT-LAB. In *2014 IEEE Conf. Expo Transp. Electrif. Asia-Pacific (ITEC Asia-Pacific)*, pages 1–4. IEEE, Aug 2014.

[85] Philipp Sinhuber, Werner Rohlfs, and Dirk Uwe Sauer. Study on power and energy demand for sizing the energy storage systems for electrified local public transport buses. In *2012 IEEE Veh. Power Propuls. Conf.*, number January 2012, pages 315–320. IEEE, Feb 2012.

[86] Thomas A. Stuart and Wei Zhu. Modularized battery management for large lithium ion cells. *Journal of Power Sources*, 196(1):458–464, Jan 2011.

[87] Saravanan Meenatchi Sundaram, Mukund Kulkarni, and Vinten Diwakar. Management of large format liion batteries. In *2015 IEEE International Transportation Electrification Conference (ITEC)*, pages 1–7. IEEE, Aug 2015.

[88] Carlo Taborelli and Simona Onori. State of charge estimation using extended Kalman filters for battery management system. In *2014 IEEE International Electric Vehicle Conference (IEVC)*, pages 1–8. IEEE, Dec 2014.

[89] J. M. Tarascon and M. Armand. Issues and challenges facing rechargeable lithium batteries. *Nature*, 414(6861):359–367, Nov 2001.

[90] X. Tian, B. Jeppesen, T. Ikushima, F. Baronti, and R. Morello. Accelerating State-Of-Charge Estimation in FPGA-based Battery Management Systems. In *6th Hybrid and Electric Vehicles Conference (HEVC 2016)*, pages 4 (6 .)–4 (6 .). Institution of Engineering and Technology, Nov 2016.

[91] Francesco Vellucci, Giovanni Pede, Massimo Ceraolo, and Tarun Huria. Electrification of off-road vehicles: Examining the feasibility for the Italian market. In *World Electric Vehicle Journal*, volume 5, pages 101–117, May 2012.

[92] Qian Wang, Bin Jiang, Bo Li, and Yuying Yan. A critical review of thermal management models and solutions of lithium-ion batteries for the development of pure electric vehicles. *Renewable and Sustainable Energy Reviews*, 64:106–128, Oct 2016.

[93] Tiansi Wang, Chunbo Zhu, Lei Pei, Rengui Lu, and Bingliang Xu. The state of arts and development trend of SOH estimation for lithium-ion batteries. In *2013 9th IEEE Vehicle Power and Propulsion Conference, IEEE VPPC 2013*, pages 359–364. IEEE, Oct 2013.

[94] Xiaokun (Cara) Wang and Joaquín Avila González. Assessing Feasibility of Electric Buses in Small and Medium-Sized Communities. *International Journal of Sustainable Transportation*, 7(6):431–448, Nov 2013.

[95] Yusheng Wang, Yongxi Huang, Jiuping Xu, and Nicole Barclay. Optimal recharging scheduling for urban electric buses: A case study in Davis. *Transportation Research Part E: Logistics and Transportation Review*, 100:115–132, Apr 2017.

[96] Phil Weicker. *A Systems Approach to Lithium-Ion Battery Management*. Publishers, Artech House, 2013.

[97] Caihao Weng, Xuning Feng, Jing Sun, and Huei Peng. State-of-health monitoring of lithium-ion battery modules and packs via incremental capacity peak tracking. *Applied Energy*, 180:360–368, Oct 2016.

[98] Fangfang Yang, Dong Wang, Yang Zhao, Kwok Leung Tsui, and Suk Joo Bae. A study of the relationship between coulombic efficiency and capacity degradation of commercial lithium-ion batteries. *Energy*, 145:486–495, Feb 2018.

[99] Jufeng Yang, Bing Xia, Wenxin Huang, Yuhong Fu, and Chris Mi. Online state-of-health estimation for lithium-ion batteries using constant-voltage charging current analysis. *Applied Energy*, 212:1589–1600, Feb 2018.

[100] Ruixin Yang, Rui Xiong, Hongwen He, Hao Mu, and Chun Wang. A novel method on estimating the degradation and state of charge of lithium-ion batteries used for electrical vehicles. *Applied Energy*, 207:336–345, Dec 2017.

[101] Aixiang Zhang, Shizhan Song, Chuanyong Wang, Jian Zhang, Kun Wang, and Liwei Li. Research of battery management system for integrated power supply. In *2017 Chinese Automation Congress (CAC)*, pages 3178–3181. IEEE, Oct 2017.

[102] Xinrong Zhang, Huimin Gao, and Chunyan Zeng. Rotor position detection based on BEMF zero-crossing detection method with three-EMF force superposition. In *2016 13th International Conference on Ubiquitous Robots and Ambient Intelligence, URAI 2016*, pages 740–745. IEEE, Aug 2016.

[103] Yimin Zhou and Xiaoyun Li. Overview of lithium-ion battery SOC estimation. In *2015 IEEE International Conference on Information and Automation, ICIA 2015 - In conjunction with 2015 IEEE International Conference on Automation and Logistics*, pages 2454–2459. IEEE, Aug 2015.